

**Numerical Study of the Duct Shape Effect on the Performance of a Ducted Vertical Axis
Tidal Turbine**

by

Yasser Nabavi

BASc., Amirkabir University of Technology (Tehran Polytechnic), 2004

A thesis submitted in partial fulfillment of the requirements for the degree of
Master of Applied Science
in
The Faculty of Graduate Studies
(Mechanical Engineering)

THE UNIVERSITY OF BRITISH COLUMBIA

April 2008

© Yasser Nabavi, 2008

ABSTRACT

The current research focused on the numerical modeling of a three-bladed vertical-axis tidal current turbine using the commercial RANS code, FLUENT. A two-dimensional, incompressible, unsteady solver was used for the simulations in conjunction with a Spalart-Allmaras turbulence model. This approach proved to have satisfactory accuracy at a reasonable computational cost. The first phase of the research focused on simulating of a free-stream turbine for a range of current velocities and tip speed ratios. The torque and power generated by each blade was recorded as a function of azimuth angle and compared to experimentally measured torque and power. The experiments were conducted in parallel to the numerical work by the research group in the Naval Architecture Laboratory at the University of British Columbia.

In the second phase of the research, a simple venturi-shape duct was placed around the turbine to accelerate the flow and consequently increase the torque and power generated. Similar to the first phase of the research, the results were validated against experimental values to obtain sufficient confidence in the accuracy of the numerical model predictions.

The last phase of the project focused on the optimization of the duct shape with the goal of increasing the power generated by the turbine's blades over a cycle. The strategy chosen to improve the duct shape was to keep a constant contraction ratio for the duct and to redirect the flow to achieve a proper angle of attack for the airfoil, especially at the azimuth angles where the torque generated by the blades was low.

TABLE OF CONTENTS

ABSTRACT.....	ii
TABLE OF CONTENTS.....	iii
LIST OF TABLES.....	v
LIST OF FIGURES.....	vi
LIST OF SYMBOLS, NOMENCLATURES, AND ABBREVIATIONS	xiv
ACKNOWLEDGEMENT	xviii
1. Introduction	1
1.1 Energy Crisis in the 21 st Century	1
1.2 Renewable Energies.....	3
1.3 History and Forms of Tidal Energy	6
1.4 Modeling Approaches	9
1.4.1 Potential Flow Modeling	10
1.4.2 RANS Modeling	18
1.4.3 Experimental Approach	19
2. CFD Simulation of a Free-Stream Vertical Axis Tidal Turbine	21
2.1 Geometry definition.....	22
2.2 Grid Generation and Boundary Conditions.....	24
2.3 Domain Size Study.....	29
2.3.1 Domain Width Effect.....	31
2.3.2 Upstream Distance.....	32
2.3.3 Downstream Distance.....	33
2.4 Solver Specifications	33
2.5 Turbulence Modeling.....	37
3. CFD Simulation of a Ducted Vertical Axis Tidal Turbine.....	43
3.1 Grid Generation, Boundary Conditions and the Domain Size	44
3.2 Solver Specifications	46
3.3 Turbulence Modeling.....	47
4. Experimental Design and Analysis of BERT Turbine	48

4.1 Experimental Model.....	48
4.2 Testing Procedure and Methodology	51
5. Numerical Results and Post Processing Procedure.....	53
5.1 Free-stream Turbine Results and Analyses.....	56
5.2 Ducted Turbine Results and Analyses.....	68
6. Discussion.....	76
6.1 Arms Effect.....	77
6.2 Validation of Numerical Results.....	79
6.3 Sources of Discrepancy	85
7. Duct Shape Optimization	91
7.1 Preliminary Approach	91
7.2 Steady-State Study of Different Ducts	99
7.2.1 Methodology.....	99
7.2.2 Grid and Solver Specifications.....	102
7.2.3 Examined Duct Configurations.....	102
7.3 Unsteady Simulations of Various Duct Configurations	125
8. Conclusion, Recommendations, and Future Work	131
8.1 Conclusion.....	131
8.2 Recommendations	132
8.3 Future Work.....	134
References	135

LIST OF TABLES

Table 1-1: Reports on experiments conducted by Barry Davis from Nova Energy in 1980's	20
Table 2-1: Simulation Plan for a free-stream three-bladed turbine	21
Table 2-2: Geometric specifications of the turbine's model.....	22
Table 2-3: Grid densities used for grid refinement study	28
Table 2-4: Results of the grid refinement study	29
Table 2-5: Domain size study results	31
Table 2-6: Under Relaxation Factors used for the simulations.....	34
Table 3-1: Grid Refinement Study for a Ducted Turbine	45
Table 5-1: Reynolds number changes as TSR and inlet velocity change.....	64
Table 7-1: Duct with guiding vane configuration results	104
Table 7-2: UBC duct modifications results.....	105
Table 7-3: Bump configurations results	109
Table 7-4: Double-Duct configuration results.....	117
Table 7-5: Guiding vane concept results.....	120
Table 8-1: Summary of the simulation results for different duct shapes	133

LIST OF FIGURES

Figure 1-1: Global Carbon emission increase [1]	1
Figure 1-2: Increasing demand for energy by region [2]	2
Figure 1-3: Comparison of US renewable energy consumption and other sources of energy [5]	4
Figure 1-4: Predicted electricity price by solar energy [6]	5
Figure 1-5: NASDAQ stock price trend for SunPower Corporation [7]	5
Figure 1-6: Wave energy devices (Courtesy of Pelamis Wave Power Ltd.)	6
Figure 1-7: Rance 240 MW tidal power plant in France [9]	6
Figure 1-8: Horizontal axis tidal turbine (Courtesy of Marine Current Turbine Ltd.)	7
Figure 1-9: Vertical axis tidal turbine (Courtesy of Blue Energy Canada)	7
Figure 1-10: Tidal sites of Canada [12]	9
Figure 1-11: Aerodynamic model of a free-stream vertical axis turbine	10
Figure 1-12: Single stream tube model [14]	12
Figure 1-13: Multiple stream tube model [14]	12
Figure 1-14: Double multiple stream tube model [14]	12
Figure 1-15: Blades are replaced with vortex filaments in vortex methods [14]	16
Figure 1-16: Cascade Model approach [10]	17
Figure 1-17: Upstream and downstream velocities in Cascade Model [10]	17
Figure 2-1: Tow tank model	22
Figure 2-2: Geometry of the physical domain including inlet, outlet, tow tank walls, blades, shaft, and interfaces	23
Figure 2-3: Geometry of the blades, shaft, and interfaces	23
Figure 2-4: NACA 63 ₄ -021 profile and coordinates	23
Figure 2-5: Structured fine grid used around the blades	25
Figure 2-6: Turbulent boundary layer profile [37]	26
Figure 2-7: Structured fine grid around the shaft	27
Figure 2-8: Unstructured grid of the domain	28
Figure 2-9: Unstructured grid around the blades and the shaft	28
Figure 2-10: Grid convergence results for a free-stream turbine at TSR=2.75	29
Figure 2-11: Definition of 2D blockage ratio	30
Figure 2-12: Definition of 3D blockage ratio	30

Figure 2-13: Domain width effect on the torque generated by the turbine	32
Figure 2-14: The upstream distance effect on the torque generated by the turbine	33
Figure 2-15: Sliding mesh scheme used for modeling the moving mesh	36
Figure 2-16: Sliding mesh scheme concept.....	37
Figure 2-17: Approaches to turbulent modeling [37]	38
Figure 2-18: Comparison of the results obtained for different turbulence models	41
Figure 2-19: Comparison of two available approaches to the near wall modeling [37]	42
Figure 3-1: UBC duct dimensions (all dimensions are in metric)	43
Figure 3-2: Interfaces in the ducted turbine configuration	44
Figure 3-3: Duct and blade grid in ducted turbine configuration	44
Figure 3-4: Grid convergence results for a ducted turbine at TSR=2.75.....	46
Figure 4-1: Experimental model of the turbine tested at UBC tow tank.....	48
Figure 4-2: Force balance assembly and data acquisition devices	49
Figure 4-3: Testing carriage setup.....	50
Figure 4-4: Experimental model of a ducted turbine.....	50
Figure 4-5: Torque curve versus the azimuth angle for a typical run	52
Figure 4-6: Averaging technique	52
Figure 4-7: Averaged torque curve over a 360 degrees cycle	52
Figure 5-1: Wake development as the turbine rotates	54
Figure 5-2: Repeating torque curves at steady conditions	54
Figure 5-3: Torque curve (3 blades) ; V=1.0 m/s , TSR=2.00.....	56
Figure 5-4: Torque curve (single blade) ; V=1.0 m/s , TSR=2.00	56
Figure 5-5: Torque curve (3 blades) ; V=1.0 m/s , TSR=2.25.....	56
Figure 5-6: Torque curve (single blade) ; V=1.0 m/s , TSR=2.25	56
Figure 5-7: Torque curve (3 blades) ; V=1.0 m/s , TSR=2.50.....	57
Figure 5-8: Torque curve (single blade) ; V=1.0 m/s , TSR=2.50	57
Figure 5-9: Torque curve (3 blades) ; V=1.0 m/s , TSR=2.75.....	57
Figure 5-10: Torque curve (single blade) ; V=1.0 m/s , TSR=2.75	57
Figure 5-11: Torque curve (3 blades) ; V=1.0 m/s , TSR=3.00.....	57
Figure 5-12: Torque curve (single blade) ; V=1.0 m/s , TSR=3.00.....	57
Figure 5-13: Velocity contours at V=1 m/s and TSR=2.00.....	59
Figure 5-14: Velocity contours at V=1 m/s and TSR=3.00.....	59

Figure 5-15: Efficiency curve for a free-stream turbine at $V=1.0$ m/s	60
Figure 5-16: Torque curve (3 blades) ; $V=1.5$ m/s , $TSR=2.00$	61
Figure 5-17: Torque curve (single blade) ; $V=1.5$ m/s , $TSR=2.00$	61
Figure 5-18: Torque curve (3 blades) ; $V=1.5$ m/s , $TSR=2.25$	61
Figure 5-19: Torque curve (single blade) ; $V=1.5$ m/s , $TSR=2.25$	61
Figure 5-20: Torque curve (3 blades) ; $V=1.5$ m/s , $TSR=2.50$	61
Figure 5-21: Torque curve (single blade) ; $V=1.5$ m/s , $TSR=2.50$	61
Figure 5-22: Torque curve (3 blades) ; $V=1.5$ m/s , $TSR=2.75$	62
Figure 5-23: Torque curve (single blade) ; $V=1.5$ m/s , $TSR=2.75$	62
Figure 5-24: Torque curve (3 blades) ; $V=1.5$ m/s , $TSR=3.00$	62
Figure 5-25: Torque curve (single blade) ; $V=1.5$ m/s , $TSR=3.00$	62
Figure 5-26: Efficiency curve for a free-stream turbine at $V=1.5$ m/s	64
Figure 5-27: Torque curve (3 blades) ; $V=2.0$ m/s , $TSR=2.00$	65
Figure 5-28: Torque curve (single blade) ; $V=2.0$ m/s , $TSR=2.00$	65
Figure 5-29: Torque curve (3 blades) ; $V=2.0$ m/s , $TSR=2.25$	65
Figure 5-30: Torque curve (single blade) ; $V=2.0$ m/s , $TSR=2.25$	65
Figure 5-31: Torque curve (3 blades) ; $V=2.0$ m/s , $TSR=2.50$	66
Figure 5-32: Torque curve (single blade) ; $V=2.0$ m/s , $TSR=2.50$	66
Figure 5-33: Torque curve (3 blades) ; $V=2.0$ m/s , $TSR=2.75$	66
Figure 5-34: Torque curve (single blade) ; $V=2.0$ m/s , $TSR=2.75$	66
Figure 5-35: Torque curve (3 blades) ; $V=2.0$ m/s , $TSR=3.00$	66
Figure 5-36: Torque curve (single blade) ; $V=2.0$ m/s , $TSR=3.00$	66
Figure 5-37: Efficiency curve for inlet velocity of 2.0 m/s	67
Figure 5-38: Comparison of efficiency for free-stream turbine at different current velocities	67
Figure 5-39: Torque curve (3 blades); $V=1.5$ m/s, $TSR=2.00$	68
Figure 5-40: Torque curve (single blade) ; $V=1.5$ m/s , $TSR=2.00$	68
Figure 5-41: Torque curve (3 blades) ; $V=1.5$ m/s , $TSR=2.25$	68
Figure 5-42: Torque curve (single blade) ; $V=1.5$ m/s , $TSR=2.25$	68
Figure 5-43: Torque curve (3 blades) ; $V=1.5$ m/s , $TSR=2.50$	69
Figure 5-44: Torque curve (single blade) ; $V=1.5$ m/s , $TSR=2.50$	69
Figure 5-45: Torque curve (3 blades) ; $V=1.5$ m/s , $TSR=2.75$	69
Figure 5-46: Torque curve (single blade) ; $V=1.5$ m/s , $TSR=2.75$	69

Figure 5-47: Torque curve (3 blades) ; V=1.5 m/s , TSR=3.00.....	69
Figure 5-48: Torque curve (single blade) ; V=1.5 m/s , TSR=3.00.....	69
Figure 5-49: Efficiency curve for a ducted turbine at V=1.5 m/s.....	70
Figure 5-50: Velocity contours at TSR=2.00.....	71
Figure 5-51: Velocity contours at TSR=3.00.....	72
Figure 5-52: Blade's angle of attack calculation for a free-stream turbine.....	72
Figure 5-53: Blade's angle of attack calculation for a ducted turbine.....	72
Figure 5-54: Torque curve (3 blades) ; V=2.0 m/s , TSR=2.00.....	73
Figure 5-55: Torque curve (single blade) ; V=2.0 m/s , TSR=2.00.....	73
Figure 5-56: Torque curve (3 blades) ; V=2.0 m/s , TSR=2.25.....	74
Figure 5-57: Torque curve (single blade) ; V=2.0 m/s , TSR=2.25.....	74
Figure 5-58: Torque curve (3 blades) ; V=2.0 m/s , TSR=2.50.....	74
Figure 5-59: Torque curve (single blade) ; V=2.0 m/s , TSR=2.50.....	74
Figure 5-60: Torque curve (3 blades) ; V=2.0 m/s , TSR=2.75.....	74
Figure 5-61: Torque curve (single blade) ; V=2.0 m/s , TSR=2.75.....	74
Figure 5-62: Torque curve (3 blades) ; V=2.0 m/s , TSR=3.00.....	75
Figure 5-63: Torque curve (single blade) ; V=2.0 m/s , TSR=3.00.....	75
Figure 5-64: Efficiency curve for a ducted turbine at V=2.0 m/s.....	75
Figure 6-1: Arms-Shaft connections.....	76
Figure 6-2: Arm-Blade connection.....	76
Figure 6-3: Arms' parasitic drag experimental model.....	78
Figure 6-4: Comparison of the efficiency curve with and without the arms effect (V=1.5 m/s).....	79
Figure 6-5: Comparison of numerical and experimental efficiencies for a free stream turbine at V=1.5 m/s.....	80
Figure 6-6: Comparison of numerical and experimental efficiencies for a free stream turbine at V=2.0 m/s.....	80
Figure 6-7: 3-Arm configuration.....	81
Figure 6-8: Arm-blade connection at the blade's tip.....	81
Figure 6-9: Comparison of numerical and experimental efficiencies for a ducted turbine at V=1.5 m/s ..	82
Figure 6-10: Comparison of numerical and experimental efficiencies for a ducted turbine at V=2.0 m/s	83
Figure 6-11: Comparison of experimental and numerical free-stream turbine torque at V=1.5 TSR=2.0084	
Figure 6-12: Comparison of experimental and numerical free-stream turbine torque at V=2.0 TSR=2.7584	

Figure 6-13: Comparison of experimental and numerical ducted turbine torque at $V=1.5$ $TSR=2.75$	84
Figure 6-14: Comparison of experimental and numerical ducted turbine torque at $V=2.0$ $TSR=2.00$	84
Figure 6-15: Comparison of 3-blade torque obtained from FLUENT, DVM, and Experiments ($V=1.5$, $TSR=2.50$)	85
Figure 6-16: Comparison of single-blade torque obtained from FLUENT, DVM, and Experiments ($V=1.5$, $TSR=2.50$)	85
Figure 6-17: RPM fluctuations in experiments	88
Figure 6-18: Free surface disturbance at lower velocities.....	89
Figure 6-19: Free surface disturbance at higher velocities.....	89
Figure 6-20: Experimental torque variations.....	89
Figure 6-21: Comparison of free-stream results from FLUENT and experiments including the error bars	90
Figure 7-1: Single-blade torque curve over a cycle in the presence of the other two blades.....	91
Figure 7-2: UBC duct with a hollow in the middle (mod 1).....	93
Figure 7-3: A duct with straight line connecting edges (mod 2).....	94
Figure 7-4: A duct with concave connecting edges (mod 3).....	94
Figure 7-5: Efficiency comparison of different modifications of UBC duct	95
Figure 7-6: 3-Blade torque comparison of three UBC duct modifications ($V=1.5$ m/s ; $TSR=2.00$).....	96
Figure 7-7: Single-Blade torque comparison of three UBC duct modifications ($V=1.5$ m/s ; $TSR=2.00$)	96
Figure 7-8: 3-Blade torque comparison of three UBC duct modifications ($V=1.5$ m/s ; $TSR=2.25$).....	97
Figure 7-9: Single-Blade torque comparison of three UBC duct modifications ($V=1.5$ m/s ; $TSR=2.25$)	97
Figure 7-10: 3-Blade torque comparison of three UBC duct modifications ($V=1.5$ m/s ; $TSR=2.50$).....	97
Figure 7-11: Single-Blade torque comparison of three UBC duct modifications ($V=1.5$ m/s ; $TSR=2.50$) ..	97
Figure 7-12: 3-Blade torque comparison of three UBC duct modifications ($V=1.5$ m/s ; $TSR=2.75$).....	97
Figure 7-13: Single-Blade torque comparison of three UBC duct modifications ($V=1.5$ m/s ; $TSR=2.75$) ..	97
Figure 7-14: 3-Blade torque comparison of three UBC duct modifications ($V=1.5$ m/s ; $TSR=3.00$).....	98
Figure 7-15: Single-Blade torque comparison of three UBC duct modifications ($V=1.5$ m/s ; $TSR=3.00$) ..	98
Figure 7-16: Typical single-blade torque comparison for UBC duct and its modifications ($V=1.5$ m/s ; $TSR=2.50$)	99
Figure 7-17: Design box concept.....	100
Figure 7-18: Measured flow parameters for comparison of different ducts.....	101
Figure 7-19: Velocity contours for the UBC duct as the reference.....	103
Figure 7-20: YV1 (Guiding vanes at 15 degrees AOA).....	104

Figure 7-21: YV2 (Guiding vanes at 5 degrees AOA).....	104
Figure 7-22: YV3 (Guiding vanes at 5 degrees angle of attack and with a rounded trailing edge).....	104
Figure 7-23: Velocity angle distribution for guiding vane configurations.....	105
Figure 7-24: YV4 velocity contours	107
Figure 7-25: YV5 velocity contours	107
Figure 7-26: YV6 velocity contours	107
Figure 7-27: YV7 velocity contours	107
Figure 7-28: YV8 velocity contours	107
Figure 7-29: Velocity angle distribution for UBC duct modifications	108
Figure 7-30: Comparison of velocity magnitude distribution over the blades' path for UBC and YV10 ducts.....	110
Figure 7-31: Comparison of velocity angle distribution over the blades' path for UBC and YV10 ducts ..	110
Figure 7-32: Comparison of velocity magnitude distribution over the blades' path for YV10 and YV11 ducts.....	110
Figure 7-33: Comparison of velocity angle distribution over the blades' path for YV10 and YV11 ducts.	110
Figure 7-34: Comparison of velocity magnitude distribution over the blades' path for YV11 and YV12 ducts.....	111
Figure 7-35: Comparison of velocity angle distribution over the blades' path for YV11 and YV12 ducts	111
Figure 7-36: Comparison of velocity magnitude distribution over the blades' path for YV11 and YV13 ducts.....	112
Figure 7-37: Comparison of velocity angle distribution over the blades' path for YV11 and YV13 ducts	112
Figure 7-38: Velocity angles contours for the four-bump configuration (Duct YV13).....	112
Figure 7-39: Comparison of velocity magnitude distribution over the blades' path for YV14, YV15, and YV16 ducts.....	113
Figure 7-40: Comparison of velocity angle distribution over the blades' path for YV14, YV15, and YV16 ducts.....	113
Figure 7-41: Comparison of velocity magnitude distribution over the blades' path for YV17 and YV18 ducts.....	113
Figure 7-42: Comparison of velocity angle distribution over the blades' path for YV17 and YV18 ducts	113
Figure 7-43: Comparison of velocity magnitude distribution over the blades' path for YV19 and YV20 ducts.....	114
Figure 7-44: Comparison of velocity angle distribution over the blades' path for YV19 and YV20 ducts	114

Figure 7-45: YV9 velocity contours	115
Figure 7-46: YV10 velocity contours	115
Figure 7-47: YV11 velocity contours	115
Figure 7-48: YV12 velocity contours	115
Figure 7-49: YV13 velocity contours	115
Figure 7-50: YV14 velocity contours	115
Figure 7-51: YV15 velocity contours	115
Figure 7-52: YV16 velocity contours	115
Figure 7-53: YV17 velocity contours	116
Figure 7-54: YV18 velocity contours	116
Figure 7-55: YV19 velocity contours	116
Figure 7-56: YV20 velocity contours	116
Figure 7-57: Comparison of velocity magnitude distribution over the blades' path for YV21, YV22, YV23, and YV24 ducts.....	118
Figure 7-58: Comparison of velocity angle distribution over the blades' path for YV21, YV22, YV23, and YV24 ducts.....	118
Figure 7-59: Comparison of velocity magnitude distribution over the blades' path for YV25, YV26, YV27, and YV28 ducts.....	119
Figure 7-60: Comparison of velocity angle distribution over the blades' path for YV25, YV26, YV27, and YV28 ducts.....	119
Figure 7-61: YV21 velocity contours	119
Figure 7-62: YV22 velocity contours	119
Figure 7-63: YV23 velocity contours	119
Figure 7-64: YV24 velocity contours	119
Figure 7-65: YV25 velocity contours	120
Figure 7-66: YV26 velocity contours	120
Figure 7-67: YV27 velocity contours	120
Figure 7-68: YV28 velocity contours	120
Figure 7-69: Comparison of velocity magnitude distribution over the blades' path for YV29 and YV30 ducts.....	122
Figure 7-70: Comparison of velocity angle distribution over the blades' path for YV29 and YV30 ducts	122

Figure 7-71: Comparison of velocity magnitude distribution over the blades' path for YV31, YV32, YV33, YV34, and YV35 ducts	123
Figure 7-72: Comparison of velocity angle distribution over the blades' path for YV31, YV32, YV33, YV34, and YV35 ducts.....	123
Figure 7-73: YV29 velocity contours	123
Figure 7-74: YV30 velocity contours	123
Figure 7-75: YV31 velocity contours	124
Figure 7-76: YV31 velocity vectors.....	124
Figure 7-77: YV32 velocity contours	124
Figure 7-78: YV32 velocity vectors.....	124
Figure 7-79: YV33 velocity contours	124
Figure 7-80: YV33 velocity vectors.....	124
Figure 7-81: YV34 velocity contours	124
Figure 7-82: YV34 velocity vectors.....	124
Figure 7-83: YV35 velocity contours	125
Figure 7-84: YV35 velocity vectors.....	125
Figure 7-85: Efficiency comparison for different duct shapes.....	126
Figure 7-86: 3-Blade torque curve for YV3 at different TSR's.....	127
Figure 7-87: Single-blade torque curve for YV3 at different TSR's	127
Figure 7-88: 3-Blade torque curve for YV11 at different TSR's.....	127
Figure 7-89: Single-blade torque curve for YV11 at different TSR's	127
Figure 7-90: 3-Blade torque curve for YV13 at different TSR's.....	127
Figure 7-91: Single-blade torque curve for YV13 at different TSR's	127
Figure 7-92: 3-Blade torque curve for YV28 at different TSR's.....	128
Figure 7-93: Single-blade torque curve for YV28 at different TSR's	128
Figure 7-94: 3-Blade torque curve for YV34 at different TSR's.....	128
Figure 7-95: Single-blade torque curve for YV34 at different TSR's	128
Figure 7-96: Velocity contours of YV34 show the flow separation from the upper side the guide vanes at V=1.5 m/s and TSR=3.00	129
Figure 7-97: Velocity vectors of YV34 show the flow separation from the upper side of the guide vanes at V=1.5 m/s and TSR=3.00	129
Figure 7-98: Summary of the performance of studied ducts.....	130

LIST OF SYMBOLS, NOMENCLATURES, AND ABBREVIATIONS

2D	Two-dimensional
3D	Three-dimensional
A_{\min}	Minimum area of the duct (throat area)
A_{\max}	Maximum area of the duct
A_{tfa}	Projected frontal area of the turbine
A_{tsa}	Cross section area of the tow tank
BERT	Blue Energy Research Turbine
C	Blades chord
C_d	Blade drag coefficient
C_k	Turbine efficiency
$C_{k \text{ arms}}$	Efficiency reduction due to the parasitic drag of the connecting arms
C_l	Blade lift coefficient
C_n	Normal force coefficient
C_p	Power coefficient
C_t	Tangential force coefficient
C_{DD}	Rotor drag coefficient
CAD	Computer Aided Manufacturing (or Canadian Dollar)
CFD	Computational Fluid Dynamics
CPU	Central Processing Unit
CR	Contraction Ratio
D	Drag force per unit span
DNS	Direct Numerical Simulation
DVM	Discrete Vortex Method
\vec{F}	Force vector on the blade
F_D	Stream-wise drag force
F_t	Tangential force exerted on the blade
GBP	Great Britain Pound
i	Unit vector in X direction
IPO	Initial Public Offering

$T_{s,b}$	Torque generated by a single blade
TRF	Torque Ripple Factor
TSR	Tip Speed Ratio
u	Local velocity
u_τ	Friction velocity
U_u	Interference factor for the upstream half-cycle
U_d	Interference factor for the downstream half-cycle
U_i	Velocity vector
UBC	University of British Columbia
UDF	User Defined Function
UNFCCC	United Nations Framework Committee on Climate Change
USD	United-States Dollar
V	Inlet velocity (upstream velocity)
V_a	Induced velocity
V_{ad}	Induced velocity in downstream
V_{au}	Induced velocity in upstream
V_e	Wake velocity in upstream side of the turbine
V_n	Normal velocity component seen by the blade
V_R	Resultant velocity seen by the blade
V_t	Tangential velocity component seen by the blade
V_w	Wake velocity downstream of the turbine
V_∞	Current velocity
$V_{\infty i}$	Sectional upstream velocity
W	Duct width
x_i	Position vector
X	Horizontal axis in the stationary plane
y	Distance from wall
y^+	Non-dimensional wall distance
Y	Vertical axis in the stationary plane
α	Angle of attack seen by the blade
ε	Dissipation rate of turbulence kinetic energy

ε_b	Blockage ratio
θ	Azimuth angle (phase angle)
μ	Dynamic viscosity
μ_t	Turbulent eddy viscosity
ν	Kinematic Viscosity
ρ	Density of fluid (water)
σ	Solidity ratio
τ	Shear stress
ω	Angular velocity
Γ	Circulation around the blade's profile
Γ_{SV}	Circulation of shed vortices
Γ_B	Instantaneous circulation of blade's profile
Φ	A typical scalar quantity of the flow field
$\bar{\Phi}$	Ensemble average of a scalar quantity
Φ'	Fluctuations of a scalar quantity in a turbulent flow field

ε_b	Blockage ratio
θ	Azimuth angle (phase angle)
μ	Dynamic viscosity
μ_t	Turbulent eddy viscosity
ν	Kinematic Viscosity
ρ	Density of fluid (water)
σ	Solidity ratio
τ	Shear stress
ω	Angular velocity
Γ	Circulation around the blade's profile
Γ_{SV}	Circulation of shed vortices
Γ_B	Instantaneous circulation of blade's profile
Φ	A typical scalar quantity of the flow field
$\bar{\Phi}$	Ensemble average of a scalar quantity
Φ'	Fluctuations of a scalar quantity in a turbulent flow field

ACKNOWLEDGEMENT

First of all, I would like to thank my supervisor, Dr. Calisal for his continuous help and support during my Master`s program. It was Dr. Calisal`s trust and support that provided me with a wonderful opportunity to start my research at UBC with very friendly and high calibre people at Naval Architecture Lab. I am also grateful to Jon Mikkelsen, whose reliable support was available to all team members in every aspect of the project. I would also like to thank Dr. Farrokh Sassani, the former graduate advisor of Mechanical Engineering Department, for his kind guidance throughout my studies.

Also, I would like to thank my colleagues at the Naval Lab who helped me in every aspect of this project. I am so indebted to my good friend Voytek Klaptocz for his generous help in every aspect of the project from mesh generation to editing this thesis. My uncle, Soheil, made a great contribution to the revision of this document as well. I would also like to thank my close friend Mahmoud Alidadi for sharing his knowledge and concerns in the design and modeling parts of the project. I am also grateful to Bill Rawlings for his extraordinary help in providing us with unique, high quality experimental data. Without Bill`s input, this numerical modeling project would have been useless. I should also thank the co-op students in our lab, Cameron Fraser, John Axerio, Florent Cultot, Pierre Leplatois, Bo Zulonas, and Thomas Chabut. Cam especially provided a great deal of help in the set-up and monitoring process of the simulations.

I should also thank Blue Energy Canada, specially our good friend, Jon Ellison, for their financial support of the project and their generous help during the experiments.

A warm appreciation is deserved for my father-in-law who opened new horizons in my ambitions and made a significant impact on my vision. I am also extremely grateful to Nana, the best mother-in-law in the world, whose kindness helped me and my wife overcome any challenges. I would also like to thank my parents for being my there for me. I am grateful to my dad who showed me how to think and how to live; although, I have not been a good learner. I should thank my mom as well for her sincere love and support during every stage of my life. Moreover, I would like to express my warmest appreciations to my dear wife, whose presence in my life is the cause of my motivation and hope for the future.

At the end, I would like to thank all my professors at UBC and Tehran Polytechnic for their teachings and support during my Master`s and undergraduate studies.

1. Introduction

1.1 Energy Crisis in the 21st Century

With origins dating back to the industrial revolution that took place over a century ago, continued development and technological progress has had a tremendous impact on the all aspects of human life. One of the main factors that determine industrial and technological wealth of a country is its access to natural resources such as minerals and energy resources. Needless to say that energy has played a key role in the in international relations and economy in the recent century. Although industrialisation has caused thousands of improvements to our lives, its side effects are becoming the main challenge of 21st century. The challenges include a vast category of environmental, social, political, and economical problems. Global warming, greenhouse gasses, pollution, political and military conflicts to access energy resources such as oil and gas, and shortage of energy resources are a few examples of the challenges industrialisation has caused. According to many reports by governmental and non-governmental organizations, the catastrophic impact of excessive use of fossil fuels is among the imminent threats to humanity and needs urgent considerations by governments, businesses, and individuals. The Kyoto Protocol as an amendment to the United Nations Framework Convention on Climate Change (UNFCCC) was enforced to urge the governments to reduce the greenhouse gas emissions. As of December 2006, 169 countries signed the protocol. Figure 1-1 shows the global increase of Carbon emission in the past two centuries.

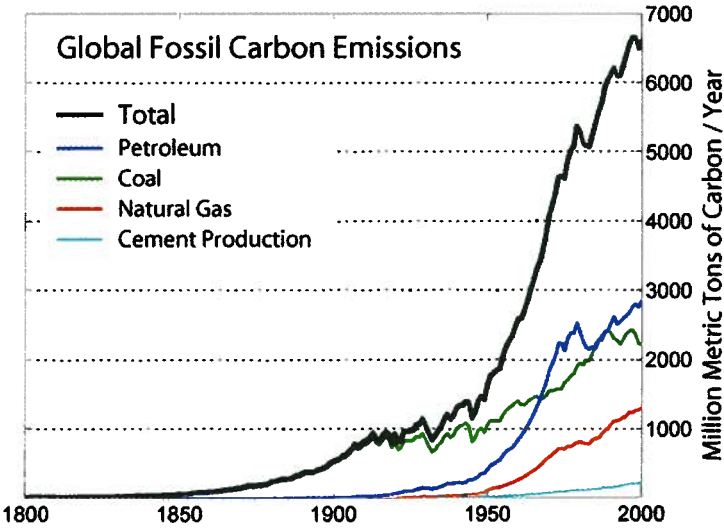


Figure 1-1: Global Carbon emission increase [1]

The increasing demand for energy, especially in developing countries and energy-hungry China and India worsen the situation. Figure 1-2 shows the global increasing demand for energy.

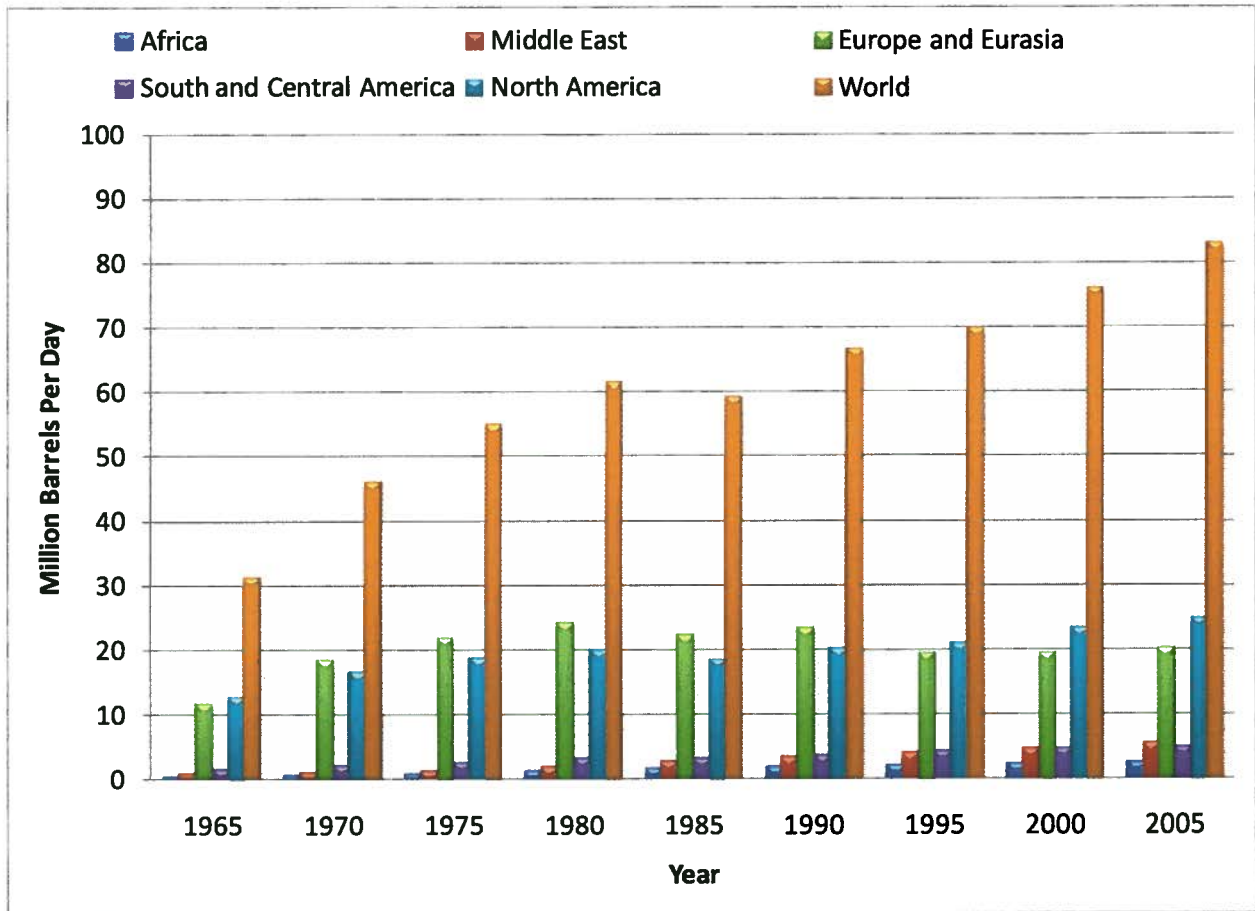


Figure 1-2: Increasing demand for energy by region [2]

The current oil price has reached a record high by topping 98 USD per barrel in November 2007 substantiating the world’s thirst for energy. The decreasing fossil fuel reserves, the reducing oil production rates predicted by Hubert’s Peak Law [3] as well as the increasing problems due to global climate change have motivated governments, corporations, and small size industrial sectors to encourage pursuing research and development in the field of alternative energies. Nuclear energy, currently under considerations by many nations as a “clean” alternative to fossil fuels has its own environmental and political problems. The focus of research and development in the recent years has been on new sustainable methods to produce energy often referred to as renewable energies.

1.2 Renewable Energies

There are many types of methods for extracting energy with minimal environmental impact that are known as Renewable Energies. Renewables have gained popularity in the recent decades and billions of dollars are being invested in research and development in these fields. The main known sources of renewable energy include:

- Geothermal Energy
- Bio-fuel and Biomass
- Hydropower
- Fuel Cells
- Solar Energy
- Wind Energy
- Ocean Energy
 - Wave Energy
 - Tidal Energy
 - Thermal Energy

Figure 1-3 shows the renewable energy consumption in the United-States in 2006. As shown, hydropower and biomass are widely used to generate electricity. On the other hand, solar, wind and geothermal energies are still in the preliminary stages of development and the power generated by them is not economically competitive with other forms of energy. The investment in these fields, however, is significantly increasing. According to United Nations Environment Programme, the global investment in clean energies has double from 2004 to 2006, to \$70.9 billion [4]. Also, the venture capital and private equity invested in sustainable energy increased by 69% in 2006, to \$8.6 billion [4].

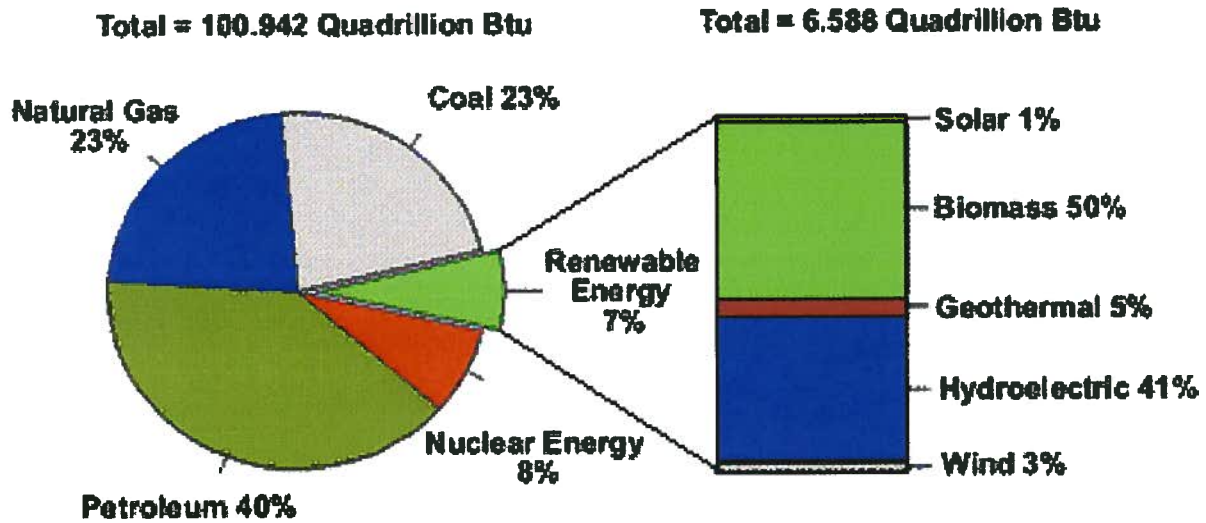


Figure 1-3: Comparison of US renewable energy consumption and other sources of energy [5]

Among the renewables, geothermal energy, biomass, and hydroelectricity are widely used and have reached technological maturity. Solar power is currently becoming a profitable sector of sustainable energy. The technology is well developed and is applicable especially in the regions with low latitudes (close to the equator). This type of energy is extracted using solar panels and the price of energy obtained from solar panels is about 28-30 cents per kW-hr. Figure 1-4 shows the predictions for solar power in the next decade. As shown in Figure 1-4, the price of solar power is predicted to exceed the cost of production by 2014. The market value of the global publicly traded solar companies stood at about \$1 billion in 2004, while currently, after a myriad of IPOs, they are worth about \$71 billion [6]. Figure 1-5 shows a sample of revolutionary changes in the market situation for solar power. This figure shows the share price of SunPower Corporation, a California based company in design and manufacturing of Photovoltaic solar panels. It is seen, the stock price has almost quadrupled from January 2007 to November 2007.

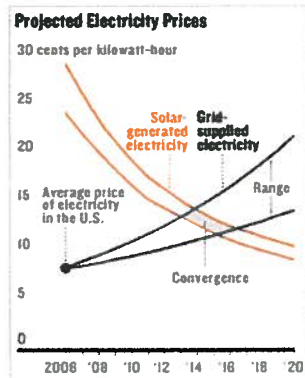


Figure 1-4: Predicted electricity price by solar energy [6]



Figure 1-5: NASDAQ stock price trend for SunPower Corporation [7]

Wind energy is another alternative which is still under development and a large number of companies are still trying to produce economically efficient devices in the form of wind farms or for individual buildings. Wind energy devices (wind turbines) work by harnessing the kinetic energy of the wind. One of the problems with this form of energy is that wind is usually not precisely predictable. Statistical data, however, allows designers and engineers to find suitable sites for construction of wind power plants. There are two major types of turbines developed to extract wind energy: horizontal axis tidal turbines and vertical axis tidal turbines. While the majority of wind turbines today are horizontal axis, an increasing number of technology developers are re-examining the vertical axis concept.

Ocean energy is also one of the most popular and reliable forms of renewable energies. This type of energy is divided into two main subsections: wave energy and tidal energy (Figure 1-6 and Figure 1-7). Wave energy is concentrated on absorbing the kinetic energy of the ocean waves while tidal energy is focused on capturing either potential or kinetic energy of tidal currents. It is estimated that marine energy could create a global business opportunity worth 600 billion GBP (more than \$1.2 trillion USD) [8].



Figure 1-6: Wave energy devices (Courtesy of Pelamis Wave Power Ltd.)



Figure 1-7: Rance 240 MW tidal power plant in France [9]

1.3 History and Forms of Tidal Energy

Tidal energy has the potential to be one of the major sources of clean energy. A large number of researches sponsored by government and private sectors have embarked on design, development, and manufacturing of proper devices to capture the energy of the tides in the past decades. Tides which are created by the gravitational forces of moon and sun on the oceans are repeated in cycles of 19 years. As the orbital motions of earth, sun, and moon are known, the tides are easily predicted during their cycle at any location on earth. This predictability of tides and tidal currents is one of the most important advantages of tidal energy compared to other forms of sustainable energy such as wave and wind energy. Tidal energy is usually harnessed in two ways. The first method of harnessing tidal power is to capture the potential energy of the tides by building a tidal barrage. A turbine is usually mounted on the barrage body to produce electricity as high tide occurs and water passes through the turbine channel and rotates the turbine's blades. On the other hand, when the water level is lowered because of the tide, the water captured behind the barrage tends to drain off due to the head difference between the water behind the tidal barrage and ocean water level. When the water is discharged from the barrage, it once again passes through the turbine's passages, rotates the turbine's blades and produces electricity. The largest plant built to work based on this concept is the Rance tidal barrage. It was built in 1967 and is rated at 240 MW. The main problem with the tidal barrage is that the creation of a massive obstruction in part of the ocean leads to a number of environmental issues. The second method of capturing tidal energy is to use special low-head turbines designed to capture the kinetic energy of tidal currents. Tidal currents are generated due to the head difference between two locations in the ocean. These currents can carry a significant amount of kinetic energy and their velocity can reach up to 20

knots in certain locations. There are two main types of tidal turbines designed to capture the kinetic energy of tidal currents, horizontal axis turbines and vertical axis turbines (Figure 1-8 and Figure 1-9).



Figure 1-8: Horizontal axis tidal turbine (Courtesy of Marine Current Turbine Ltd.)

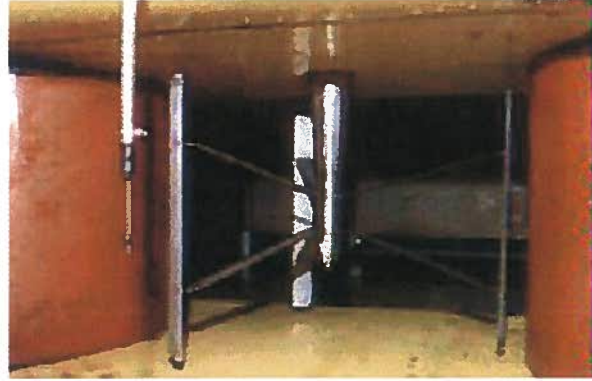


Figure 1-9: Vertical axis tidal turbine (Courtesy of Blue Energy Canada)

A horizontal axis turbine appears similar to a wind turbine with a number of blades rotating about a horizontal shaft. On the other hand, a vertical axis turbine consists of a few straight or helical blades distributed evenly about a vertical axis. The main benefit of the horizontal axis turbine design is as it is very similar to the wind turbines, its technology is sufficiently mature and well developed while the vertical axis turbine technology is not as far along in the design cycle. Also, the horizontal axis turbine has larger annual output power compare to the vertical axis ones due to its higher efficiency. In addition, both methods have a few negative environmental effects such as noise generation that can affect the sea life. However, large scale turbines with a low rotational speed reduce the noise level and environmental impact of the device.

However, the horizontal axis turbine is sensitive to the direction of the current while vertical axis turbines can work independently of the current direction. Also, the horizontal axis turbine needs a higher capital cost (1200-1400 GBP/KWh) compared to the vertical axis turbine with a capital cost of 400-900 GBP/KWh [10]. The operating cost is also higher for a horizontal axis turbine (20-50 GBP/KWh) while for a vertical axis turbine, the operating cost is estimated to be 14-20 GBP/KWh [10].

A large number of tidal sites have been assessed to be appropriate for mounting tidal turbines. The estimates show that if only 10% of the tidal current power were utilized, the country could have

generated about 1.5 GW of electricity which is about 6% of its current need [11]. Also, tidal currents in Florida have the potential to produce 25 GW of electricity [11].

Tidal energy research in Canada dates back to 1919 when strong tidal currents in New Brunswick triggered thoughts about harnessing tidal energy to produce electricity. There are many potential sites on both eastern and western coasts of Canada such as Ungava Bay in Quebec, the Bay of Fundy in New Brunswick, and Queen Charlotte Islands in British Columbia. Figure 1-10 shows the potential sites in Canada. To date, thirteen potential sites have been identified along the coast of British Columbia. Among these sites, Portland Canal, Jervis and Sechart Inlet, and the Observatory Inlet have the largest output with tide amplitudes of 5 m, 3.5 m, and 4.7 m respectively. A study conducted at Observatory Inlet, close to Prince Rupert showed that the capital cost required for a 2.03 MWh output is \$2,498,000 CAD and for a 167 KWh plant is \$243,000 CAD. This study shows that the tidal power is not economically beneficial in British Columbia, especially because of the relatively low power price in British Columbia which is about one-seventh of tidal power [11].

The main problem with vertical axis turbines is their low efficiency as well as large torque ripple that can cause mechanical design problems and affect the durability of the design. The focus of the current research is to increase the power generated by the turbine by placing a few of the ducts around the turbine. The shape of these ducts and their effect on the performance of the turbine is studied in the current research. Duct shape optimization is obviously one of the approaches to increase the power generated by the turbine. Rotor optimization is another key aspect of the project which is also under study at Naval Architecture Lab at the University of British Columbia.

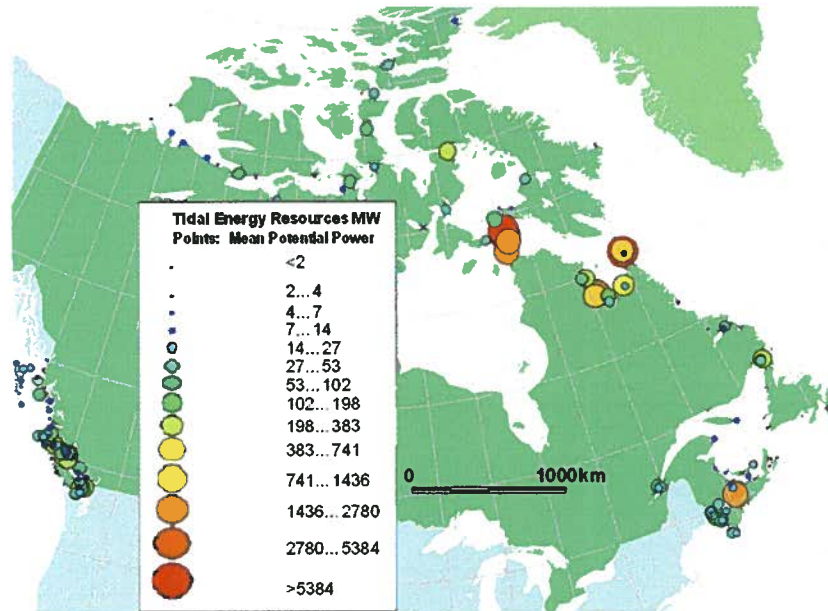


Figure 1-10: Tidal sites of Canada [12]

1.4 Modeling Approaches

Development and optimization of tidal turbines require accurate and time-efficient mathematical models. Based on the computational tools available, different models with different computational costs were developed and applied for optimization and analysis purposes. These models range from computationally inexpensive but low in accuracy momentum models, to three-dimensional RANS models of the turbine with all the physical details taken into account. It can be concluded from a comprehensive literature review that there are two families of potential flow codes and RANS codes to numerically model a tidal turbine. Some of these methods were applied to wind turbines sharing a similar concept for operation. The RANS modeling is the subject of the current research and will be extensively discussed in the next chapters. In this section, different potential flow codes used for numerical modeling of a vertical axis turbine are briefly reviewed and the advantages and disadvantages of each model are discussed. More detailed information about different aerodynamic models used for prediction of a straight-bladed Darrieus turbine can be found in [13, 14]. There are three main categories of modeling approaches to numerically simulate and predict the performance of a vertical axis tidal turbine (also known as Darrieus turbine) as described below.

- Potential flow models
 - Momentum Models
 - Single stream tube
 - Multiple stream tube
 - Double-Multiple stream tube
 - Discrete Vortex Method
 - Fixed Vortex Method
 - Free Vortex Method
 - Cascade Model
- RANS model
- Experimental model

1.4.1 Potential Flow Modeling

As shown in Figure 1-11, the incoming flow is from the left hand side of the turbine plane. When the free-stream flow reaches the blade, it has a velocity of V_a . The resultant velocity is obtained using the angular velocity of the blade and the upstream velocity. Also, the normal velocity (V_n), tangential velocity (V_t), and angle of attack can be calculated as follows:

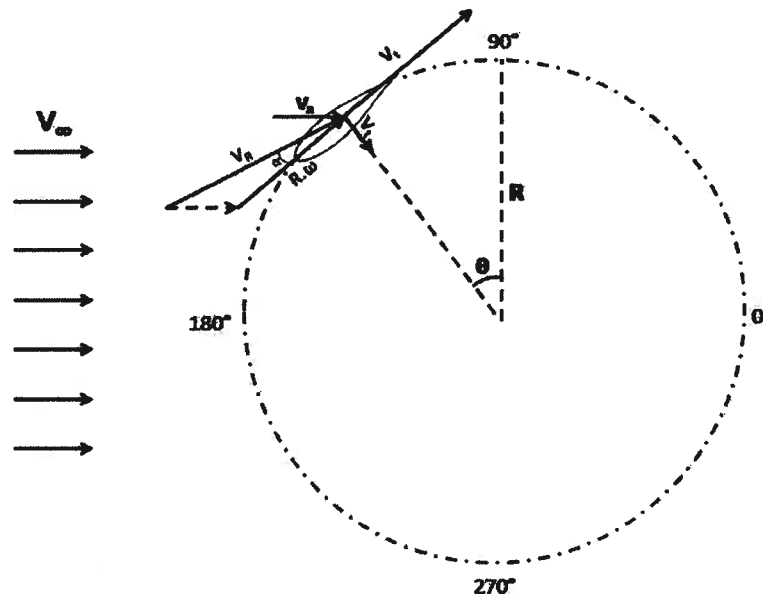


Figure 1-11: Aerodynamic model of a free-stream vertical axis turbine

$$V_t = R\omega + V_a \cos(\theta) \quad \text{Equation 1-1}$$

$$V_n = V_a \sin(\theta) \quad \text{Equation 1-2}$$

$$V_R = \sqrt{(V_t^2 + V_n^2)} \quad \text{Equation 1-3}$$

$$\alpha = \text{atan}\left(\frac{V_n}{V_t}\right) \quad \text{Equation 1-4}$$

All different potential flow models developed for the analysis of the turbine apply a method to estimate the direction and magnitude of the induced velocity (V_a). When induced velocity is obtained, the normal and tangential forces can usually be calculated using the experimental values of lift and drag coefficients. The tangential force can then be used to calculate the torque generated at each orbital position by a single blade.

$$C_t = C_l \sin(\theta) - C_d \cos(\theta) \quad \text{Equation 1-5}$$

$$C_n = C_l \cos(\theta) + C_d \sin(\theta) \quad \text{Equation 1-6}$$

$$F_t = \frac{1}{2} \rho A_{tfa} V_R^2 C_t \quad \text{Equation 1-7}$$

$$T_{s.b.}(\theta) = F_t(\theta) \cdot R \quad \text{Equation 1-8}$$

The instantaneous torque can be calculated by adding up the effect of all N blades of the turbine.

$$T(\theta) = \sum_{i=1}^N T_{sb}(\theta) \quad \text{Equation 1-9}$$

The average power can be obtained by integrating the instantaneous torque over the blades path. The power generated by the turbine is obtained using the average torque and angular velocity of rotation.

$$T_{avg} = \int_0^{2\pi} T(\theta) d\theta$$

Equation 1-10

$$P = T_{avg} \omega$$

Equation 1-11

In the following section, different approaches on modeling a vertical axis turbine will be briefly described, and the advantages and disadvantages of each approach will be discussed.

1.4.1.1 Momentum Models

Momentum models are based on the Glauert's actuator disc theory and blade element theory. The concept used in these models is that the total change in axial momentum across the actuator disc is equal to the aerodynamic forces exerted on the blades in the axial direction. This force is also equal to the average pressure difference across the disc. Bernoulli's equation is then used in each stream tube to obtain the wake velocity. The main momentum models developed are single stream tube model, multiple stream tube model, and double-multiple stream tube model as shown in Figure 1-12 through Figure 1-14.

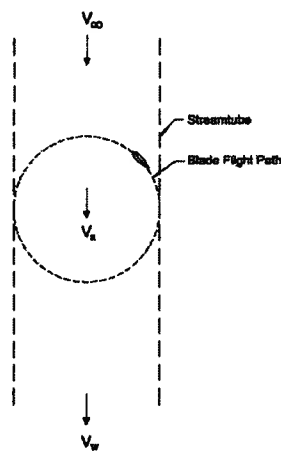


Figure 1-12: Single stream tube model [14]

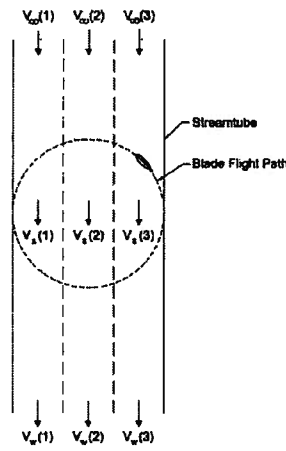


Figure 1-13: Multiple stream tube model [14]

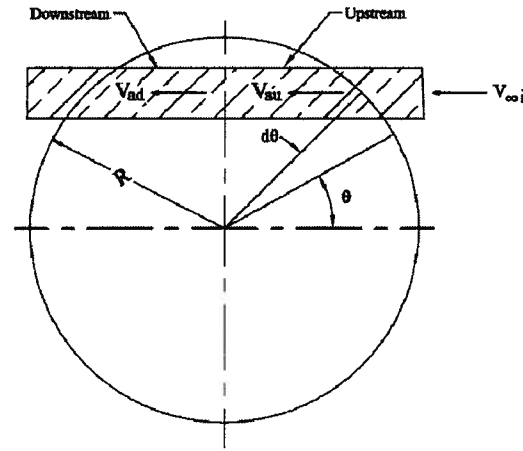


Figure 1-14: Double multiple stream tube model [14]

1.4.1.1.1 Single Stream Tube

Presented by Templin in 1974 [15], this model is the simplest approach to calculate and predict the performance of a vertical axis turbine. In this model, it is assumed that the turbine is enclosed in one single tube of stream lines and the velocity across the disc is assumed to be constant. It is also assumed in this model that a single blade exists and the chord length of this blade is equal to the sum of all the

chord lengths of the real turbine. Using Glauert's actuator disc theory, one can calculate the uniform velocity across the rotor.

$$V_a = \frac{(V_\infty + V_w)}{2} \quad \text{Equation 1-12}$$

By equating the stream-wise drag force (F_D) with change in axial momentum, one can obtain the velocity across the rotor as a function of non-dimensional rotor drag coefficient.

$$\frac{V_a}{V_\infty} = \left(\frac{1}{1 + \frac{C_{DD}}{4}} \right) \quad \text{Equation 1-13}$$

C_{DD} is the rotor drag coefficient and can be calculated using Equation 1-14. The rotor drag force (F_D) can be also calculated by integrating the axial force using experimental aerodynamic characteristics of the blades. V_a obtained from Equation 1-13 can be used to calculate the resultant velocity and angle of attack at each location. The average power can be calculated by using Equation 1-1 and Equation 1-2.

$$C_{DD} = \frac{F_D}{\frac{1}{2} \rho A_{tfa} V_a^2} \quad \text{Equation 1-14}$$

1.4.1.1.2 Multiple-Stream Tube

This model was developed in 1974 by Wilson and Lissaman [16]. As shown in Figure 1-13, a single stream tube is replaced by multiple adjacent stream tubes which are aerodynamically independent. Similar to the single stream tube model, the momentum theory and the blade element theory are used together for each stream tube and different induced velocities (V_a) are obtained for each stream tube. The induced velocity can be obtained using Equation 1-15 where k is a parameter determined iteratively.

$$\frac{V_a}{V_\infty} = 1 - \left(\frac{K}{2} \cdot \frac{NC}{R} \cdot \frac{R\omega}{V_\infty} \cdot \sin(\theta) \right) \quad \text{Equation 1-15}$$

In 1975, Strickland developed a more complicated model for multiple stream tube, which accounts for the effect of drag and momentum change along each stream tube as well [17]. Although Strickland's model is more accurate, Wilson's model gives a faster convergence due to simpler physics of the model.

Later in 1975, Muraca presented a model [18], which included the effect of airfoil geometry, struts, blade aspect ratio, solidity, and also flow curvature around the blade on the performance. The study showed that the flow curvature effect is not significant at low chord to radius ratios. Sharpe presented another model in 1977 [19] which took the Reynolds number effect into account. In 1980, another model was developed by Sharpe and Read for a lightly loaded, high aspect ratio bladed turbine [20]. The expansion of stream tubes are incorporated in this model, thus improving the calculation of instantaneous aerodynamic forces and the induced velocities compared to other multiple stream tube models.

1.4.1.1.3 Double-Multiple-Stream-Tube

The original idea of the Double Multiple Stream Tube concept was introduced by Lapin [21] in 1975. In 1981, Paraschivoiu developed it as a mathematical model for prediction of the performance of Darrieus wind turbines [22, 23]. Similar to Multiple Stream tube model, the surrounding stream tube of the turbine is divided into several small strips. As shown in Figure 1-14, the improvement to the multiple stream tube model was made by introducing the upstream induced velocity and downstream induced velocity at the front and rear part of the turbine respectively. The upstream and downstream induced velocities can be calculated using Equation 1-16 and Equation 1-17.

$$V_e = V_\infty \left(\frac{2V_{au}}{V_{\infty i}} - 1 \right) = V_{\infty i} (2u_u - 1) \quad \text{Equation 1-16}$$

$$V_{ad} = u_d V_e = u_d (2u_u - 1) V_{\infty i} \quad \text{Equation 1-17}$$

In the above equations, u_u and u_d are interference factors for upstream and downstream half-cycles respectively and can be defined as follows:

$$u_u = \left(\frac{V_{au}}{V_{\infty i}} \right) \quad \text{Equation 1-18}$$

$$u_d = \left(\frac{V_{ad}}{V_e} \right) \quad \text{Equation 1-19}$$

V_{au} and V_{ad} are induced velocity at upstream and downstream half-cycles and $V_{\infty i}$ is the upstream velocity and can be different at different heights to include the effect of wind shear in wind turbines. This model predicts the generated power more accurately than single and multiple stream tube models. However, the power is over-predicted for high solidities and convergence problems occur in some cases.

1.4.1.2 Discrete Vortex Models

This model was first introduced by Larsen [24] in 1975 to predict the two-dimensional performance of a cyclogiro windmill. Fanucci and Walters [25] applied the model to a straight-bladed vertical axis turbine. In 1979, Strickland developed the three-dimensional model using the vortex method and incorporated aerodynamic stall in his model. Research was conducted at UBC [26] to apply the model to a vertical axis tidal turbine. The results presented were in good agreement with experimental results especially at high TSR's. It is usually said that the vortex model predicts the performance of the turbine more accurately compared to the stream tube models at higher computational cost. However, with the recent improvements in computational power, the method is fairly reliable and economical.

There are two subdivisions of vortex model: fixed vortex and free vortex. The vortex method is a potential flow solution of the flow field which takes the effect of vorticity shed from the blades into account.

1.4.1.2.1 Fixed Vortex Method

As shown in Figure 1-15, the blade is replaced with a bound vortex filament. The strength of the vortex filament is calculated using the Kutta-Joukowski law and experimental value of lift per unit span.

$$L = \rho V_{\infty} \Gamma \quad \text{Equation 1-20}$$

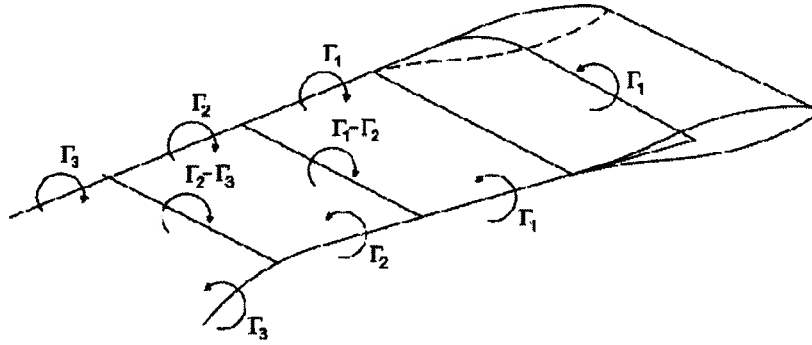


Figure 1-15: Blades are replaced with vortex filaments in vortex methods [14]

The trailing and wake vortices can be obtained using Helmholtz and Kelvin's theorems. The induced velocity by a vortex filament at any location in the flow field can be calculated using the strength of the vortex sheet. The change in the axial flow can be calculated using the strength of the vortex sheets. Therefore, the velocity field can be obtained by superimposing the upstream velocity and the induced velocity by the blades. Knowing the velocity at each location the angle of attack seen by the blades can be determined. The experimental blade data can then be used to calculate the torque at each azimuth angle and consequently the generated power.

1.4.1.2.2 Free Vortex Method

The fixed vortex method suffers from the fact that vortex sheets are fixed and independent of time. This also results in the inability of this method to predict the velocity components normal to the free stream. In the free vortex method, proposed by Strickland [27], the blade is again replaced by a vortex and the vortex strength is calculated using Kutta-Joukowski formulation for lift. The stream-wise and normal component of velocity can be obtained using Biot-Savart law. Using Kelvin's theorem, the change in circulation of the blades will result in the change of the strength of the vorticity shed from the blades (Equation 1-21)

$$\Gamma_{SV} = -(\Gamma_B^n - \Gamma_B^{n-1}) \quad \text{Equation 1-21}$$

Strickland also proposed a method to replace the vortex core strength with a linear function to solve the singularity problem. As mentioned above, the free vortex method is capable of including the change in the direction of velocity vector upstream and downstream of the blades resulting in a more accurate calculation of angle of attack. Knowing the angle of attack and experimental values of lift and drag, the

tangential force, the torque generated by the blades can be calculated. There are a few problems associated with the discrete vortex method. These models are not able to model the drag induced vortices such as vortex shedding from the shaft. They also lack a reliable dynamic stall model which is more crucial for low tip speed ratios. In addition, the experimental data of the blade's profile is not always available. Their main capability is in rotor optimization and optimization of configurations with simple geometries and mild separation.

1.4.1.3 Cascade Model

A cascade is defined as a series of identical, parallel, and equally spaced blades. The cascade concept is widely used in turbomachinery analysis and modeling. The cascade concept was first applied to a vertical axis wind turbine by Hirsch and Mandal in 1987 [28]. In the proposed method, the aerodynamic characteristic of each blade is calculated independently for upstream and downstream blades (similar to the double multiple stream tube). The effect of local angle of attack and Reynolds number is also included in this model. After calculation of local angle of attack and velocity, the blades are placed linearly and in tandem (like a linear cascade) as shown in Figure 1-16.

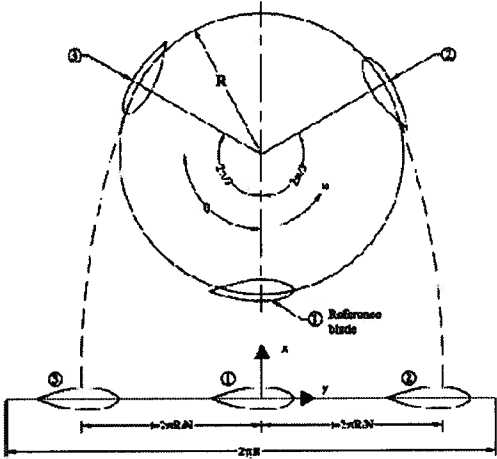


Figure 1-16: Cascade Model approach [10]

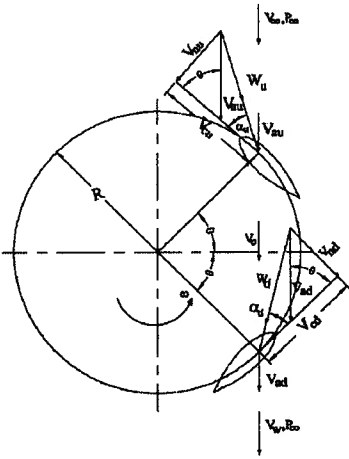


Figure 1-17: Upstream and downstream velocities in Cascade Model [10]

The cascade plan is assumed to be normal to the blades' axis of rotation. In the cascade configuration, the upstream and downstream induced velocities are expressed using Equation 1-22 and Equation 1-23.

$$\frac{V_{au}}{V_{\infty}} = \left(\frac{V_e}{V_{\infty}}\right)^{k_i} \quad \text{Equation 1-22}$$

$$\frac{V_{ad}}{V_e} = \left(\frac{V_w}{V_e}\right)^{k_i} \quad \text{Equation 1-23}$$

V_e and V_w are the wake velocities in the upstream and downstream sides of the turbine respectively as shown in Figure 1-17. The value of k_i is determined using empirical relations obtained from experiments. Hirsch and Mandal proposed Equation 1-24 for determination of the exponent (k_i). In this equation, σ is solidity ratio.

$$k_i = (0.425 + 0.332\sigma) \quad \text{Equation 1-24}$$

Mandal and Burton later incorporated dynamic stall and flow curvature effects into account [29]. This model found to be more accurate than the stream tube models. Although it is not as accurate as free vortex models, it is computationally cheaper and has no convergence problems. It works properly for high tip speed ratios and high solidities as well.

1.4.2 RANS Modeling

With the revolutionary improvements in the computer technology in the past two decades, conducting CPU-intensive tasks has presently become much more feasible. At the time of the vortex method invention, the high computational cost of the model had been described as the main problem. Today, with modern computational tools, running a vortex method code takes no longer than a few minutes. With the use of powerful computers and parallel processing technology these days, RANS simulations are becoming more popular in industrial and academic sectors. Wind and tidal turbine optimization tasks using RANS simulations are extensively used these days [30]. Conducting RANS simulations can provide the user with a valuable insight into the flow field and can facilitate the decision making process for optimization. In spite of the potential flow codes, RANS simulations do not need any external data (such as experimental lift and drag). They can include separation from the foils and drag induced vortices from the turbine's shaft. Also, they are able to simulate dynamic stall phenomenon (although it is not perfect due to the imperfection of turbulence models). RANS modeling is also a powerful tool for complex geometries in which case vortex methods cannot be used. On the other hand, RANS simulations for tidal turbines still suffer from high computational cost and time. Three-dimensional simulations cannot be conducted on single computers and can only be done using a network of several

nodes. The other problem with RANS simulations is turbulence and separation modeling which will be addressed in the turbulence modeling section in Chapter 2.

1.4.3 Experimental Approach

Experimental modeling is still the most reliable source for data. Most of the physics of the problem can be modeled and measured accurately. However, it suffers from high cost and design time. Also, the technical problems concerned with experiments always exist and should be addressed properly. The other problem of experimental work is that flow visualization and access to different quantities in the flow field is not easy.

A series of experimental tests were conducted at the University of British Columbia towing tank during 2006-2007. The results and the problems associated with those experiments will be discussed later in Chapter 4 and Chapter 6. The current research at the University of British Columbia is a continuation of the work started by the Vancouver based company, Blue Energy Canada. This company, formerly registered as Nova Energy started its research and development in early 80's in the field of application of Darrieus concept to extract tidal energy. The research was supervised by the veteran aerospace engineer, Barry Davis. A Series of experimental tests was conducted at NRC flume tank and the results were documented in a number of reports as presented in Table 1-1.

Table 1-1: Reports on experiments conducted by Barry Davis from Nova Energy in 1980's

Report Title	Synopsis
NEL-002: Water Turbine Model Trials [31]	Flume tank tests of vertical and horizontal axis water turbines.
NEL-021: Ultra Low Head Hydroelectric Power Generation Using Ducted Vertical Axis Water Turbines [32]	Vertical axis water turbine flume tank tests with caissons, walls, and vane duct configurations.
NEL-022: Ultra Low Head Hydroelectric Power Generation Using Ducted Vertical Axis Water Turbines [33]	Continuation of NEL-021 with a more robust model.
NEL-038: Research and Development of a 50kW to 100kW Vertical Axis Hydro Turbine for a Restricted Flow Installation [34]	Installation of 70 kW turbine within a dam in Nova Scotia.
NEL-070: The Ducted Vertical Axis Hydro Turbine for Large Scale Tidal Energy Applications [35]	Investigates application of vertical axis turbine in a 474 turbine tidal fence.
NEL-081: Commissioning and Testing of a 100kW Vertical Axis Hydraulic Turbine [36]	Examined repaired and enhanced version of model in NEL-038.

2. CFD Simulation of a Free-Stream Vertical Axis Tidal Turbine

In the first phase of the project, a three-bladed free-stream turbine was simulated for a range of current velocities and tip speed ratios presented in

Table 2-1. The tip speed ratio (TSR) is a non-dimensional number representing the ratio of the tangential velocity of the turbine's blades to the current velocity as defined in Equation 2-1.

$$TSR = \frac{R \cdot \omega}{V}$$

Equation 2-1

Table 2-1: Simulation Plan for a free-stream three-bladed turbine

Current Velocity (m/s)	TSR	RPM
1	2.25	47.0
1	3.5	73.1
1.5	2	62.7
1.5	2.25	70.5
1.5	2.5	78.3
1.5	2.75	86.1
1.5	3	94.0
2	1.75	73.1
2	2.25	94.0
2	2.75	114.9
2	3.25	135.8
2	3.75	156.6

2.1 Geometry definition

The dimensions of the turbine, summarized in Table 2-2, were chosen to reflect the model tested in the tow tank shown in Figure 2-1.

Table 2-2: Geometric specifications of the turbine's model

Blade's profile	NACA 63 ₄ -021
Diameter	0.9144 m
Blade's Height	0.6858 m
Number of Blades	3
Arms connection	Quarter chord
Shaft diameter	0.0482 m

The geometry used for the simulations, shown in Figure 2-2 and Figure 2-3, was a 2D version of the tested turbine; therefore, the arms and arm connections were not included. The boundaries on the computational domain represented in the 2D model consist of a velocity inlet on the left, an outlet on the right, and two slip walls at the top and the bottom of the domain representing the tow tank walls. Figure 2-3 shows the blades, the circular shaft in the center, and two concentric circles used as an interface between the moving mesh section and the stationary sections.

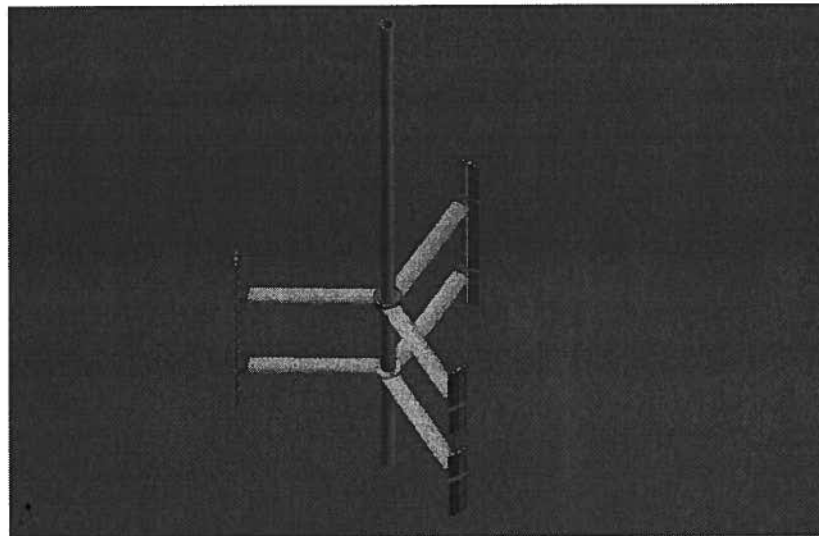


Figure 2-1: Tow tank model

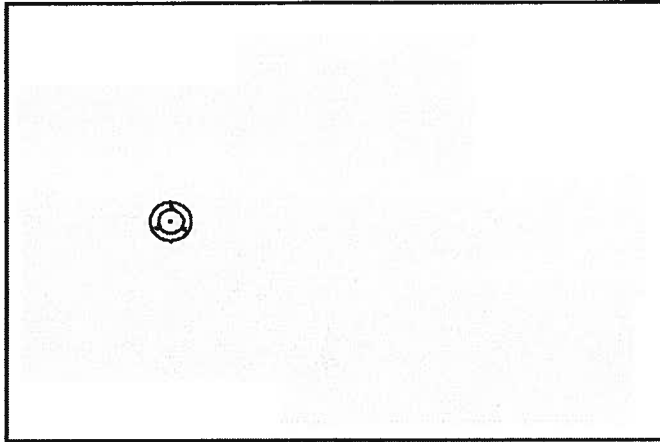


Figure 2-2: Geometry of the physical domain including inlet, outlet, tow tank walls, blades, shaft, and interfaces

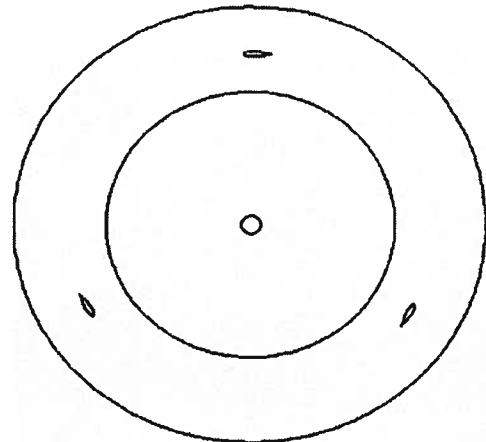


Figure 2-3: Geometry of the blades, shaft, and interfaces

The airfoil used for the blades is a five-digit NACA Series, NACA 63₄-021 (Figure 2-4). This airfoil was chosen based on previous NRC reports [31-36].

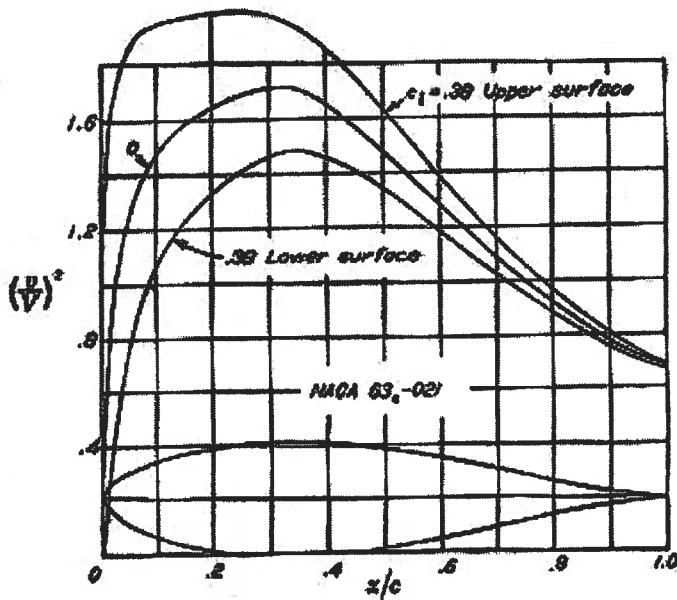


Figure 2-4: NACA 63₄-021 profile and coordinates

x (per cent c)	y (per cent c)	$(w/V)^2$	w/V	$\Delta\alpha/V$
0	0	0	0	1.439
0.5	1.563	0.373	0.621	1.235
0.75	1.937	0.554	0.751	1.186
1.25	2.527	0.725	0.851	1.034
2.5	3.577	1.010	1.006	0.843
5.0	5.055	1.290	1.122	0.653
7.5	6.182	1.394	1.181	0.550
10	7.080	1.457	1.210	0.454
15	8.441	1.592	1.262	0.302
20	9.410	1.656	1.280	0.235
25	10.053	1.698	1.303	0.201
30	10.412	1.721	1.312	0.258
35	10.500	1.709	1.307	0.225
40	10.298	1.694	1.298	0.198
45	9.854	1.678	1.256	0.173
50	9.206	1.479	1.216	0.150
55	8.290	1.280	1.175	0.120
60	7.441	1.281	1.132	0.113
65	6.896	1.180	1.086	0.096
70	5.290	1.084	1.041	0.081
75	4.160	0.994	0.997	0.068
80	3.054	0.911	0.954	0.057
85	2.091	0.839	0.916	0.046
90	1.113	0.774	0.880	0.036
95	0.202	0.721	0.849	0.022
100	0	0.676	0.822	0

L.E. radius: 2.680 per cent c

2.2 Grid Generation and Boundary Conditions

In order to conduct a CFD simulation, the domain needs to be discretized into very small sections called cells or elements. Discretization of the domain allows for the conversion of the Partial Differential Equations (PDE's) to algebraic equations which can be solved numerically through an iterative process. The PDE's that need to be discretized are continuity, momentum equation (in X and Y direction), energy equation (when using of a coupled solver), and the turbulence equation(s).

To calculate the turbine performance, the torque generated by the blades was recorded for each simulation as a function of azimuth angle. The average power was then calculated based on the average torque over a cycle and the angular velocity of rotation of the turbine's blades using Equation 2-2.

$$P = f(T_{avg}, \omega) = T_{avg} \cdot \omega \quad \text{Equation 2-2}$$

The torque itself is a function of lift and drag forces generated by the blades (Equation 2-3). Since the variation of pressure in the boundary layer along the normal axis to the surface is negligible, the pressure distribution and hence the lift force can be predicted accurately even using a potential flow code. The complicated task in calculating the forces exerted on the blade is to accurately predict the drag force. This requires an accurate solution of the boundary layer developed over the blades.

$$T = f(L, D, \alpha) = L \sin(\alpha) - D \cos(\alpha) \quad \text{Equation 2-3}$$

An accurate prediction of drag on the blades, especially for unsteady separated flow requires a high quality fine grid around the airfoils. Thus, a very fine C-shape structured grid was used to resolve the flow around the airfoil and the wake structure as shown in Figure 2-5. The number of nodes used on the airfoil surface and the wake was 240 and 120 respectively and the number of layers used to form the C-shape mesh was 80 with a growth ratio of 1.05. The node distribution was dense at the leading edge and trailing edge of the airfoil where high velocity and pressure gradients exist.

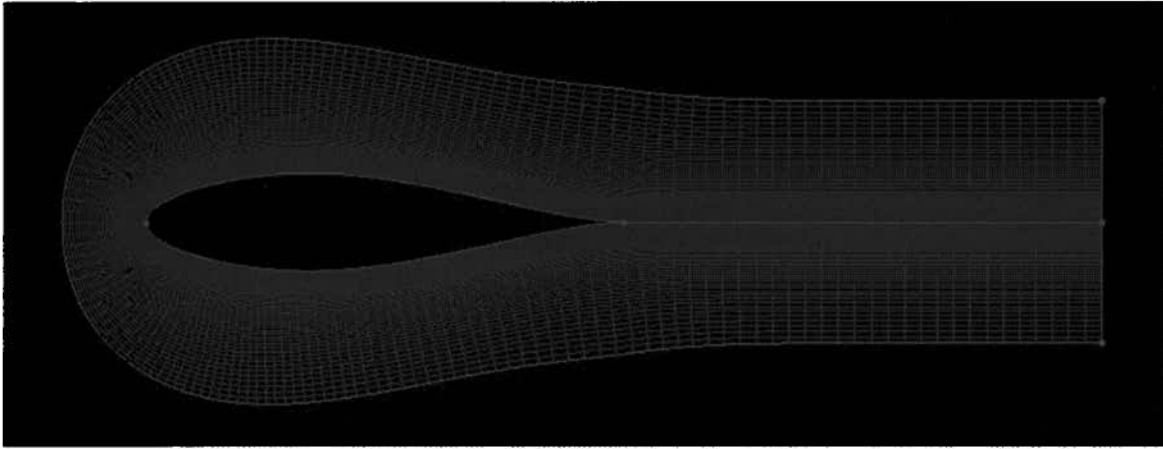


Figure 2-5: Structured fine grid used around the blades

The size of the grid required adjacent to the blades is dependent on the thickness of the turbulent boundary layer. The boundary layer profile shown in Figure 2-5, can be divided into three different regions: the viscous sublayer, buffer layer and fully-turbulent layer. The viscous sublayer is the innermost layer in which the viscous forces are dominant and the value of the non-dimensional cell height, y^+ (defined by Equation 2-4 and Equation 2-5) is below 5.

$$y^+ = \frac{\rho u_\tau y}{\mu} \quad \text{Equation 2-4}$$

$$u_\tau = \sqrt{\frac{\tau_w}{\rho}} \quad \text{Equation 2-5}$$

In the buffer layer, the effect of viscosity and turbulence is of the same order and the y^+ value is between 5 and 60. Fully-turbulent layer, also called the log-law region, is where the effects of turbulence are dominant and the velocity profile can be approximated using Equation 2-6.

$$\frac{u}{u_\tau} = 2.5 \ln \left(\frac{u_\tau y}{\nu} \right) + 5.45 \quad \text{Equation 2-6}$$

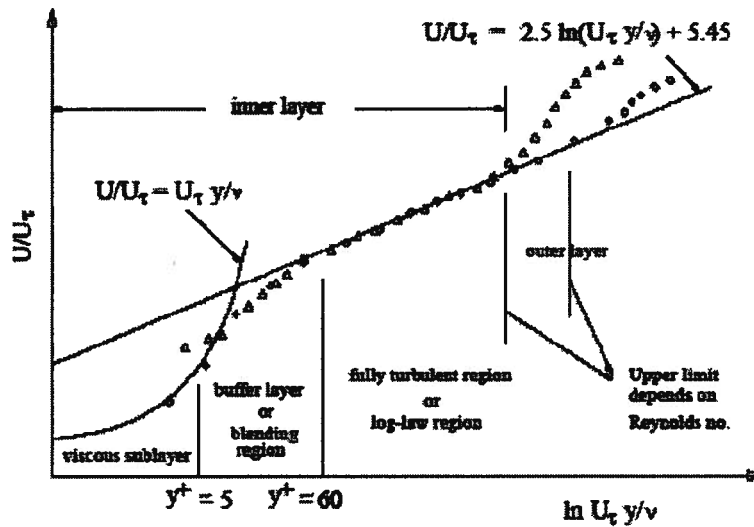


Figure 2-6: Turbulent boundary layer profile [37]

It is important to note that y^+ value is not only a function of the cell height adjacent to the wall, but also is a function of the Reynolds number. Since the Reynolds number over a blade is dependent on its orbital position, it changes as a function of the azimuth angle. Thus, the y^+ value can only be approximated based on the maximum Reynolds number seen by the blade and using the correlations for known flows such as the turbulent flow over a flat plate given by Equation 2-7.

$$y^+ = 0.172 \left(\frac{y}{\ell}\right) Re^{0.9} \quad \text{Equation 2-7}$$

The required cell height adjacent to the turbine blade was therefore computed using Equation 2-7 by imposing a required y^+ value of 2 to ensure that there is adequate number of cells to resolve the viscous sublayer. Since the method of determining the cell height is based on an approximation, the y^+ value was monitored during the simulations to ensure that it was constantly kept in an acceptable range. Based on Equation 2-7, the height of the cells adjacent to the wall was determined and set to $5.08 \cdot 10^{-6}$ m. This cell height yields a $y^+ = 2.16$ which is still below 5 with a safety factor of 2.

Also, as shown in Figure 2-7, the same type of grid was used for the flow field around the shaft to properly solve the vorticity shed from the shaft. Because the flow velocity over the shaft is lower than the velocity over the blades and hence the shaft Reynolds number is lower, a larger cell height is allowed adjacent to the shaft wall. The cell height used for the shaft was 12.7×10^{-6} m which yielded a y^+ value of 1.56.

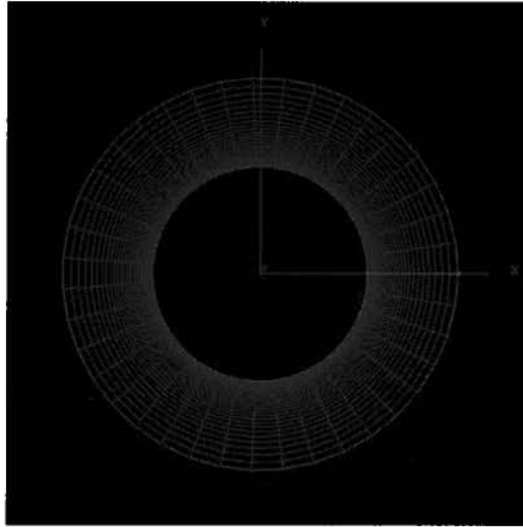


Figure 2-7: Structured fine grid around the shaft

For the rest of the domain, a triangular unstructured grid was used as can be seen in Figure 2-8 and Figure 2-9. As shown in these figures, the mesh density is high around the turbine region and becomes lower far from the turbine zone. Because of the complexity of the flow in the wake of the turbine, the mesh density is higher downstream than upstream of the turbine. Also, the grid was refined in the areas at which the pressure gradient was high.

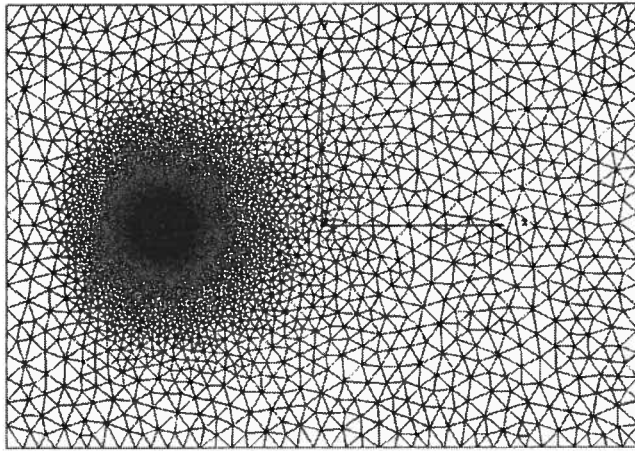


Figure 2-8: Unstructured grid of the domain

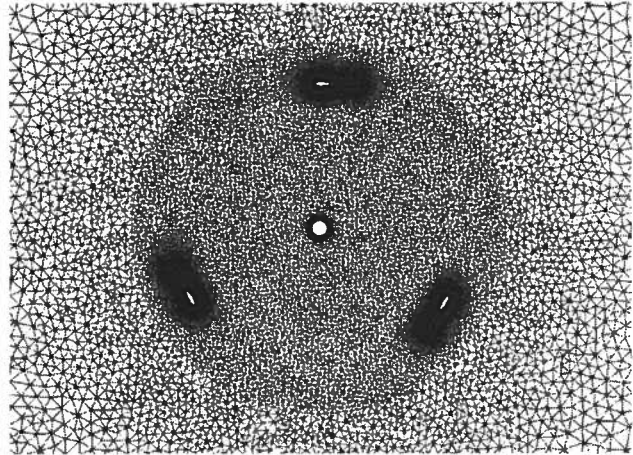


Figure 2-9: Unstructured grid around the blades and the shaft

For a CFD problem, the solution needs to be independent of the grid. Hence, a grid refinement study is a necessary component of every CFD simulation. A grid refinement study can be easily done for a steady-state problem. However, for an unsteady problem, a target parameter should be selected and compared for different grid densities. In the current research, the average power generated by the turbine over each cycle was chosen as the target parameter and was compared for three different mesh densities. The mesh densities generated for the free-stream turbine model are presented in Table 2-3. It should be noted that the refinement factor chosen for both free-stream and ducted turbine models was 1.5. Although the industry standard refinement factor is $\sqrt{2}$, a factor of 1.5 enables the study of a larger range of cell numbers. This could result in finding a smaller number of cells with acceptable accuracy.

Table 2-3: Grid densities used for grid refinement study

Grid Density	Number of Cells
Coarse	144,641
Medium	220,803
Fine	328,947

The simulations were conducted for different mesh densities at the same inlet velocity of 1.5 m/s and a TSR of 2.75. This TSR was selected because a relatively severe separation occurs as the angle of attack

seen by the blades is relatively high. Also, at this TSR the blade velocities are high and a finer grid is required. The results obtained for different grids are presented in Table 2-4 and Figure 2-10.

Table 2-4: Results of the grid refinement study

Grid	Average Power Per Cycle (Watts)
Coarse	318.3
Medium	390.7
Fine	389.7

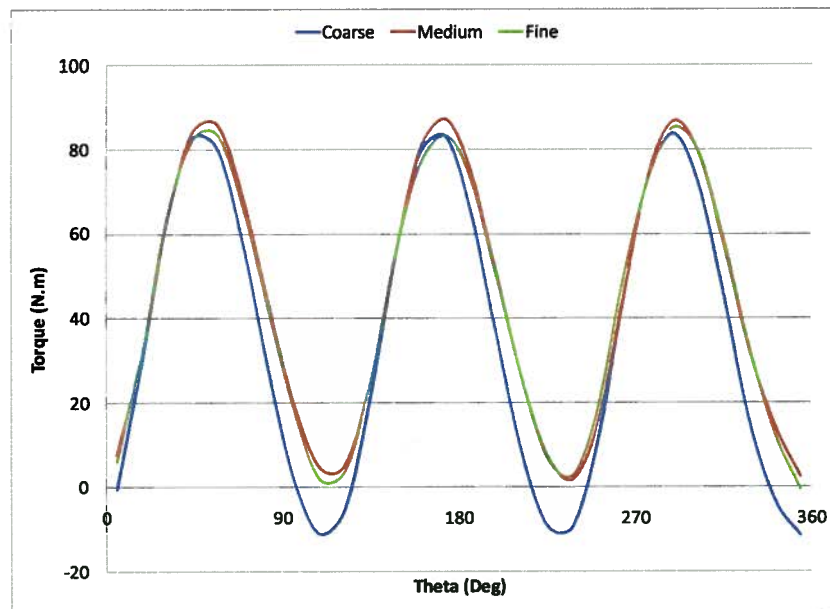


Figure 2-10: Grid convergence results for a free-stream turbine at TSR=2.75

2.3 Domain Size Study

As the final product would be installed in the free stream of the ocean currents, it is necessary to conduct the simulations in a large domain in which the boundaries have minimal effect on the solution. This was the same strategy that was tried to be achieved in the experiments. In order to quantify the effect of tow tank walls on the performance of the turbine, a parameter is defined in Equation 2-8 which is called blockage ratio.

$$\varepsilon_b = \frac{A_{tfa}}{A_{tsa}}$$

Equation 2-8

Blockage Ratio is basically the ratio of the projected turbine area to the cross sectional area of the tow tank. The Blockage Ratio concept is shown in Figure 2-11 and Figure 2-12 for 2D and 3D models respectively.

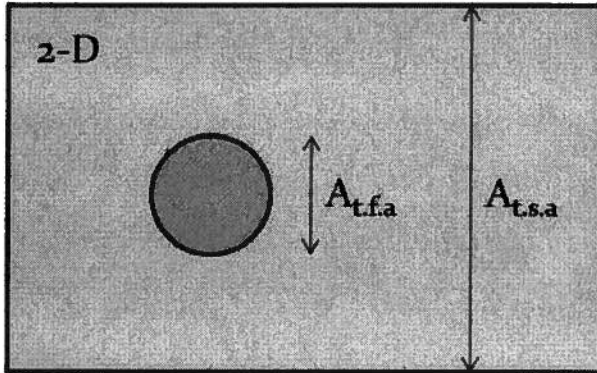


Figure 2-11: Definition of 2D blockage ratio

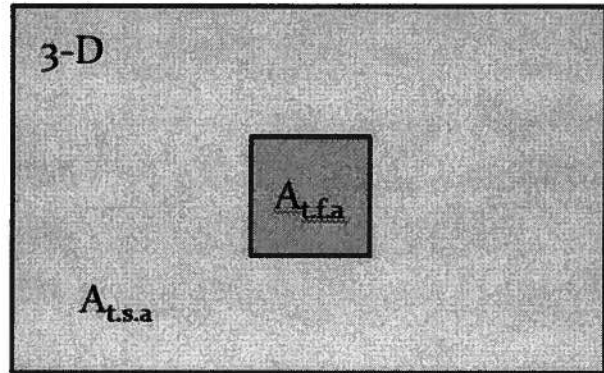


Figure 2-12: Definition of 3D blockage ratio

For the conducted experiments as a part of the current research in the Naval Architecture Lab, the blockage ratio was about 7% which implies that the test conditions can be considered as free stream conditions. Thus, the same blockage ratio was also used for the simulations. However, to ensure that the domain size is large enough to simulate a free stream condition, a domain size study was conducted for different domain sizes and the results obtained from those simulations approved that the domain size is large enough to represent the free stream conditions. The main concern in adjusting each factor is to minimize the domain boundaries effect on the turbine performance. On the other hand the number of cells in the domain is another concern about the computational cost of the simulations. These concerns resulted in choosing different upstream, downstream and side distances as presented in Table 2-5, and the simulations were conducted to ensure the solution independency on the domain size.

Table 2-5: Domain size study results

Case Name	Domain Width (m)	Distance From Upstream (m)	Distance From Downstream (m)
A	2.54	1.27	2.54
B	7.62	2.54	10.16
C	7.62	3.81	10.16
D	7.62	5.08	10.16
E	10.16	5.08	10.16
F	10.16	6.35	10.16
G	12.7	5.08	10.16

2.3.1 Domain Width Effect

The small width of the domain (2.54 m which corresponds to a blockage ratio of 35%) has a large effect on turbine performance due to blockage and flow restriction. These tests do not accurately model free-stream results, but may be consistent with the flume tank testing results. The trend is such that smaller width domains, naturally, reduce the Betz effect and channel more flow energy through the turbine blades, thus increasing their power. Once the domain is on the order of 10 m wide, there are negligible effects on the flow from the tank walls and free-stream flow can be assumed to be accurately modeled. From 7.5 m to 10 m, the steady state average torque drops by approximately 0.5 N.m, and from 10 m to 12.5 m, the drop appears much lower and the flow conditions can be assumed as free stream conditions. The results of the domain width study for cases A, D, E, and G are shown in Figure 2-13.

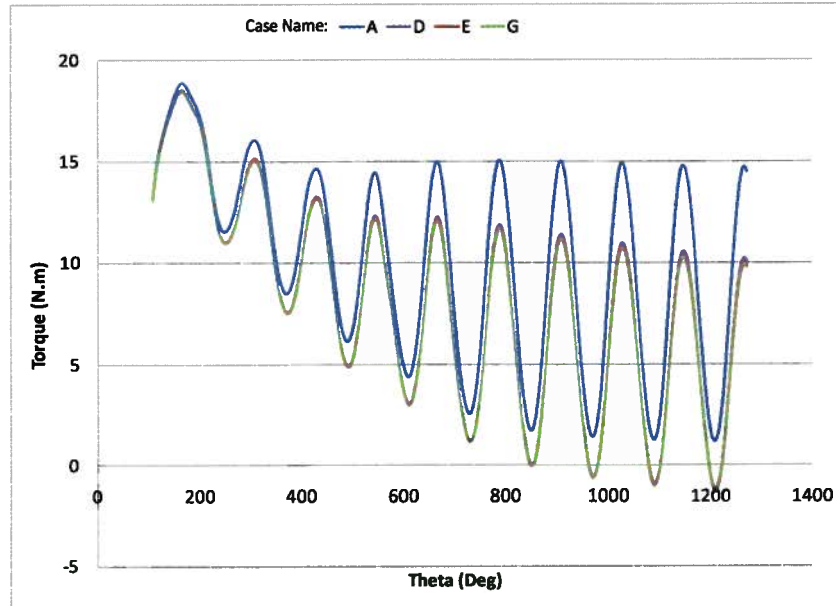


Figure 2-13: Domain width effect on the torque generated by the turbine

2.3.2 Upstream Distance

It appears that, on larger domains where flow eddies and vortices can be resolved, the upstream distance between the turbine and inlet has as a dramatic effect on the flow characteristics as the domain width. If insufficient space is provided, water cannot flow around the turbine as it would in free-stream conditions as the flow enters the domain perpendicular to the inlet boundary. It can also cause a reverse flow at the inlet if the inlet is too close to the turbine. It appears that lengths larger than 3.81 m (more than 4 times of the turbine diameter) are required for adequate flow pattern formation prior to reaching the turbine, while smaller values lead to numerical errors and an artificially increased turbine performance. As can be seen in Figure 2-13, the torque variation is around 0.3 N.m between 2.54 m and 3.81 m, and less than 0.05 N.m between 3.81 and 5.08 m and between 5.08 m and 6.35 m. These results are still quite accurate as the flow is largely established before the turbine early in the simulation as compared to the flow behind the turbine where turbulent eddies must be resolved prior to accurate modeling. The results of the tests for upstream distance are shown in Figure 2-14.

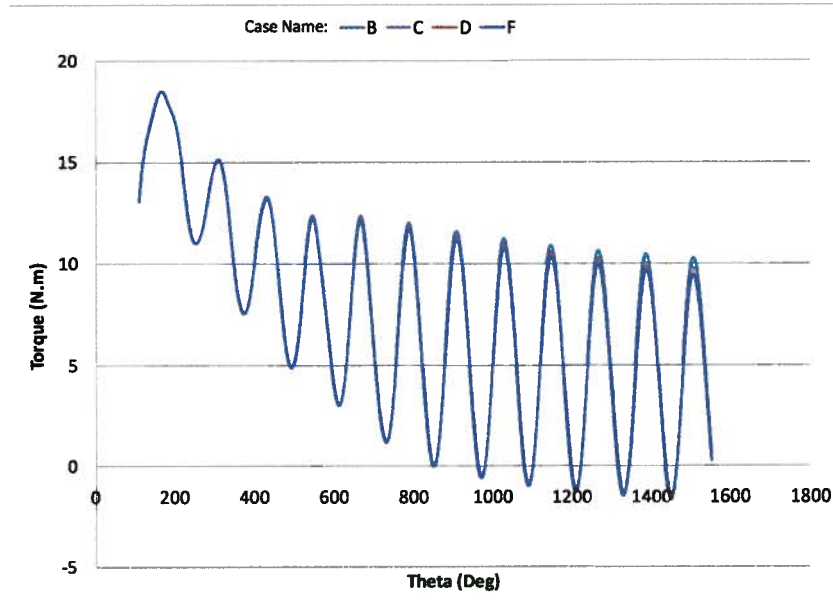


Figure 2-14: The upstream distance effect on the torque generated by the turbine

2.3.3 Downstream Distance

For an accurate depiction of vortex shedding phenomenon, a properly sized trailing distance is required to allow for the formation and dissipation of eddies shed from the blades and the shaft. The results suggest that a downstream spacing of around 10.16 m should suffice for adequate realization of the shed vortices. This size is approximately 10 times larger than the turbine diameter and is recommended in different sources such as [30].

2.4 Solver Specifications

In the following section the solver specification used for the simulations are described. As the working fluid in the simulations is water which is an incompressible fluid, a segregated solver can be applied. A 2nd order, implicit, and unsteady solver was used to increase the accuracy of the solution. The advantage of using an implicit solver is accelerated convergence and also the solution is stable regardless of the time step value. On the other hand, an implicit solver requires more memory and is recommended when sufficient amount of memory is available.

The flow was also a turbulent flow and the one-equation Spalart-Allmaras turbulence model was used to model the turbulence in the flow. The details of the procedure of selecting a proper turbulence model are extensively described in the turbulence modeling section.

The under relaxation factors for the flow parameters were set as presented in Table 2-6. These parameters can be manipulated during the solution to control the convergence and convergence speed of the solution. In the current simulations, the only parameters which were changed during the solution process were pressure and momentum, changing gradually to the values of 0.7 and 0.3 respectively to accelerate the convergence.

Table 2-6: Under Relaxation Factors used for the simulations

Parameter	Under Relaxation Factor
Pressure	0.3
Momentum	0.7
Density	1
Body Forces	1
Modified Turbulent Viscosity	0.8
Turbulent Viscosity	0.8

PISO algorithm was also used for the pressure-velocity coupling. PISO which stands for Pressure Implicit with Splitting Operators, uses one predictor step and two corrector steps and can be considered as an extension to the SIMPLE (Semi-Implicit Method for Pressure-Linked Equations) algorithm with one more corrector step to improve it. The details of this method can be found in many CFD books [38]. Although PISO algorithm increases the computations, it shows an accelerated convergence compared to SIMPLE, SIMPLEC, and SIMPLER algorithm in unsteady problems. An under relaxation factor is involved in this method to stabilize the calculation process.

The convergence criteria used for the continuity, momentum and turbulence equations were set to at least 10^{-5} . It was, however, observed that while continuity converges at a lower rate, momentum and turbulence equations were converged to a value of 10^{-7} or lower in most cases.

Selection of the time step is one of the important parts of the simulations. Choosing an improperly large time step does not only affect the convergence of the solution, but also results in significant errors in the results of the simulations. On the other hand, choosing an extremely small time step can significantly increase the simulation time. Thus, setting an optimum time step for the simulations is required to obtain accurate and quick results. The strategy used for the simulations was to start with a relatively large time step and allowing the turbine to go through a few cycles. After the solution was

periodically repeated, the time step should be decreased to a value at which the maximum cell courant number in the important regions of the flow field such as the blades surfaces and wakes are lower than 20-40. Therefore, the contours of courant number were monitored in several steps during the solution to ensure that the maximum courant number does not exceed the limits. This value for the courant number usually results in proper convergence in 10-20 iterations per time step. It should be noted that any increase or decrease in the time step should be done gradually to prevent numerical instabilities. In order to make sure that the time step is sufficiently small, the time step was reduced during a typical simulation and the changes in the torque curve were monitored. The time step at which the difference between the average torque values was less than 1% was chosen as the time step for all the simulations.

There are two options available to simulate an unsteady moving mesh problem: sliding mesh scheme and dynamic mesh scheme. Dynamic mesh scheme basically changes the cells shape as the object moves in the medium, and after a few time steps the grid for a part of or for the whole domain needs to be regenerated to prevent the cells to be highly skewed. The disadvantages corresponding to this method are increased computational time and cost due to the necessity of grid generation at every few time steps. Moreover, the stability, convergence speed, and accuracy will be decreased because of the existence of low quality highly skewed cells in the domain especially in the regions around the blades where the flow needs to be predicted accurately.

Conversely, in the 2D sliding mesh scheme, two surfaces with a relative motion to each other slide on an interface edge and form a conformal grid at the interface. In spite of the dynamic mesh schemes, the grid is not regenerated or dragged during the solution and hence, there is not any chance of formation of highly skewed cells in this scheme. Therefore, a more accurate and accelerated solution can be obtained by applying this method to the current simulations. The application of sliding mesh scheme for the current turbine modeling is depicted in Figure 2-15.

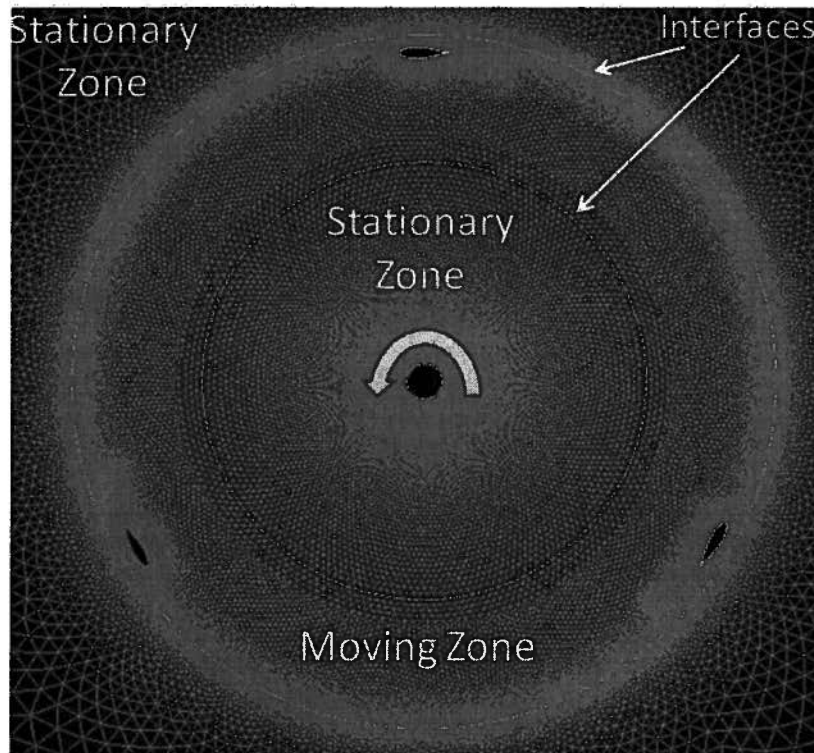


Figure 2-15: Sliding mesh scheme used for modeling the moving mesh

As it is shown in this figure, the domain is split into three different zones; two stationary zones inside and outside of the blades rotation area and a moving part in the middle which rotates around the center of the shaft. As the blades are placed in this zone, the angular velocity of the moving mesh zone should be the same as the turbine's RPM. The shaft in the center is also defined as a moving wall with the same angular velocity as the blades and the moving mesh zone.

The stationary zones and the moving mesh zone are separated by two interface edges as indicated in Figure 2-15.

The methodology that the sliding mesh scheme uses is based on the fact that at the intersection of the interface zones at each time step the fluxes across the sliding interfaces can be calculated by ignoring the interface zone faces and using the faces created by the intersection of interfaces instead. In other words, instead of calculating the flux from face AB, the interface area is split into two faces, AC and CB and the flux across the AB face can be calculated by adding the flux from the AC and CB faces as shown in Figure 2-16.

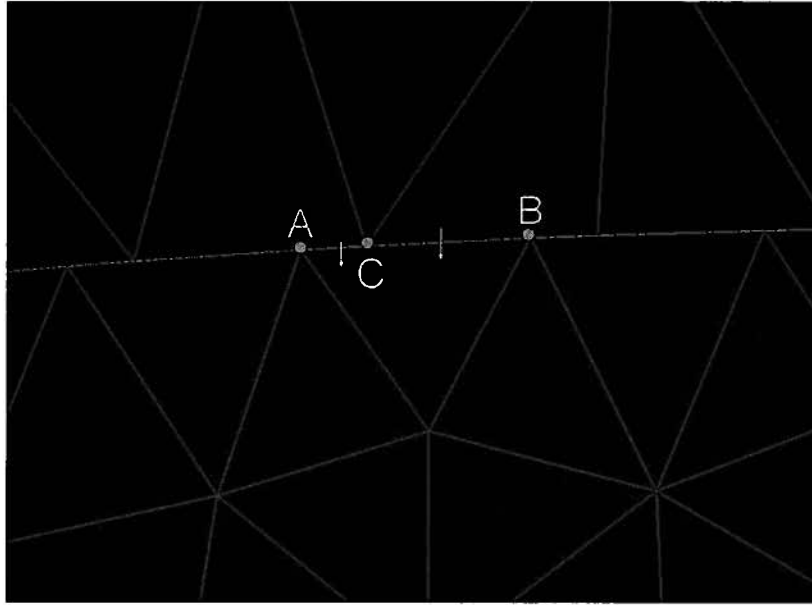


Figure 2-16: Sliding mesh scheme concept

It might be asked that it was possible to use an external stationary zone and an internal moving mesh zone in which the blades and shaft can rotate about the center of the shaft. There are two reasons that three zones were used instead of two because firstly, the three zone grid can allow for placing different designs such using an airfoil as the shaft cover or a few number of guide vanes as flow straighteners inside the turbine area to minimize the upstream blades' wake and shaft's wake effect on the rear part of the turbine. Secondly, a finer grid could be used in the middle ring in which the wake of the blades are dominant and a fine grid is needed to resolve the flow field accurately. In other words, having a middle region can help to control the grid distribution inside the turbine area while saving computational time and cost.

2.5 Turbulence Modeling

Turbulence modeling is one the three main fields in computational fluid dynamics along with solver development and mesh generation. In the recent years, with improvements in computational tools different approaches to the turbulence problem were introduced and developed. There are three different categories in numerical modeling of turbulence as follows:

- DNS (Direct Numerical Simulation)
- LES (Large Eddy Simulation)
- RANS (Reynolds Averaged Navier-Stokes)

In order to understand the advantages and disadvantages of each approach, the turbulence mechanism should be clarified. Briefly, turbulence is an unsteady, irregular, three dimensional, highly non-linear and, anisotropic motion of the flow in which transported quantities such as mass, momentum, and scalar quantities fluctuate in time and space. Turbulence contains different scales of eddies. Large eddies are carried in the flow field by the free stream flow and smaller eddies are carried by larger eddies. Larger eddies have size and velocity in the order of the mean flow. Their energy is transferred to the smaller eddies through a mechanism which is called vortex stretching. This transfer of energy from larger eddies to smaller eddies is called Energy Cascade. When the energy is transferred to small eddies, it dissipates in the form of thermal energy via viscous dissipation. This phenomenon happens in the smallest scales which are referred to as the Kolmogorov scale. The rate at which viscous dissipation occurs is the same as the rate of energy transfer from larger eddies to smaller ones.

Different approaches to turbulence modeling in CFD are based on the structure of turbulence and size of eddies as shown in Figure 2-17.

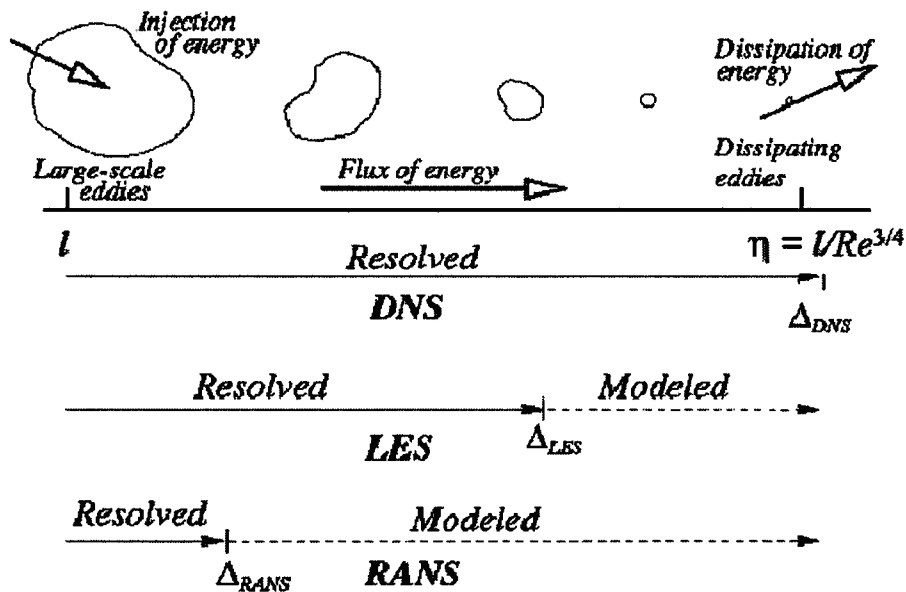


Figure 2-17: Approaches to turbulent modeling [37]

In DNS, full Navier-Stokes equations are solved for all scales of eddies and hence, there is no need to model the turbulence which results in increased accuracy and reliability. On the other hand, as this approach requires eddies to be solved to the Kolmogorov scale, it needs vast computational resources and is not practical for industrial CFD problems and is only applicable to research purposes with very low Reynolds numbers. Predictions show that with improvements in the computer technology, the flow around a full airplane can be solved using DNS not earlier than 2080.

The second approach to the turbulence modeling which was developed in recent years is Large Eddy Simulations. The method that LES uses is to resolve Navier-Stokes equations for large scale eddies and to model small scale eddies. The small scale eddies are in fact filtered in this method. It is computationally cheaper than DNS method but less accurate. Another disadvantage of LES is that it has to be done in 3D and is not suitable for engineering applications that can be conducted in 2D with significantly lower computational cost.

Another approach to solve the turbulence problem is the RANS method. RANS modeling introduces each quantity in the form of a mean value (which is obtained by ensemble averaging) plus a fluctuating term (Equation 2-9).

$$\phi = \bar{\phi} + \phi' \quad \text{Equation 2-9}$$

Writing the flow parameters such as pressure and velocities in this form and plugging them into the Navier-Stokes equations results in an equation identical to original Navier-Stokes equation with one additional term as in Equation 2-10.

$$\rho \left(\frac{\partial U_i}{\partial t} + U_k \frac{\partial U_i}{\partial x_k} \right) = -\frac{\partial p}{\partial x_i} + \frac{\partial}{\partial x_j} \left(\mu \frac{\partial U_i}{\partial x_j} - \rho \overline{u'_i u'_j} \right) \quad \text{Equation 2-10}$$

The new term appeared in Equation 2-10 is $-\rho \overline{u'_i u'_j}$ and is called the Reynolds stresses. This term is added to the strain term and has the form of viscosity. The task of a turbulence model is to calculate the Reynolds stresses and close the equation. Hence, the problem of obtaining turbulent shear stresses is sometimes called the closure problem. A simple approach to the closure problem was introduced by Joseph Valentin Boussinesq. The Boussinesq approximation is based on dimensional analysis and assumes that the turbulence is isotropic. This approach relates the turbulence stresses to the mean flow

by introducing a turbulent eddy viscosity term μ_t . This approach led to a new family of zero equations (algebraic models), one-equation and two-equation turbulence models called eddy viscosity models. Baldwin-Lomax, Baldwin-Bart, Spalart-Allmaras, k- ϵ (with several modifications), Menter's k- ω and k- ω SST are some examples of eddy viscosity model with different number of transport equations.

Another approach that does not use the Boussinesq assumptions is Reynolds Stress Transport Models. There is no isotropy assumption in RSM models and they contain more physics of the problem but they are more complicated than eddy viscosity models and are computationally expensive.

For the current research several turbulence models were studied and applied to simulate the turbulent flow inside and outside of the turbine area. The options available for a 2D simulation were as follows:

- Spalart-Allmaras (one-equation model)
- k- ϵ (two-equation model)
 - Standard k- ϵ
 - RNG k- ϵ
 - Realizable k- ϵ
- k- ω (two-equation model)
 - Standard k- ω
 - k- ω SST
- Reynolds Stress Model

After a detailed investigation for an appropriate turbulence model and running a few number of simulations to compare their performance (Figure 2-18), Spalart-Allmaras was chosen as the turbulence model for the simulations. The main advantages of this turbulence model are its low computational cost, stability and acceptable accuracy. This model was first developed for aerospace applications but is gaining popularity in the turbomachinery fields as well. However, like many other turbulence models, it is incapable of modeling severe separations perfectly.

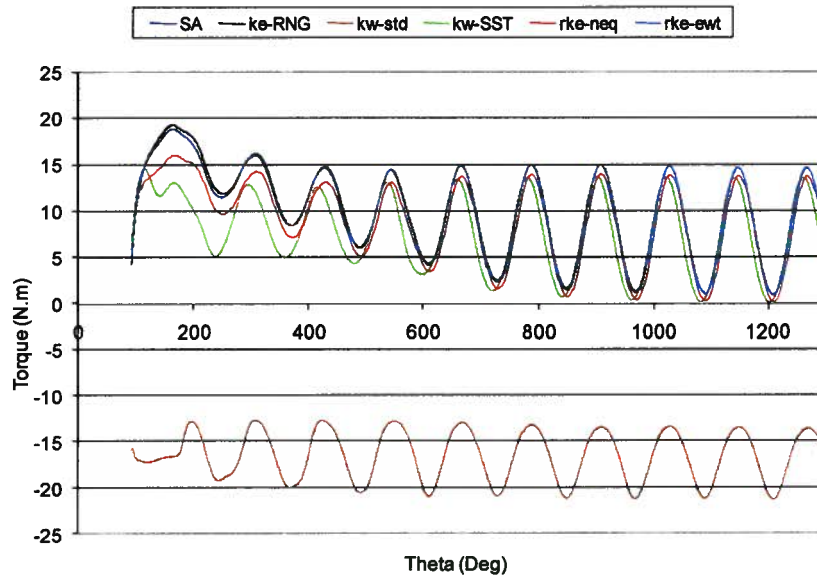


Figure 2-18: Comparison of the results obtained for different turbulence models

Another important characteristic of Spalart-Allmaras model is that it is not sensitive to the near wall modeling approach. In other words, it is modified in a way that if the y^+ value is in order of one, it resolves the boundary layer; otherwise, it uses the wall functions. Wall functions are empirical correlations to approximate the flow field in the viscous sublayer and buffer layer. In fact, they act as a bridge to relate the near wall flow field to the fully turbulent regions. For the wall functions to be engaged in the simulations, the y^+ value should be above 5. If the y^+ value is under 5, another approach for the near wall modeling will be engaged to resolve the boundary layer. The concepts of these two near wall modeling approaches are depicted in Figure 2-19. The second approach is noticeably more accurate than the wall functions but is computationally more expensive as 10 or more cells are needed in the viscous sublayer and buffer layer. In the current research, the second approach was taken since the boundary layer growth and separation would largely affect the turbine performance and needed to be accurately predicted.

One of the problems with all modification of $k-\epsilon$ and RSM models is that the near wall modeling approach has to be specified for the simulations and is applied to all the walls. However, in the simulations conducted, especially for the ducted turbine models, the y^+ value can change between values lower than one and 6. Also, y^+ value on the blades changes as the turbine rotates. This is because that y^+ value is not only a function of the near wall grid but also a function of Reynolds numbers. Hence,

it is not possible to switch between different near wall modeling methods, the simulations, can be instable and inaccurate. Thus, a flexible approach is essential to adapt itself to the local Reynolds number and the near wall grid. Another problem with these models, especially with RSM is their stability problems and high computational cost as it is a five-equation model.

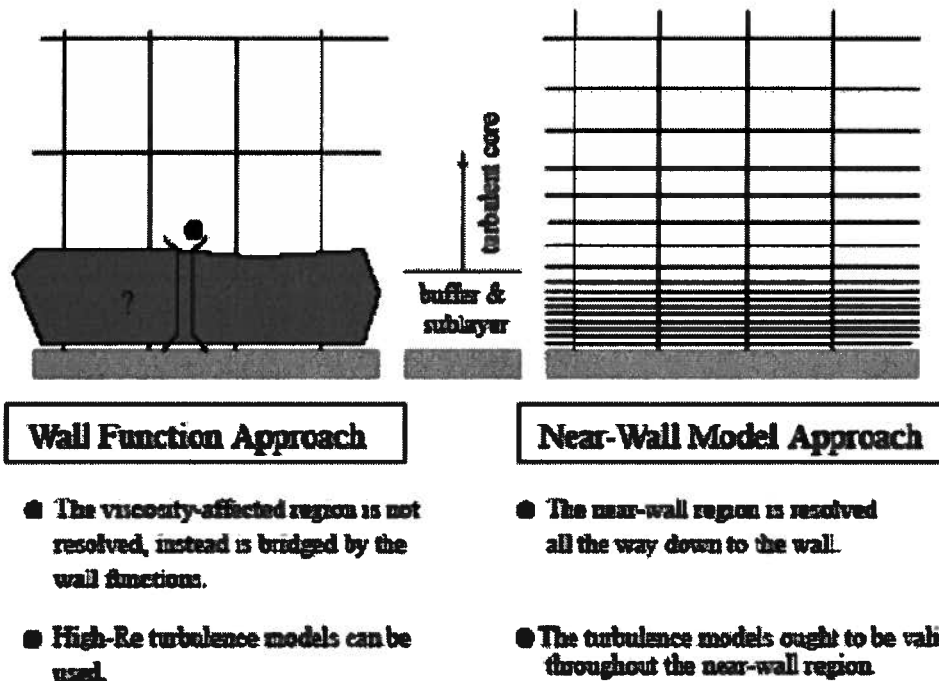


Figure 2-19: Comparison of two available approaches to the near wall modeling [37]

Also, standard $k-\omega$ and $k-\omega$ SST did not show a superior performance in this application. They also sometimes showed instability and convergence problems as well. Another problem these models share with $k-\epsilon$ and RSM models is their higher computational cost in comparison with Spalart-Allmaras turbulence model. In the next phase of the project in which 3D simulations will be conducted (based on the availability of computational resources) it is recommended to study LES and DES (Detached Eddy Simulation) models as some unsteady phenomena may not be modeled properly in RANS models especially at higher angles of attack where severe separations occur.

3. CFD Simulation of a Ducted Vertical Axis Tidal Turbine

The previous research [31-36] showed that confining the turbine within a parabolic duct can result in an increase in the power generated by the turbine. When using a venturi-shape duct, the flow accelerates inside the duct and the kinetic energy delivered to the blades is increased. However, placing a duct around the turbine can increase the complexity and cost of design and installation of the device. Thus, a detailed study of the mechanical design, mooring, maintenance, financial, and other aspects of the project must be undertaken before a decision is made regarding the use of a duct.

In this chapter, the simulation process of a ducted turbine will be described. After conducting simulations for a free-stream turbine and understanding the optimum method of setting the solution parameters, a pair of symmetrically placed parabolic shaped ducts were modeled around the turbine to simultaneously accelerate the flow and guide the flow in a proper direction. The same duct geometry was used in the experiments conducted at UBC tow tank. The duct shape and dimensions are shown in Figure 3-1.

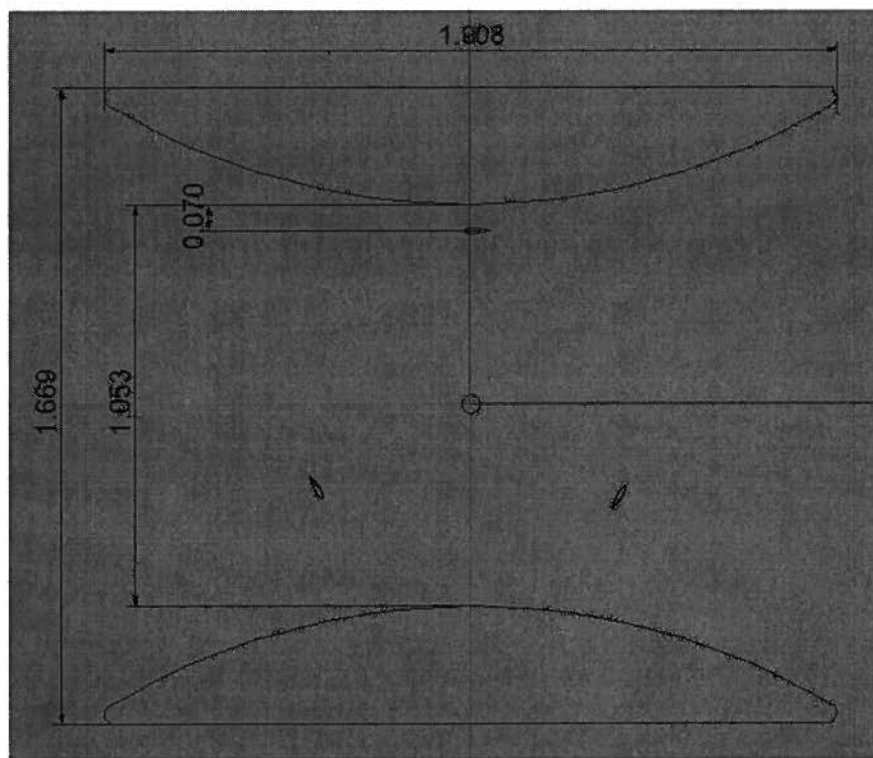


Figure 3-1: UBC duct dimensions (all dimensions are in metric)

The duct was positioned in such a way as to have a wall clearance of approximately one chord between the blade and the wall at the narrowest point. The rotor geometry was identical to the free-stream turbine. The same range of TSR's was used along with velocities of 1.5 and 2 m/s for the simulations. As it will be explained in Chapter 5, the experimental results obtained for the ducted turbine model at a speed of 2 m/s are of lesser quality due to significant free surface effects.

3.1 Grid Generation, Boundary Conditions and the Domain Size

As in the case of the grid generated for the free-stream turbine, a combination of structured and unstructured triangular elements was used to discretize the domain for a ducted turbine. The same type of 80-layer, C-Shape structured mesh was used around the blades with 240 nodes on the surface and 120 on the wake. Also, a structured grid around the shaft with 60 nodes on the shaft surface and 50 layers of cells with a growth ratio of 1.1 was used to model the shaft. The remainder of the domain was modelled using triangular cells. The only difference between the free-stream turbine mesh and that of the ducted turbine was that the outer interface that defines the moving wall boundary was placed closer to the blades to allow the walls to be only a chord away from the blades (Figure 2-3 and Figure 3-2). Moreover, a structured quadrilateral grid was used to mesh the ducts (Figure 3-3). The first cell height, the growth ratio, and number of layers were set to $1.27 \cdot 10^{-4}$ m, 1.15, and 20 respectively. This cell height yields a y^+ value about 30. This grid density is sufficient for the ducts as the flow separates mildly at the rear part of the duct compared to the sever separations on the blades. Also, the fine grid on the blades is used to properly solve for the drag force. Since an accurate drag force of the duct is not of interest at this stage, a coarse grid may be used to decrease the computational time and cost.

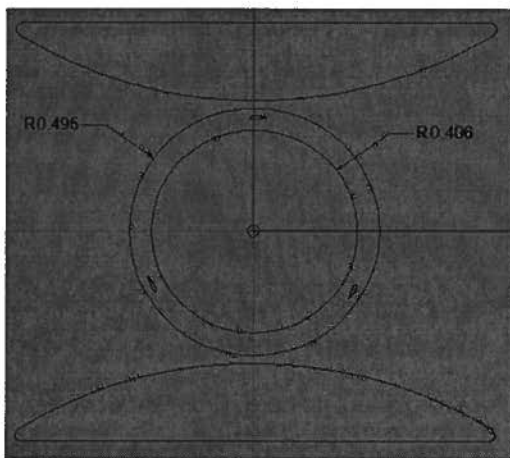


Figure 3-2: Interfaces in the ducted turbine configuration

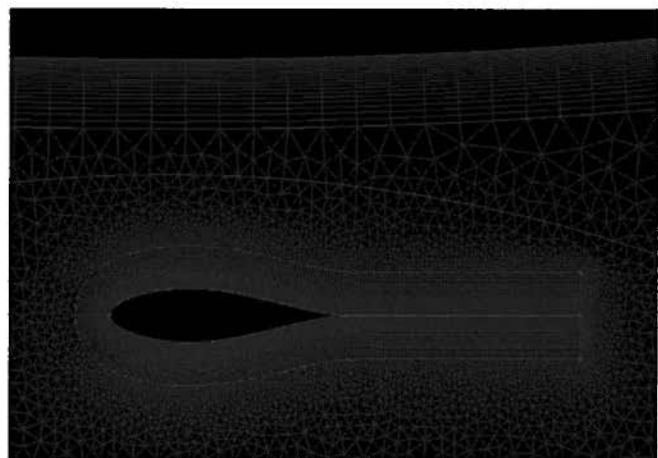


Figure 3-3: Duct and blade grid in ducted turbine configuration

To avoid large cell size gradients in the limited space between the blades and the interfaces, the number of nodes on each interface needed to be increased. This leads to an increased number of cells in the ducted turbine model in comparison to the free-stream model. The total number of nodes used for the simulations is approximately 235,000 cells.

As in the case of the free-stream simulation, grid refinement study was conducted to ensure a grid independent simulation. Three different mesh densities were used to study the grid convergence as presented in Table 3-1. The TSR used for the grid convergence study was 2.75 which was the same as that used for grid refinement study of the free-stream turbine.

Table 3-1: Grid Refinement Study for a Ducted Turbine

Grid	Number of Cells	Average Power Per Cycle (Watts)
Coarse	159,094	911.4
Medium	235,170	587.1
Fine	358,223	586.4

The torque curve per cycle was also plotted for each mesh density to ensure the convergence of the results as shown in Figure 3-4. It should be noted that the grid adjacent to the wall was not made coarser and was kept constant for all three grids. The reason for that was to keep a consistent method of solving the boundary layer in coarse, medium and fine grids. Had the near wall mesh been made coarser, the y^+ value would have exceeded 30 and hence a wall function would have to be used to calculate the boundary layer which is different than the near wall approach used for fine and medium grid densities described in the previous chapter.

In addition, as the grid becomes finer, a smaller time step is required to keep the cell Courant Number in the same order for different mesh densities. In order to accelerate the solution process, a relatively larger time step may be used at the beginning of the simulations which can be decreased gradually to solve for a few more cycles to obtain the final results. The final time step used for the simulations in this study was set to 0.2 milliseconds.

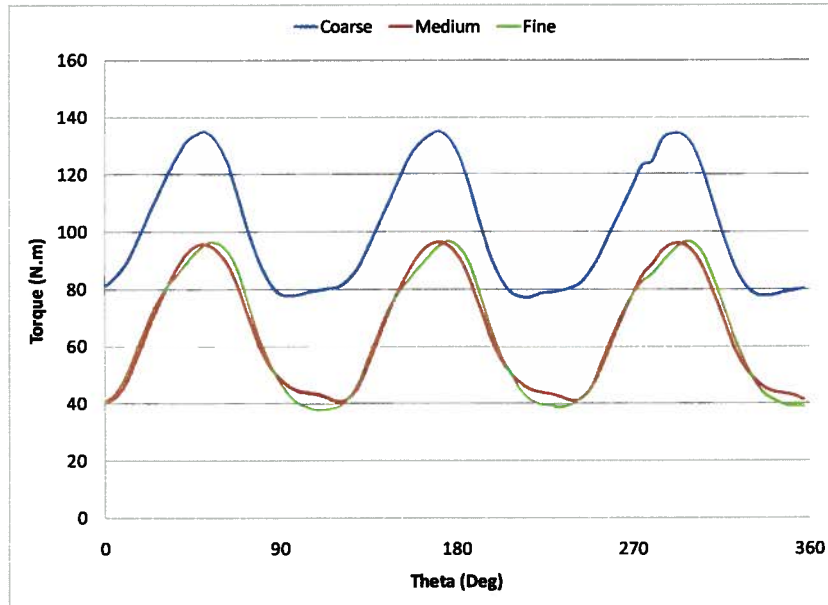


Figure 3-4: Grid convergence results for a ducted turbine at TSR=2.75

The same domain size as the free-stream turbine was used for the simulations of the ducted turbine to keep a constant blockage ratio with the tow tank experiments. The blockage ratio for the ducted case is less than 13% and the results can still be considered as free stream conditions. Alternatively, [39] recommends an analytical approach based on the actuator disc theory to estimate the effect of the domain walls effect on the solution. Those recommendations can also be used to verify if the domain walls have negligible effect on the results. Moreover, the free vortex code developed in UBC's Naval Architecture Lab can be used to estimate the effect of the domain size on the simulation results as well [40].

3.2 Solver Specifications

Similar to the free-stream turbine model, a 2D, second order, implicit, segregated solver was used for the ducted turbine modeling. A PISO algorithm was also used for pressure-velocity coupling in conjunction with the Spalart-Almaras turbulence model. As the grid is finer in the ducted turbine model compared to the free-stream turbine model, a smaller time step should be used for the solutions. The same strategy for under relaxation factors were used for the ducted simulations as well. It was also noticed that increasing the pressure under relaxation factor beyond this threshold leads to the divergence of the solution. An upwind first order discretization scheme was used for momentum, pressure and turbulence equations at the beginning of the simulations because of the acceptable

accuracy and proper convergence behaviour. After the turbine reached quasi steady state conditions, a second order upwind scheme was used to increase the accuracy and reliability of the solutions. At that point the convergence criteria for residuals were decreased to 10^{-5} for all the equations. The momentum in X and Y direction as well as the turbulence equation converged beyond 10^{-8} . The continuity equation, however, converged at a slower rate and did not reach a residual value lower than 10^{-7} with a reasonable number of time steps. Better convergence can be achieved for the continuity equation by significantly decreasing the time step size, but this will increase the computational cost and is not practical for engineering applications. The forces on the blades were monitored during each iteration to ensure that the solution was converged properly.

Akin to the free-stream turbine model, a sliding mesh scheme was used to simulate the blades rotation around the turbine's shaft center. The shaft rotation was set at the same angular velocity as the blades and the moving mesh zone.

3.3 Turbulence Modeling

The same turbulence model (Spalart-Allmaras) was also applied to the simulations of a ducted turbine because of its accuracy, reasonable computational cost and reliability. The significance of using this turbulence model was more pronounced in this set of simulations because of the different mesh densities around the blades and the ducts. In other words, as the drag of the ducts is not of particular interest at this point, a coarser grid may be used adjacent to the ducts to decrease the computational time and cost. A coarser grid around the ducts needs the wall function approach to be engaged to calculate the boundary layer. Hence, a flexible turbulence model is required to apply two different near wall approaches simultaneously to solve the boundary layer accurately on the blades and use a wall function to calculate the boundary layer characteristics around the ducts. As it was described in the previous chapter, the modified Spalart-Allmaras turbulence model can handle this situation. On the contrary, k- ϵ and RSM model need a single near wall modeling approach to be selected and cannot apply to the above mentioned approaches at the same time. It was observed that using either a wall function or enhanced wall treatment approaches with these turbulence models will lead to numerical instability and divergence in some cases. Strictly speaking, any turbulence model needs certain modifications depending on the application to increase the accuracy. However, modification and development of turbulence models are beyond the scope of the current research and the reader should be aware of the fact that turbulence models imperfections are among the sources of error in the simulations, especially in the cases with larger adverse pressure gradients and severe separations.

4. Experimental Design and Analysis of BERT Turbine

The following chapter is selectively quoted from an internal lab report on the experimental research conducted in August 2006 and November 2006 by the Naval Architecture Lab at UBC. Another set of experiments was also conducted by the Naval Lab in September 2007. Parts of the results obtained from those tests are used in Chapter 6 for validation of CFD results.

In order to validate the numerical models and obtain a better understanding of the performance, a vertical axis tidal current turbine model was designed and built in the UBC naval lab and subsequently tested in the UBC tow tank. This turbine is a scaled version of the Blue Energy vertical axis turbine. The first set of tests took place between Aug 17, 2006 and Aug 24, 2006 on the original un-ducted version of the turbine. A second set of tests was performed between the 13th and 26th of November, 2006 on a ducted version of the turbine.

4.1 Experimental Model

As shown in Figure 4-1, the experimental model was a 0.91m diameter 3-bladed vertical axis turbine. The foil section used for the blades was a NACA 63₄-021 section. The NACA section was selected in previous NRC studies. The blades were mounted to the central shaft via two arms connected at the quarter-span locations. Arms were fixed to the blades using a pivot joint with a clamping mechanism such that the angle of attack could be adjusted using precision-wedges.

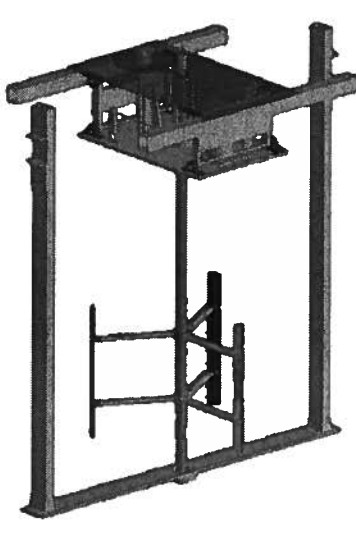


Figure 4-1: Experimental model of the turbine tested at UBC tow tank

As shown in Figure 4-2, the upper shaft bearing was mounted out of the water onto a force balance consisting of a two parallel plates capable of translating relative to each other and connected via load cells. The load cells were used to measure the drag force exerted on the turbine as it was towed through the water. The turbine revolution speed was regulated using an AC motor controller. An optical encoder was used to measure rotational speed and angular position of the main shaft. A torque meter was connected inline to measure the torque produced by the turbine. In addition pressure taps were placed along the length of the duct to aid with validation of the numerical modeling.

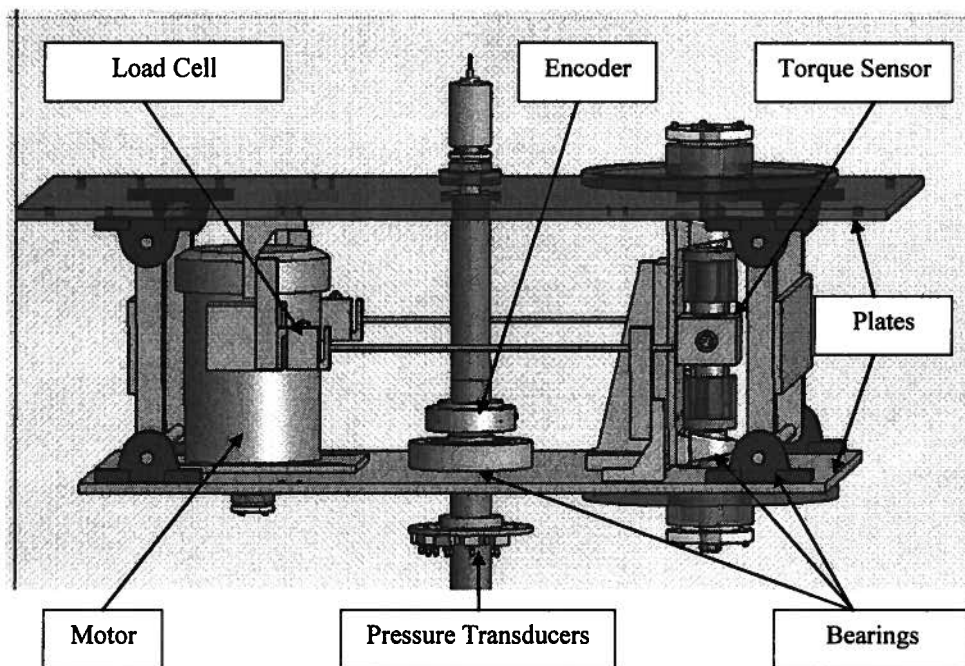


Figure 4-2: Force balance assembly and data acquisition devices

Also, an auxiliary carriage was built with the purpose of providing a stable platform spanning the width of the tank to allow for installation and testing of ocean engineering devices. This carriage was designed in the Naval Architecture lab and built at the UBC Mechanical Engineering machine shop. The auxiliary carriage bolts directly to the main carriage by which it is driven as shown in Figure 4-3.

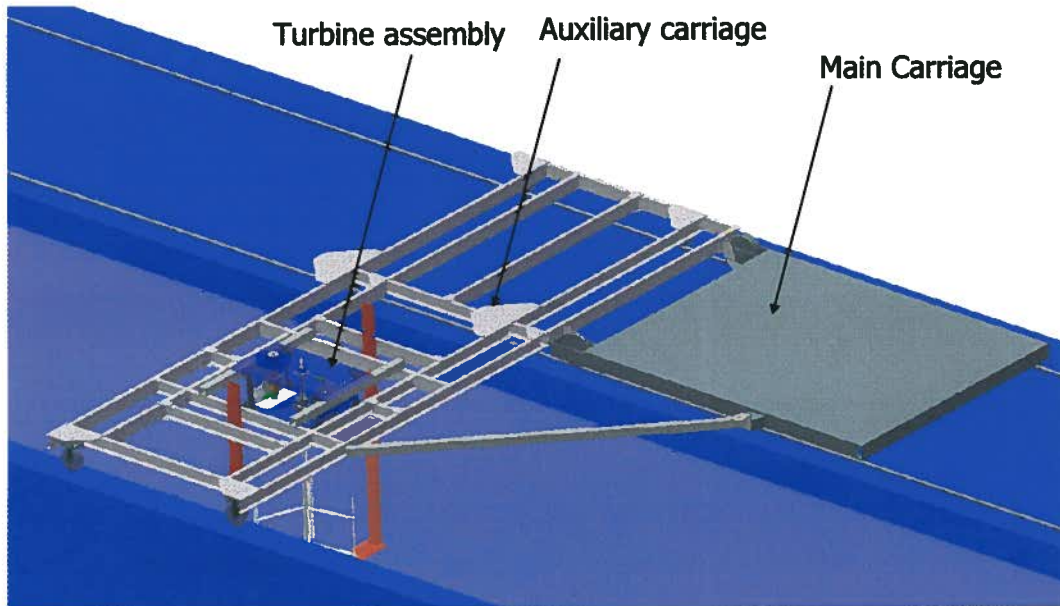


Figure 4-3: Testing carriage setup

A generic fiberglass Venturi type duct was mounted to the carriage and the surrounding frame positioning the lower shaft bearing. The ducting was 6 feet long by 1 foot maximum width, and was placed a chord length from the turbine blade at its closest central point. The turbine and duct setup are shown in Figure 4-4.

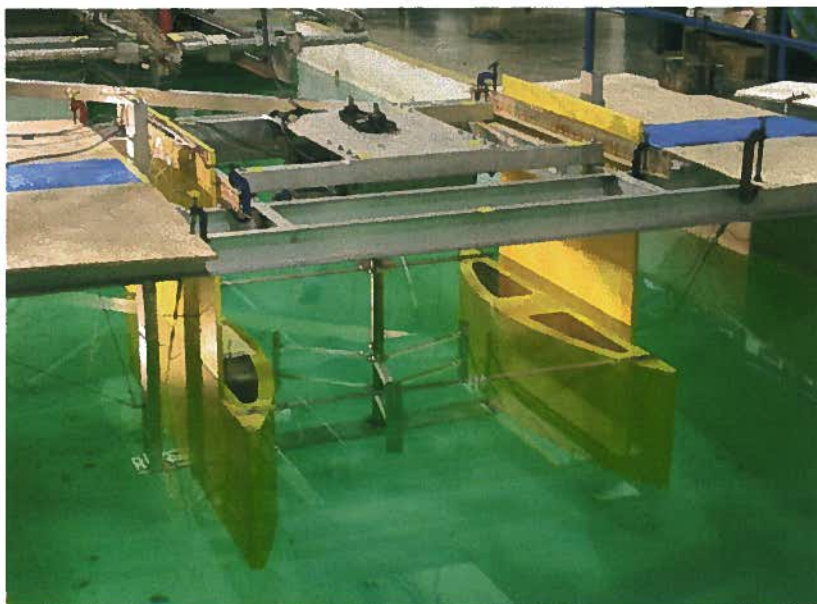


Figure 4-4: Experimental model of a ducted turbine

4.2 Testing Procedure and Methodology

The purpose of this testing was to test a scale model of the Blue Energy vertical axis turbine. The testing in the towing tank consisted of pulling the turbine through the water at a set carriage speed and turbine RPM to measure drag, moment, torque and pressures along the blades. The testing was repeated for a range of carriage velocities and RPM's. In addition, runaway RPM was also recorded for each carriage speed. The tests were first done for a blade angle of attack of zero, and subsequently repeated for angles of attack ranging between -10 and +10 degrees.

Live data analysis was done following each run to record the average achieved turbine torque which was plotted versus tip speed ratio (TSR). This method was used to guide the test program and avoid unnecessary runs, namely combination of carriage speed and RPM where the turbine did not produce torque.

A final round of testing was conducted with the turbine blades removed in order to provide an approximation of parasitic drag, namely, the added drag produced by the turbine shaft as well as the arms connecting the turbine blades to the central shaft.

In the second set of tests conducted November 2006 at UBC tow tank, a number of changes were made to the August model, such as minimizing the profile of the arms and replacing the rapid prototype section of the blade (used for measuring pressure) with a solid aluminum blade. The initial phase of testing in November repeated a similar testing matrix to that of August in order to establish a new baseline for the un-ducted turbine. Subsequent testing consisted of measuring the performance of a single bladed un-ducted turbine by removing two of the three blades. This was done to isolate the torque fluctuations over a revolution to a single blade as well as attempt to quantify the shadowing effect produced by the presence of blades and the shaft upstream. Following these tests, a ducted version of the turbine was tested using the same testing matrix as the un-ducted model. A final set of tests were conducted for a bi-foil configuration of the turbine in both the ducted and un-ducted configuration.

Figure 4-5 shows the torque profile of a typical run versus the angle of rotation showing the acceleration of the carriage, the working range of data acquired while the carriage is at constant speed, and the deceleration of the carriage. A MATLAB code was written to automatically select the acceptable range of data at which the carriage velocity is constant and the torque curve is repeated as shown in Figure 4-6.

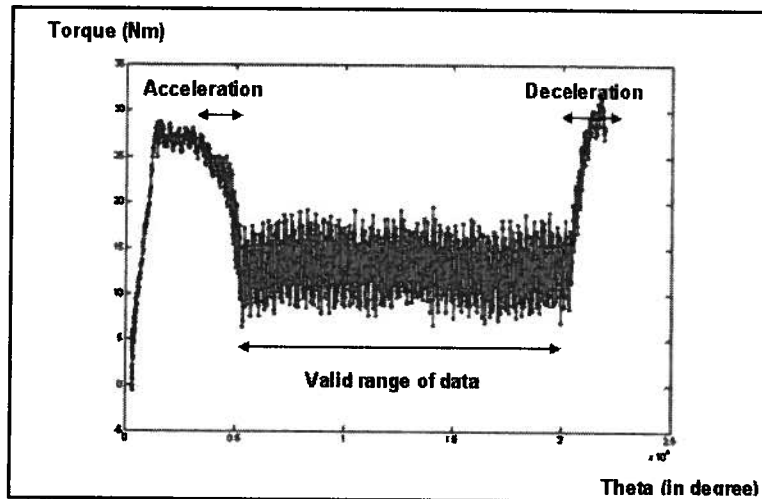


Figure 4-5: Torque curve versus the azimuth angle for a typical run

To obtain a smooth torque curve vs. the azimuth angle, a special averaging technique was implemented. The methodology used for this task was to isolate the data into small slices (every 2 degrees) and take the average of the data points in that range as shown in Figure 4-6. The torque curve was then plotted over 360 degrees of rotation cycle (Figure 4-7).

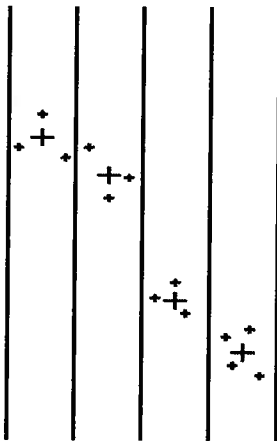


Figure 4-6: Averaging technique

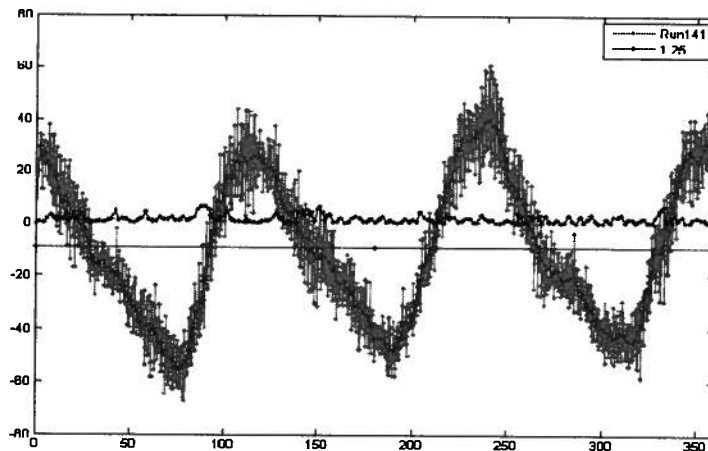


Figure 4-7: Averaged torque curve over a 360 degrees cycle

The torque curves obtained from runs at different velocities and TSR's were used to compare with the CFD model and the free vortex model to validate the numerical models. The experimental results obtained for a free-stream and a ducted turbine will be compared with CFD model results in Chapter 7. The numerical and experimental errors will also be discussed in details as the main sources of discrepancies between the results.

5. Numerical Results and Post Processing Procedure

This chapter includes the numerical results obtained from the simulations for both a free-stream and a ducted turbine. The results presented include the torque curves for different current velocities and tip speed ratios. Also, the non-dimensional power curves representing the turbine efficiency are given for different configurations. Comparison of these curves can be used to understand the effect of the ducting on the turbine performance. Moreover, the torque curve for a single blade in a 3-blade configuration is presented to facilitate the understanding of the locations of peaks and troughs of generated torque over a cycle. In other words, these curves explain why the generated torque is low in some regions over a cycle and how to address a low-torque problem.

In order to obtain the torque curve for each configuration, a User Defined Function (UDF) was written and linked to the software. A UDF consists of a C++ code linked to the main solution platform to conduct further detailed calculations which are not included or user-customizable within the software. The code for ducted turbine geometry is identical to the code used for free-stream turbine. The main task of the code is to integrate the pressure and shear stress distribution around the airfoil surface area (Equation 5-1). There are two types of forces exerted on the blades: pressure forces and viscous forces. The code goes through each element on the surface of the blades and calculates the pressure and viscous forces in X and Y directions knowing the normal vector components to the airfoil surface.

$$\vec{F} = \oint_s p \vec{d}_A + \oint_s \tau \vec{d}_A \quad \text{Equation 5-1}$$

Knowing the forces exerted on the blade in X and Y directions, the magnitude of torque about the shaft center can be easily calculated using Equation 5-2.

$$\vec{T} = \vec{r} \times \vec{F} = (r_x i + r_y j) \times (F_x i + F_y j) \quad \text{Equation 5-2}$$

In Equation 5-2, r_x and r_y are the horizontal and vertical distance of the quarter chord of the blade from the center of the rotation. The quarter chord of the blade is the location of arm attachment to the blades in the experimental. Connecting the arms to the quarter chord of the blades is also structurally beneficial as the center of pressure is approximately around that point and the moments exerted to the arm-blade joint are minimal.

At the beginning of the simulation, the torque curve shows variation over each cycle. This is because the wake is not well developed. It takes about 5 to 10 seconds of simulations (depending on the inlet velocity and TSR) for the wake to develop (Figure 5-1). At this point, the torque curve starts to repeat over each cycle and the flow field reaches quasi steady state conditions (Figure 5-2).

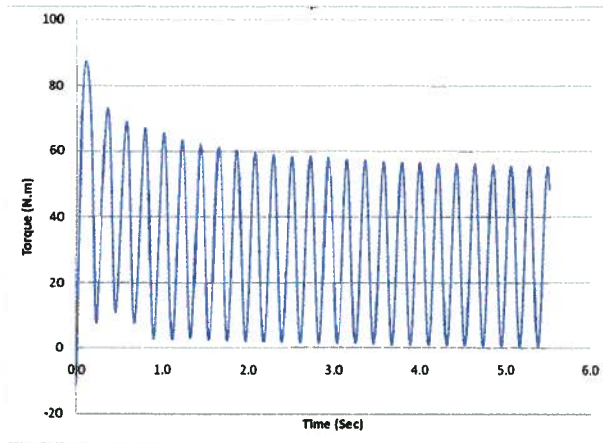


Figure 5-1: Wake development as the turbine rotates

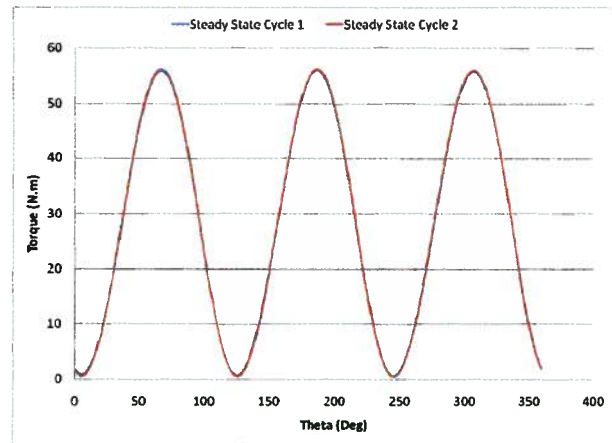


Figure 5-2: Repeating torque curves at steady conditions

After reaching the quasi-steady state condition, the average torque and the power generated over each cycle can be calculated. If the torque is recorded N times in a cycle of rotation, the average torque is calculated as Equation 5-3.

$$T_{avg} = \frac{1}{N} \sum_{i=1}^N T_i \tag{Equation 5-3}$$

The power generated by the turbine blades over a cycle can then be calculated using Equation 5-4.

$$P = T_{avg} \cdot \omega \tag{Equation 5-4}$$

There are two ways to define the efficiency of the turbine knowing the power generated per cycle. The first way is to calculate the ratio of the power generated by the turbine to the available kinetic energy in the current flowing towards the frontal area of the turbine. This kinetic energy available to the frontal area of turbine can be simply obtained using Equation 5-5.

$$P_{av} = \frac{1}{2} \rho A_{tfa} V^3 \quad \text{Equation 5-5}$$

Hence, the efficiency can be calculated as follows:

$$C_k = \frac{P}{P_{av}} = \frac{T_{avg} \cdot \omega}{\frac{1}{2} \rho A_f V^3} \quad \text{Equation 5-6}$$

The other way of expressing the efficiency is to define it as the ratio of generated power to the power that can be extracted theoretically from the turbine. This theoretical value is called Betz limit. The Betz limit shows theoretically that the maximum extractable power from a wind turbine or a tidal turbine is approximately 59% (16/27) of the kinetic power available based the frontal area of the turbine. Hence, the turbine efficiency based on Betz limit is defined as Equation 5-7.

$$C_p = \frac{P}{P_{max}} = \frac{T_{avg} \cdot \omega}{\left(\frac{16}{27}\right) \left(\frac{1}{2} \rho A_{tfa} V^3\right)} = \frac{C_k}{\left(\frac{16}{27}\right)} \quad \text{Equation 5-7}$$

As the Betz limit is only applicable to the free-stream conditions and is incapable of including more complications such as the ducted turbine, the efficiency used in the current research is based on the ratio of generated power to the available power (C_k). Hence, all the figures, tables and numbers presented for efficiency in this report use this definition for the turbine's efficiency.

In the design of tidal turbines, extracting the highest possible efficiency for a set configuration does not necessarily mean that the design is ideal. There are many parameters that need to be considered in the final design such as ease of structural design, cost, reliability, durability, etc. It is even hard to claim that the design is hydrodynamically optimal since a number of hydrodynamic phenomena were not considered in the current study. Additional topics such as cavitation need to be considered to obtain an optimum design; however, these topics are beyond the scope of this research.

5.1 Free-stream Turbine Results and Analyses

In the first set of simulations, the current velocity was assumed to be 1.0 m/s and tip speed ratio was ranging between 2.00 and 3.00 with 0.25 increments. The results presented are torque curve over a cycle for 3 blades and single blade in a 3-blade configuration as presented in Figure 5-3 through Figure 5-12. Figure 5-16 through Figure 5-25 show the torque curves for the same tip speed ratios with an incoming current velocity of 1.5 m/s. Finally, the torque curves are presented for an incoming velocity of 2.0 m/s.

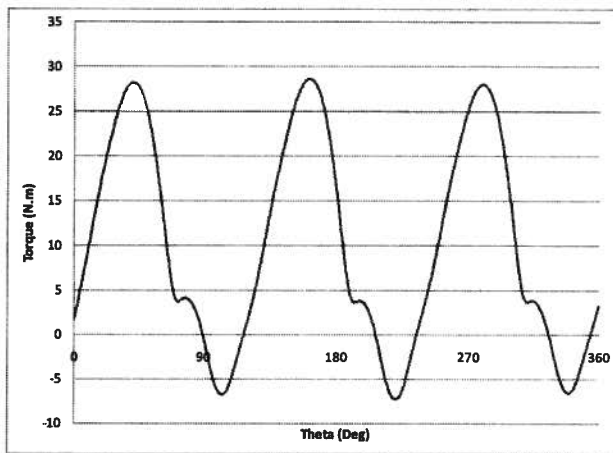


Figure 5-3: Torque curve (3 blades) ; V=1.0 m/s , TSR=2.00

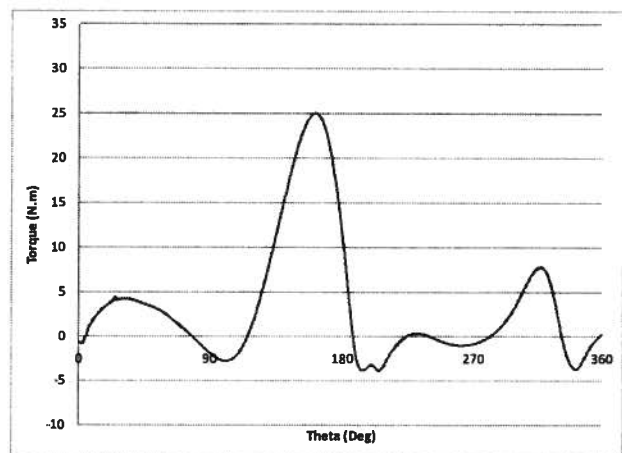


Figure 5-4: Torque curve (single blade) ; V=1.0 m/s , TSR=2.00

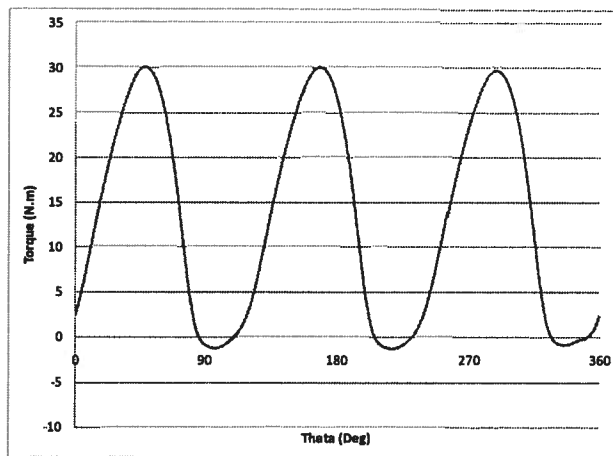


Figure 5-5: Torque curve (3 blades) ; V=1.0 m/s , TSR=2.25

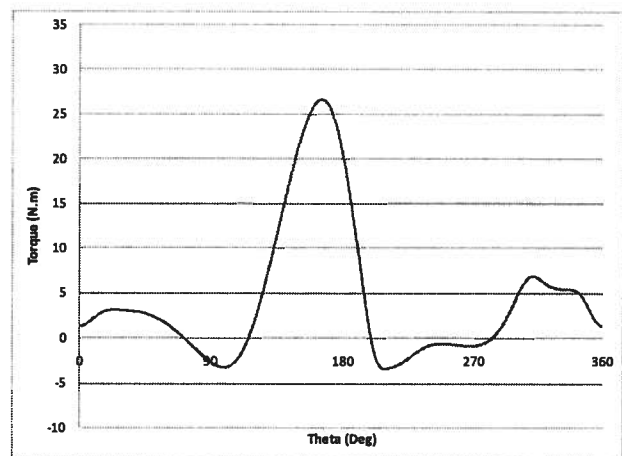


Figure 5-6: Torque curve (single blade) ; V=1.0 m/s , TSR=2.25

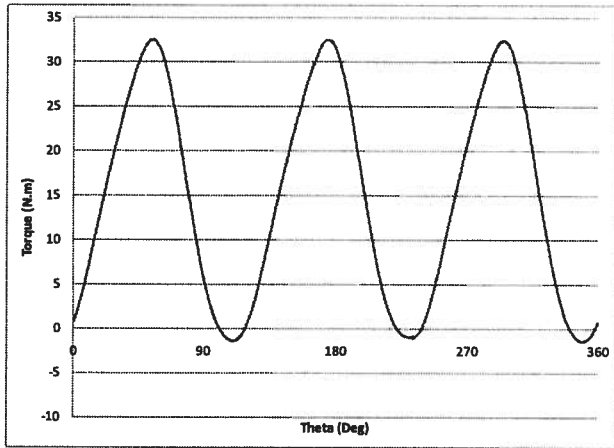


Figure 5-7: Torque curve (3 blades) ; $V=1.0$ m/s , $TSR=2.50$

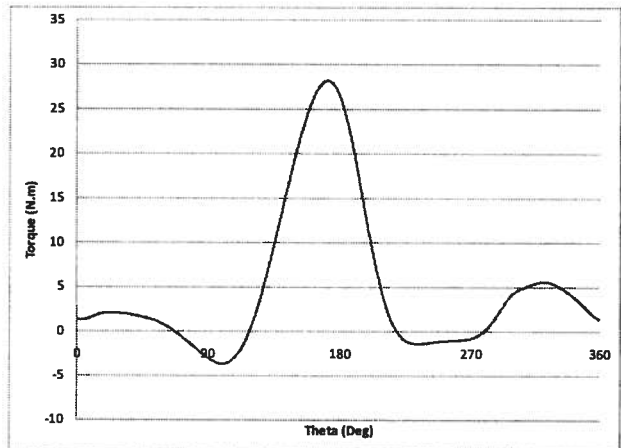


Figure 5-8: Torque curve (single blade) ; $V=1.0$ m/s , $TSR=2.50$

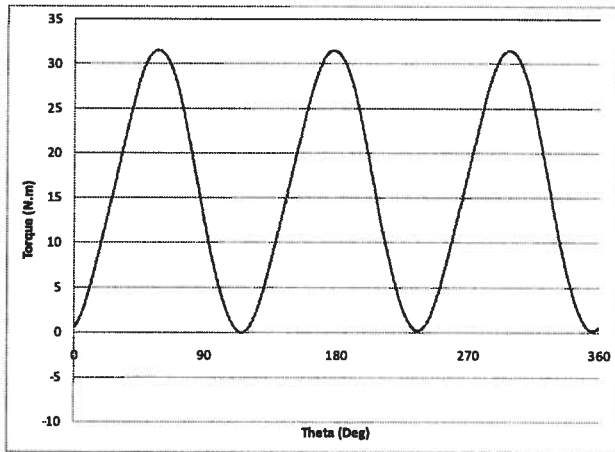


Figure 5-9: Torque curve (3 blades) ; $V=1.0$ m/s , $TSR=2.75$

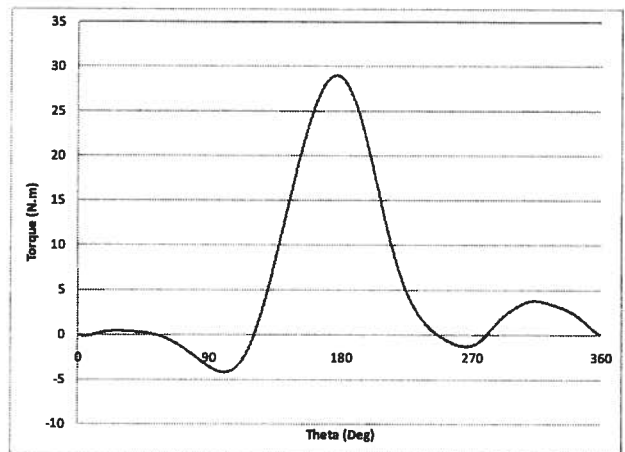


Figure 5-10: Torque curve (single blade) ; $V=1.0$ m/s , $TSR=2.75$

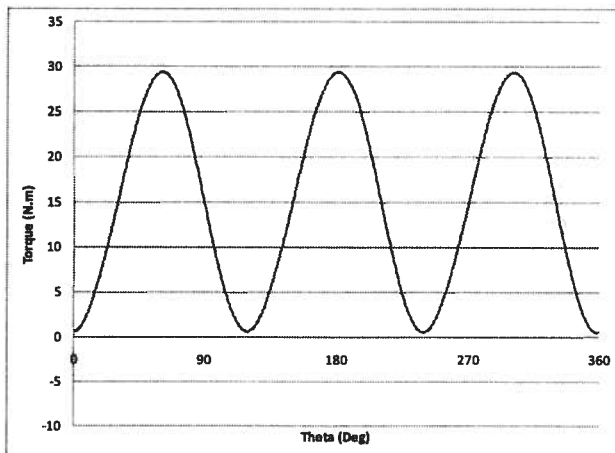


Figure 5-11: Torque curve (3 blades) ; $V=1.0$ m/s , $TSR=3.00$

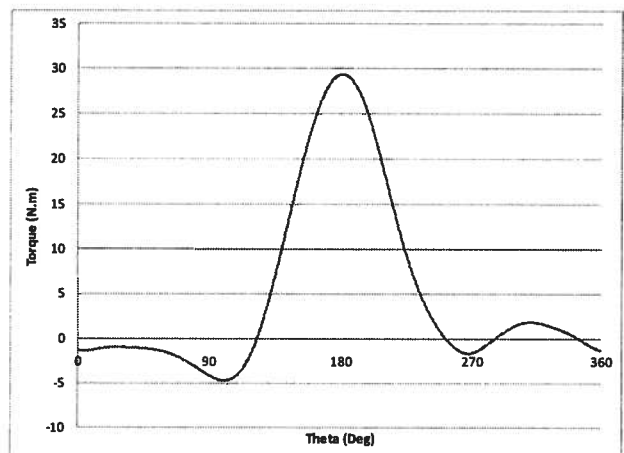


Figure 5-12: Torque curve (single blade) ; $V=1.0$ m/s , $TSR=3.00$

The results presented in Figure 5-3 through Figure 5-12 show the torque curve for 3 blades and 1 blade torque in a 3-blade configuration. It can be concluded from the 3 blades torque curves that:

- Torque magnitude increases with the increase in tip speed ratio up to $TSR=2.50$.
- Torque curve for 3 blades has a sinusoidal pattern with 3 peak points over a cycle.
- Torque fluctuations amplitude does not change significantly when TSR increases. However, the trough points appear to be shifted up as the TSR increases.
- A bump in the torque curve is observed at low TSR's ($TSR=2.00$) at about 80 degrees. However, this bump is diminished at higher TSR. This bump can be the result of super-imposing the torque curves of each individual blade. As the angle of attack seen by the blades is high at a phase angle of 80 degrees, a severe separation occurs over the inner side of the blade. This bump might be also due to the flow reattachment to the surface of the blades as well.
- At $TSR=2.75$ and $TSR=3.00$ a small torque drop is observed in the maximum torque magnitude. It is predicted that the torque magnitude continues to decrease significantly for TSR's higher than 3.00 as well.

The observations from torque curve for a single blade show that:

- There is one significant peak point in the torque curve ranging between 160 and 180 degrees of phase angle.
- The torque value at the peak point increases slightly as TSR increases.
- The phase angle where the torque reaches its maximum shifts to the right as TSR increases. This is because when TSR increases, the phase angle at which the blade stalls shifts to a higher azimuth angle.
- The important conclusion from the single blade torque curve is that the torque value is significantly reduced in the downstream section of the turbine (phase angles between 0 and 90 degrees and also phase angles between 270 and 360). This is due to the fact that at higher TSR's the intense vorticity shed from the upstream blades creates a wide region of disturbed, decelerated flow downstream that lowers the torque generated downstream of the turbine. In other words, when the blades rotate at a higher angular velocity, a virtual increase in solidity occurs that prevents the flow with high kinetic energy to be delivered to the downstream blades. This fact can be shown by comparing the velocity contours at a low and high TSR. Figure

5-13 and Figure 5-14 show the velocity contours at the TSR=2.00 and TSR=3.00 respectively. The black zones in these figures show the regions at which the velocity is lower than 0.7 m/s. It is seen that for TSR=2.00 the low velocity region is notably smaller than TSR=3.00. It is also observed that the vorticity shed from the shaft has a significant effect on the downstream flow. Hence, it seems that at lower TSR's the shaft contribution to downstream vortices is more significant than at higher TSR's where the vortices shed by downstream blade have dominant effects on the downstream disturbance.

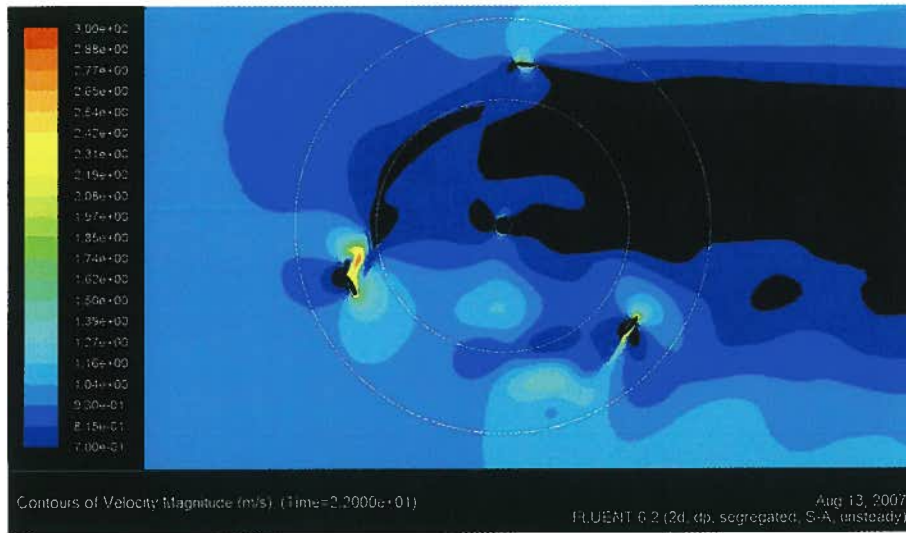


Figure 5-13: Velocity contours at V=1 m/s and TSR=2.00

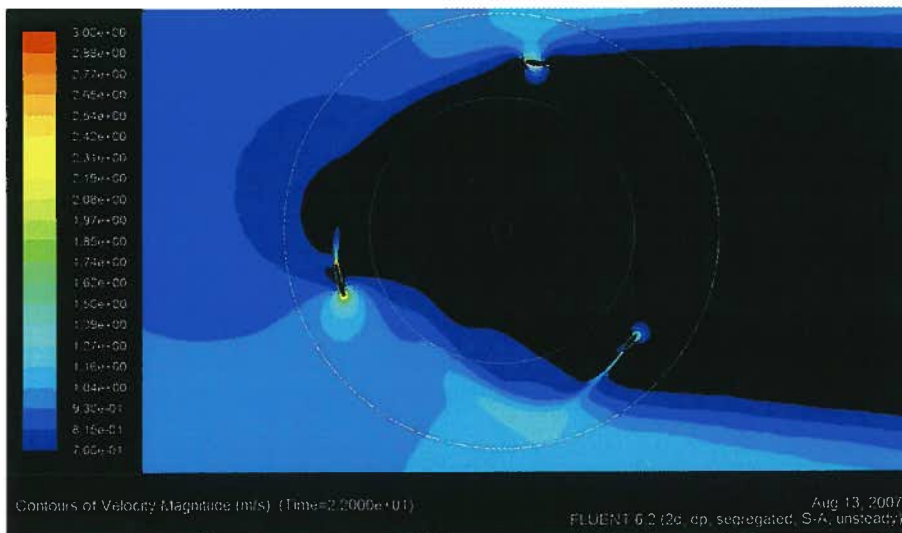


Figure 5-14: Velocity contours at V=1 m/s and TSR=3.00

After the torque curves were obtained, the average torque and consequently the power generated by the turbine and efficiency at each TSR was calculated. Figure 5-15 shows the efficiency curve for the first set of simulations at inlet velocity of 1.0 m/s and TSR's ranging between 2.00 and 3.00. It is seen that efficiency curve slope decreases as the TSR increases. In other words, the torque curve seems to follow a parabolic pattern from a relatively low value at TSR of 2.00 and peaks near a TSR value of 3.00. This behaviour is typical of such devices and has been documented in literature [31-36]. A decreased torque value at higher TSR's is due to low angles of attack seen by the blades. Hence, the drag force will be dominant while the lift force is small resulting in a negative torque magnitude according to Equation 2-3. It is observed that the efficiency does not exceed 32% at TSR=3.00. It should be mentioned that this efficiency is calculated based on the average of 2D torque. The 3D effects will be discussed in more details in Chapter 6 as well as other sources that cause a drop in efficiency.

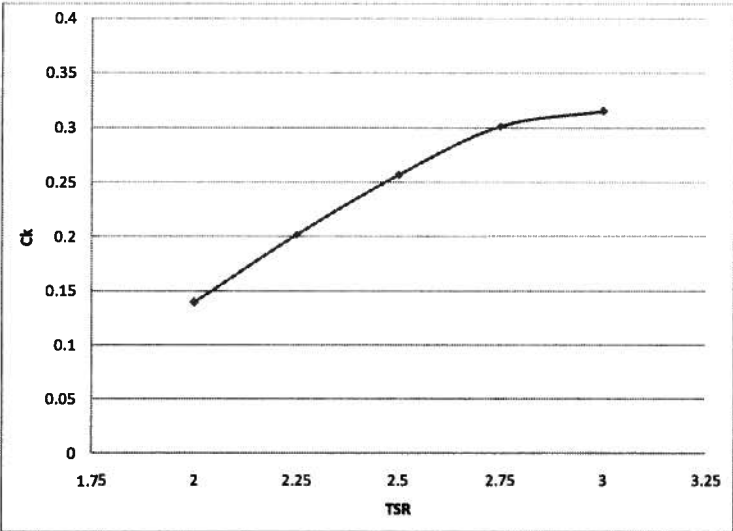


Figure 5-15: Efficiency curve for a free-stream turbine at V=1.0 m/s

Figure 5-16 to Figure 5-25 show the torque curves for the second set of simulations at an inlet velocity of 1.5 m/s. Similar to the simulations for an inlet velocity of 1.0 m/s, the TSR ranges between 2.00 and 3.00 with 0.25 increments. Knowing the torque curves, the average torque and power can be calculated and the efficiency can be obtained as presented in Figure 5-26.

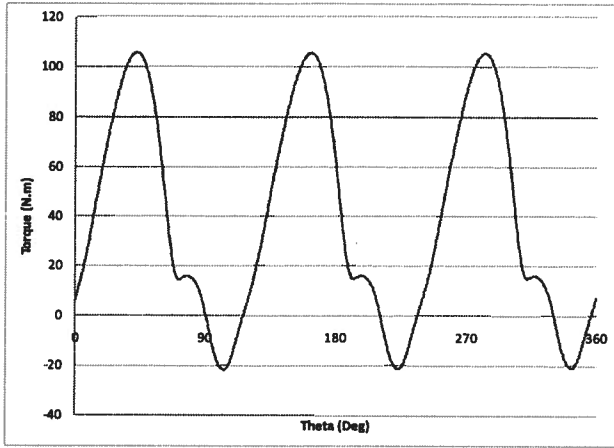


Figure 5-16: Torque curve (3 blades) ; V=1.5 m/s , TSR=2.00

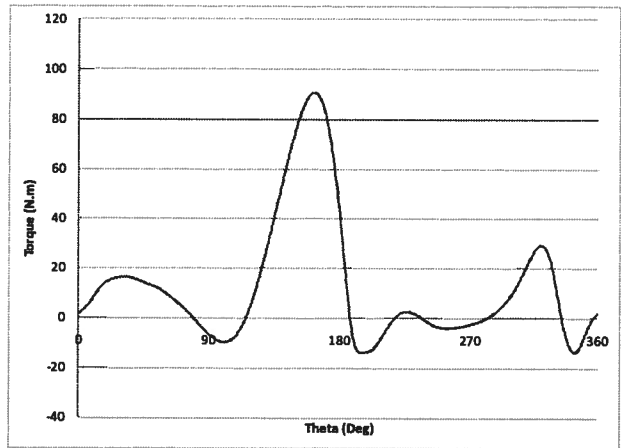


Figure 5-17: Torque curve (single blade) ; V=1.5 m/s , TSR=2.00

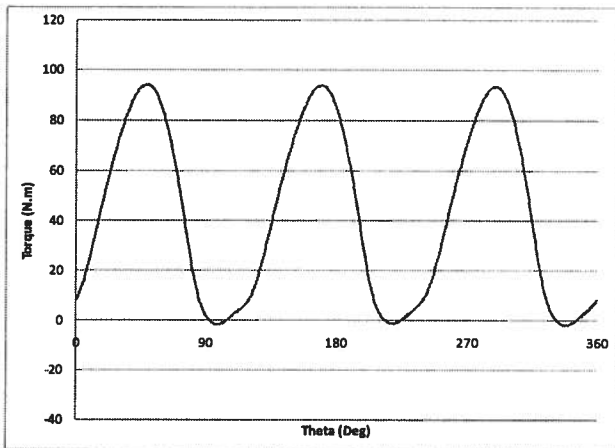


Figure 5-18: Torque curve (3 blades) ; V=1.5 m/s , TSR=2.25

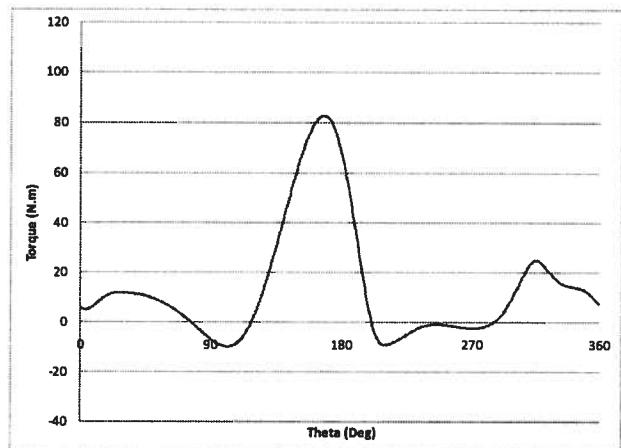


Figure 5-19: Torque curve (single blade) ; V=1.5 m/s , TSR=2.25

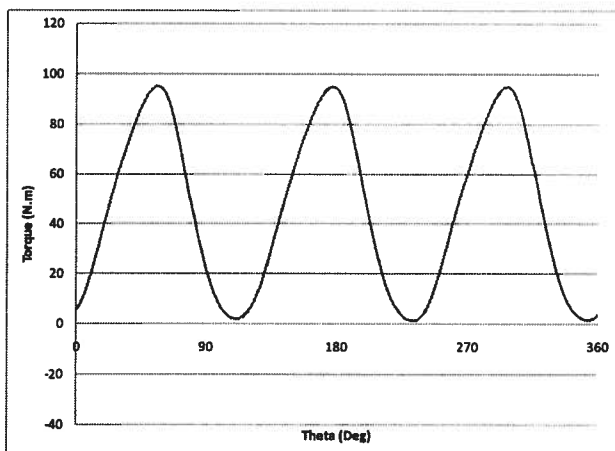


Figure 5-20: Torque curve (3 blades) ; V=1.5 m/s , TSR=2.50

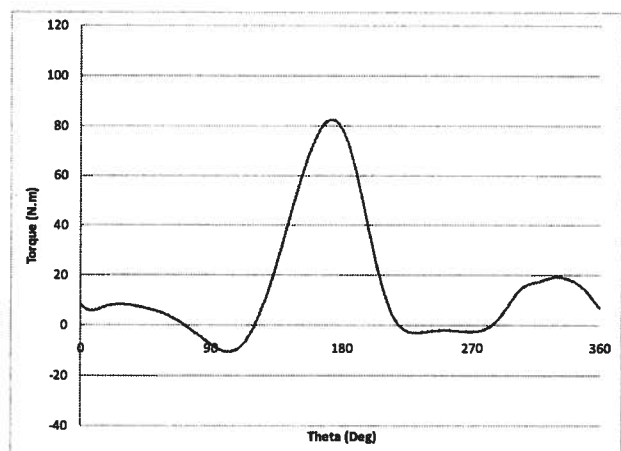


Figure 5-21: Torque curve (single blade) ; V=1.5 m/s , TSR=2.50

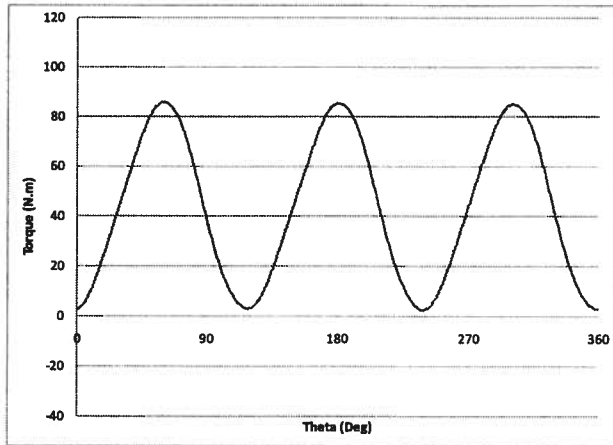


Figure 5-22: Torque curve (3 blades) ; $V=1.5$ m/s , $TSR=2.75$

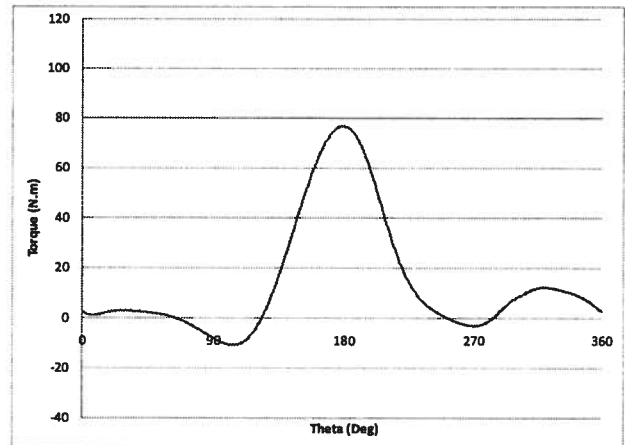


Figure 5-23: Torque curve (single blade) ; $V=1.5$ m/s , $TSR=2.75$

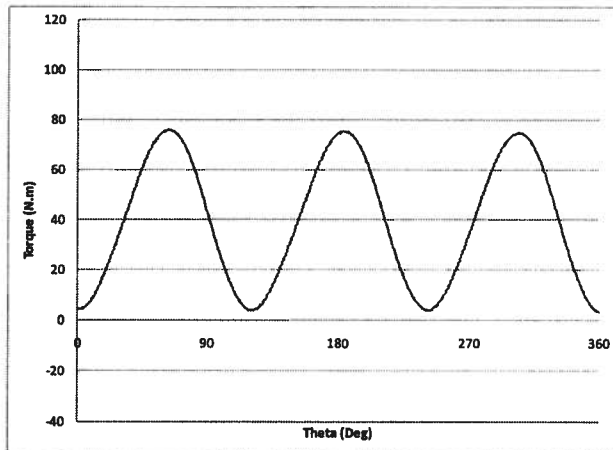


Figure 5-24: Torque curve (3 blades) ; $V=1.5$ m/s , $TSR=3.00$

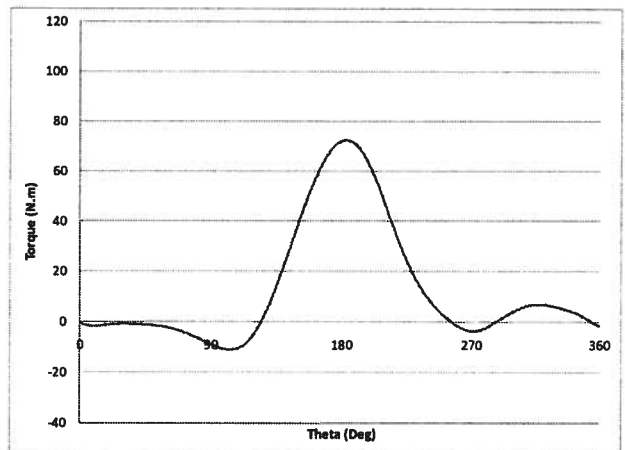


Figure 5-25: Torque curve (single blade) ; $V=1.5$ m/s , $TSR=3.00$

The main results for the higher velocity of 1.5 m/s are very similar to the simulations conducted for $V=1.0$ m/s. Several observations and trends emerge as outlined below:

- Maximum torque magnitude decreases as TSR increases. At $TSR=3.00$ a drop in the average torque is observed.
- The phase angle at peak torque location shifts to the right as TSR increases. However, it is seen that the range is slightly larger and it covers the phase angles from 150 to 180 degrees.
- Similar to the previous results, the single-blade torque curves show a second low-magnitude peak when the blades pass downstream of the central shaft.
- When the TSR increases the downstream peak torque magnitude decreases.

- As TSR increases, the torque generated by the blade at angles between 0 and 90 degrees decreases and reaches a negative average value at TSR's of 2.75 and 3.00. This problem is due to the fact that the shadowing effect of upstream blades affects the performance of downstream blades. This problem will be addressed in Chapter 7 by applying specific duct shapes to re-energize and redirect the flow to increase the power obtained from downstream blades.

After obtaining the torque curves for this set of simulations, the efficiency curve is plotted to observe the change in efficiency as the inlet velocity increases as shown in Figure 5-26. A comparison between the efficiency curves at the two speeds shows that the maximum torque achieved at the higher current speed is about 2 percent greater. Since the only difference between the two simulations is the incoming speed of the flow, it is reasonable to assume that the efficiency of the turbine is a function of current speed. At the scale presently used for the simulations, the Reynolds numbers seen by the blades are in the range of 200,000 to 550,000. The turbine is therefore operating within the transition zone between laminar and turbulent flow where Reynolds effects have a substantial influence on the performance of the turbine. This difference in Reynolds number is maximized at 90 degrees phase angle at which the blades' tangential velocity is opposite to the direction of the incoming flow. As density, chord length, and viscosity of water are constant, the change of Reynolds number at different inlet velocities and TSR's can be specified based on the change in the velocity. Table 5-1 presents the maximum velocity that the blades see and the relative change in the Reynolds number for velocities of 1.0 m/s, 1.5 m/s, and 2.0 m/s. It should be mentioned that the increase in the Reynolds number is measured based on the Reynolds number change compared to the minimum Reynolds number that occurs at V=1.0 m/s and TSR of 2.00 as described by Equation 5-8.

$$Re_{increased} = \frac{Re_{v,TSR} - Re_{v=1,TSR=2}}{Re_{v=1,TSR=2}} \times 100\% \quad \text{Equation 5-8}$$

It can be seen in Table 5-1 Reynolds number increases up to 167% as the velocity and TSR change. It is also predicted that an increased TSR (where Reynolds number is usually higher) can cause the effect of the Reynolds number to be minimized as the Reynolds number is above the transition values.

Table 5-1: Reynolds number changes as TSR and inlet velocity change

V (m/s)	TSR	Maximum Velocity (m/s)	Maximum Reynolds Number	Increase in the Reynolds Number (%)
1	2	3	206,009	0
1	2.25	3.25	223,177	8
1	2.5	3.5	240,344	17
1	2.75	3.75	257,512	25
1	3	4	274,679	33
1.5	2	4.5	309,014	50
1.5	2.25	4.875	334,765	63
1.5	2.5	5.25	360,516	75
1.5	2.75	5.625	386,268	87
1.5	3	6	412,019	100
2	2	6	412,019	100
2	2.25	6.5	446,354	117
2	2.5	7	480,689	133
2	2.75	7.5	515,023	150
2	3	8	549,358	167

Figure 5-26 shows the efficiency curve for velocity 1.5 m/s. It is observed that at lower TSR's where the Reynolds number is in transition zone, the efficiency is higher for V=1.5 m/s compared to V=1.0 m/s. This is because of the fact that at higher Reynolds numbers the separation is postponed and the stall occurs at higher angles of attack.

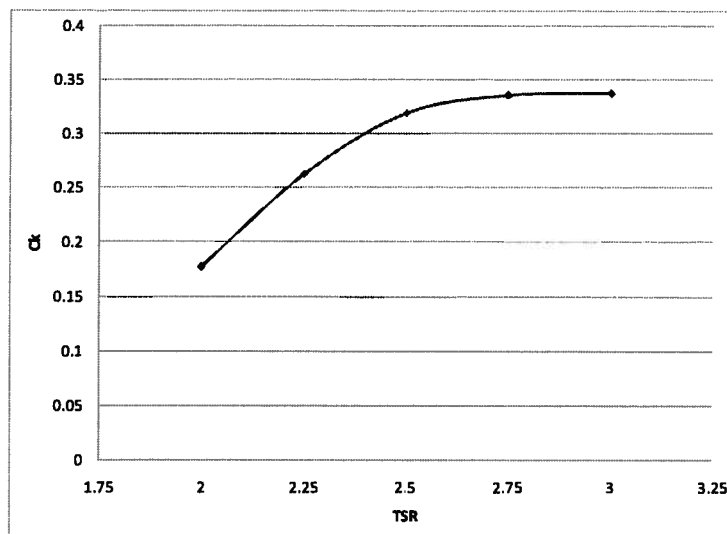


Figure 5-26: Efficiency curve for a free-stream turbine at V=1.5 m/s

Figure 5-27 to Figure 5-36 show the results for the last set of simulations for the free-stream turbine model. The current velocity was 2.0 m/s for this series of simulations. It is observed that the torque magnitude is larger than previous cases as the energy available to the turbine is increased (available power is proportional to velocity cubed). The same trend was also observed for the number of peak points on both 3-blade torque curves and single blade torque curves. The behaviour of the upstream blades on downstream section of the turbine is similar to the previous simulations that resulted in high torque upstream and a lower peak point downstream of the turbine. However, the phase angle range at which the maximum torque occurs is between 150 and 190 degrees. Thus, the trend seen in these sets of simulations is that the peak point occurs at higher phase angles as TSR increases. This fact can be interpreted as a result of the stall angle postponement with increasing Reynolds number.

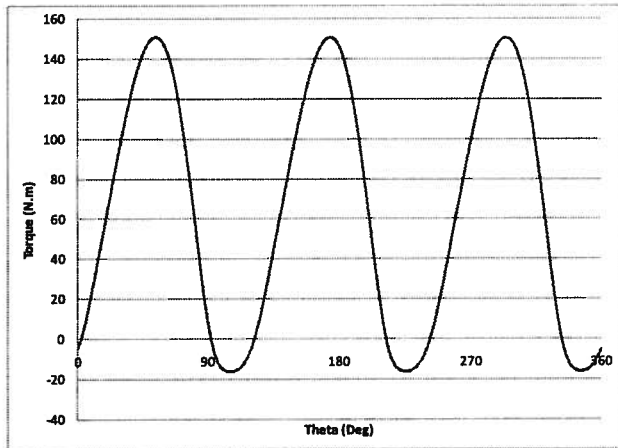


Figure 5-27: Torque curve (3 blades) ; V=2.0 m/s , TSR=2.00

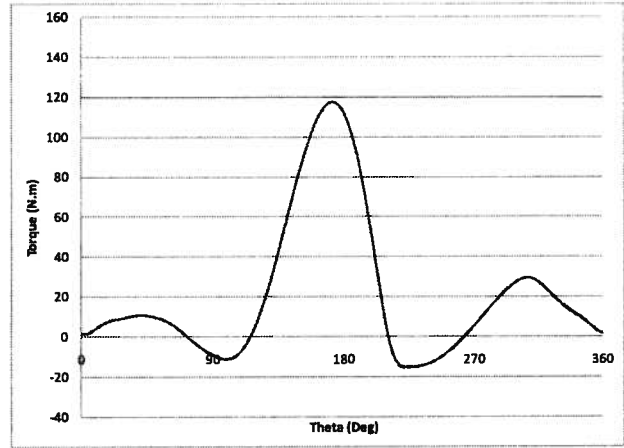


Figure 5-28: Torque curve (single blade) ; V=2.0 m/s , TSR=2.00

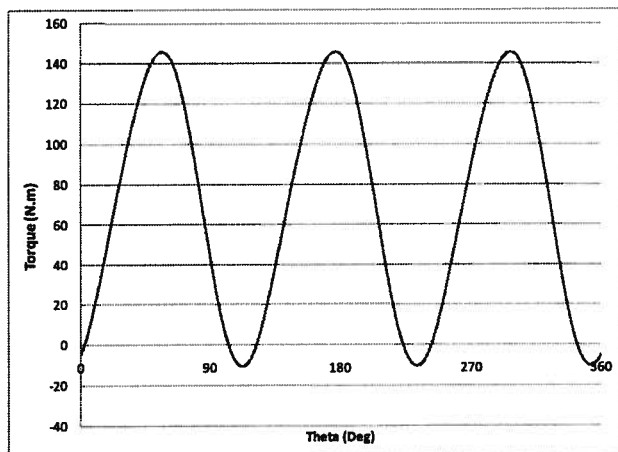


Figure 5-29: Torque curve (3 blades) ; V=2.0 m/s , TSR=2.25

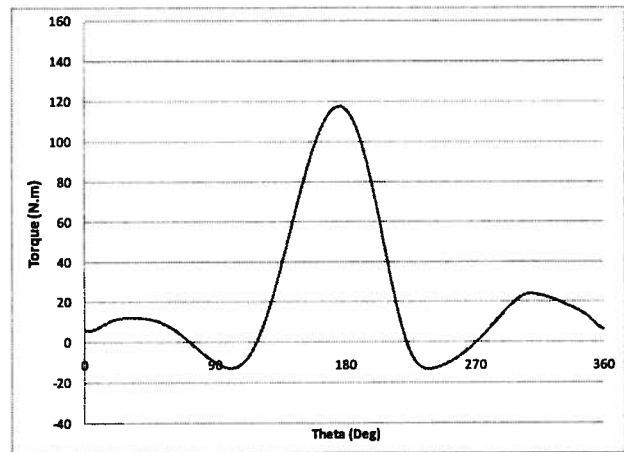


Figure 5-30: Torque curve (single blade) ; V=2.0 m/s , TSR=2.25

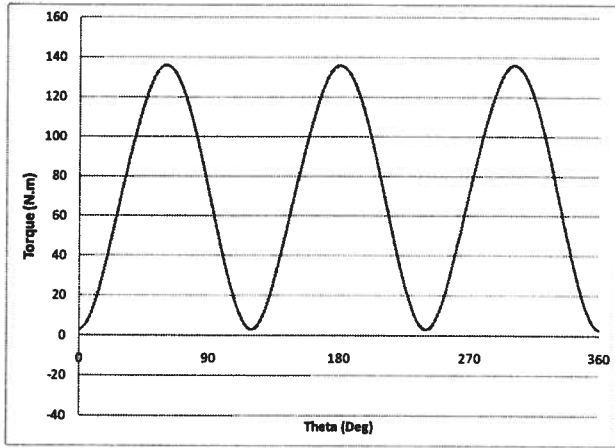


Figure 5-31: Torque curve (3 blades) ; $V=2.0$ m/s , $TSR=2.50$

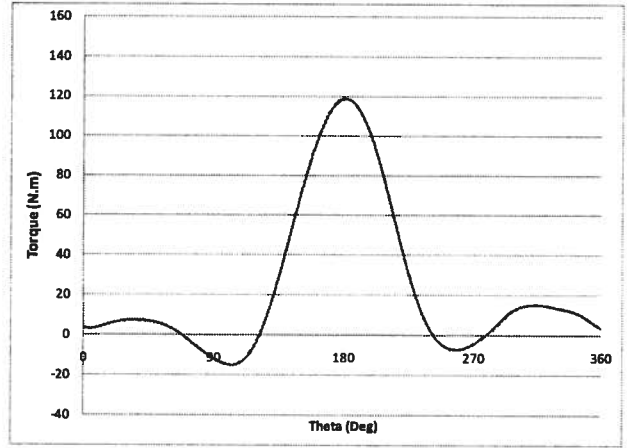


Figure 5-32: Torque curve (single blade) ; $V=2.0$ m/s , $TSR=2.50$

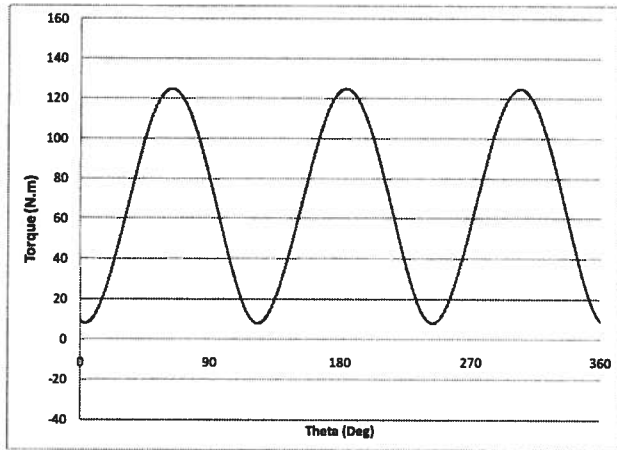


Figure 5-33: Torque curve (3 blades) ; $V=2.0$ m/s , $TSR=2.75$

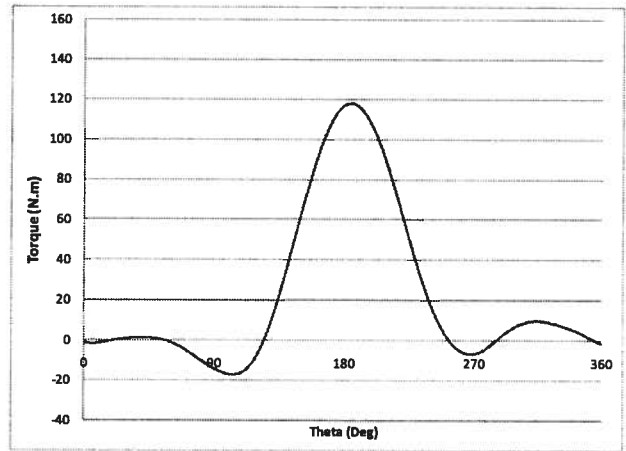


Figure 5-34: Torque curve (single blade) ; $V=2.0$ m/s , $TSR=2.75$

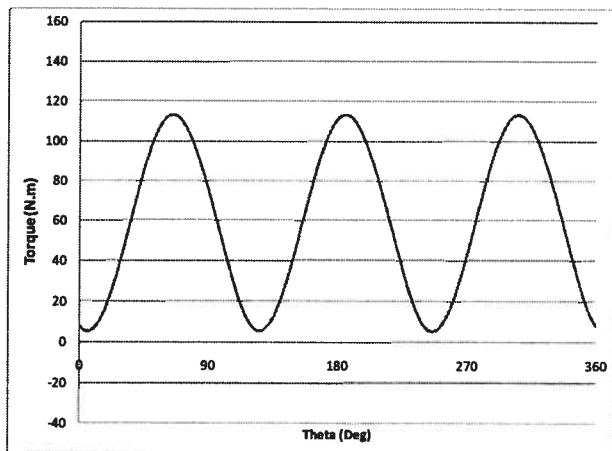


Figure 5-35: Torque curve (3 blades) ; $V=2.0$ m/s , $TSR=3.00$

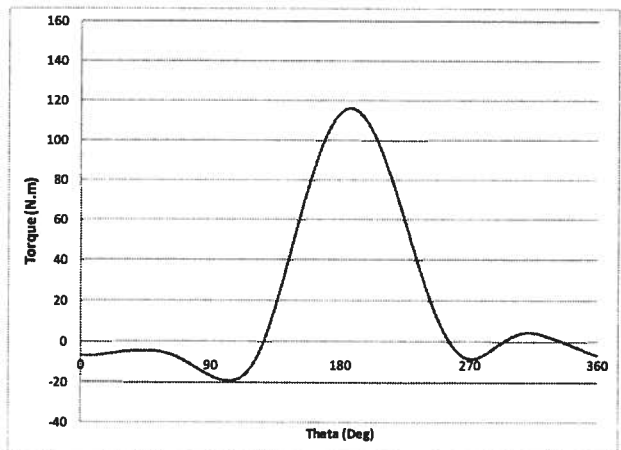


Figure 5-36: Torque curve (single blade) ; $V=2.0$ m/s , $TSR=3.00$

Figure 5-37 shows the efficiency curve for the final set of simulations. Figure 5-38 contains the results for all velocities, previously presented separately in Figure 5-15, Figure 5-26 and Figure 5-37 to provide an easier comparison of efficiencies at different current velocities. In other words, this figure shows the effect of Reynolds number on the rotor performance. As predicted, increasing Reynolds number results in an improvement in performance. This effect is especially significant in the current simulations as the Reynolds number is in the transition range (between 200,000 and 550,000). It can also be concluded from these results that a scaled up version of the turbine can perform at slightly higher efficiency than the current models since the Reynolds number increases with increased size of the device.

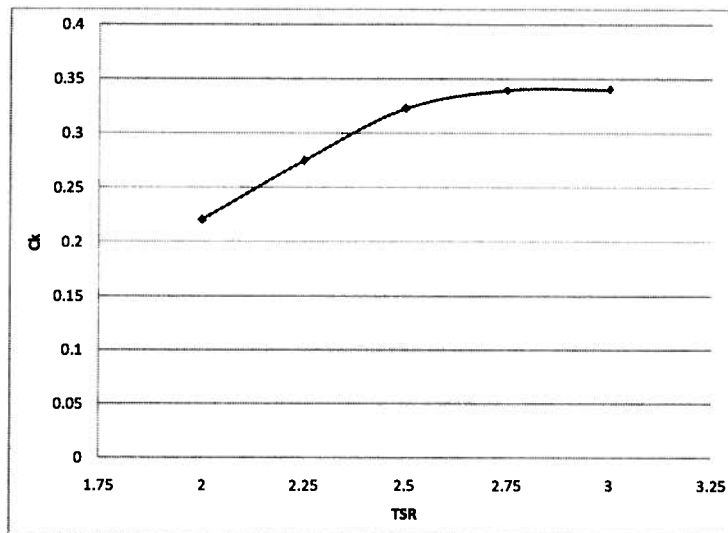


Figure 5-37: Efficiency curve for inlet velocity of 2.0 m/s

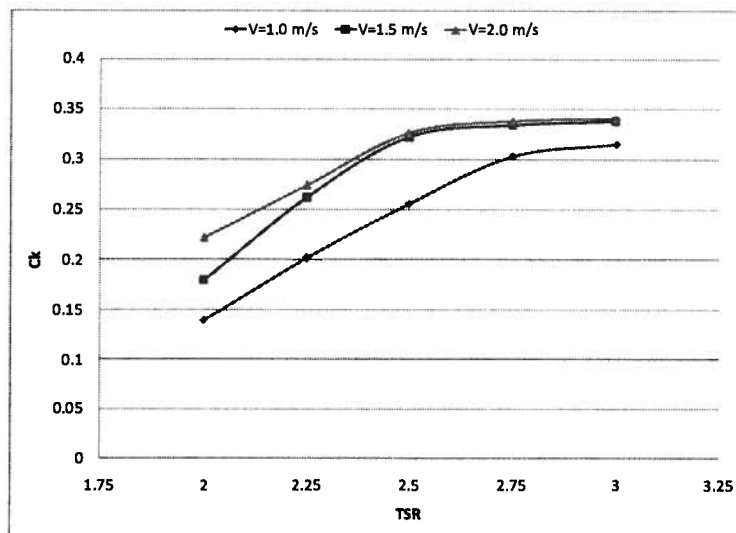


Figure 5-38: Comparison of efficiency for free-stream turbine at different current velocities

5.2 Ducted Turbine Results and Analyses

As a further validation of the numerical models, a set of experiments were conducted at UBC's tow tank in November 2006. The tested turbine had a convex, parabolic shape as shown in Figure 3-1. The solver specification and the simulation procedure were described in detail in Chapter 3. In this section, the results obtained from the simulations of the ducted turbine are presented and analyzed. The comparison of the results with experimental data and the sources of discrepancies will be discussed in Chapter 6.

Figure 5-39 to Figure 5-48 show three-blade and single-blade torque curves for the ducted turbine with an inlet velocity of 1.5 m/s. TSR's tested in these simulations ranged between 2.00 and 3.00 with 0.25 increments.

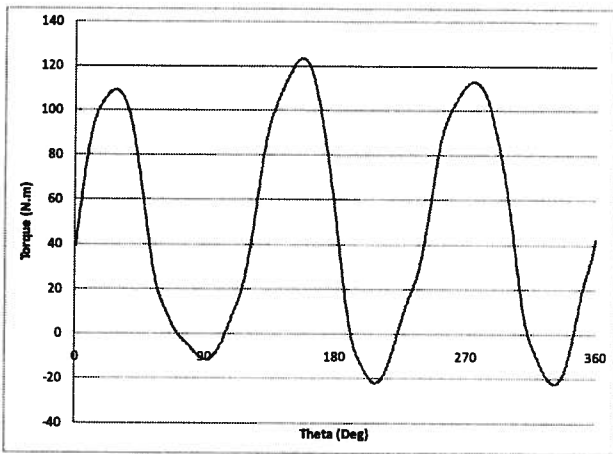


Figure 5-39: Torque curve (3 blades); V=1.5 m/s, TSR=2.00

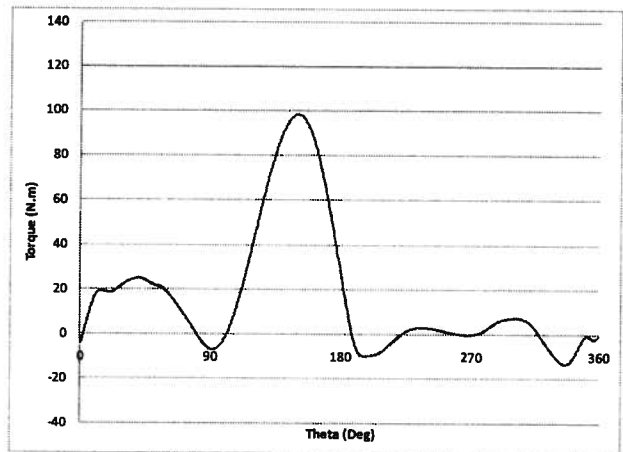


Figure 5-40: Torque curve (single blade) ; V=1.5 m/s , TSR=2.00

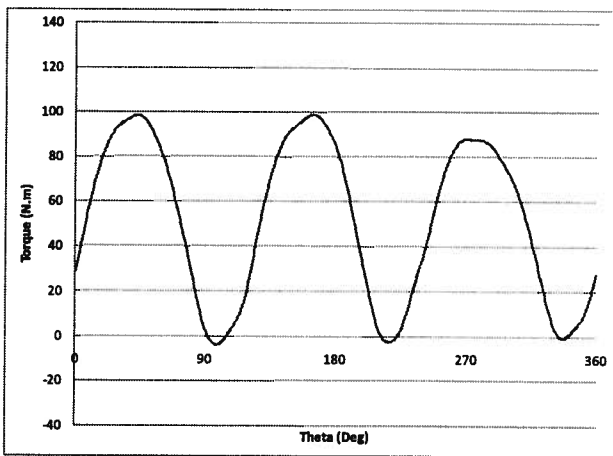


Figure 5-41: Torque curve (3 blades) ; V=1.5 m/s , TSR=2.25

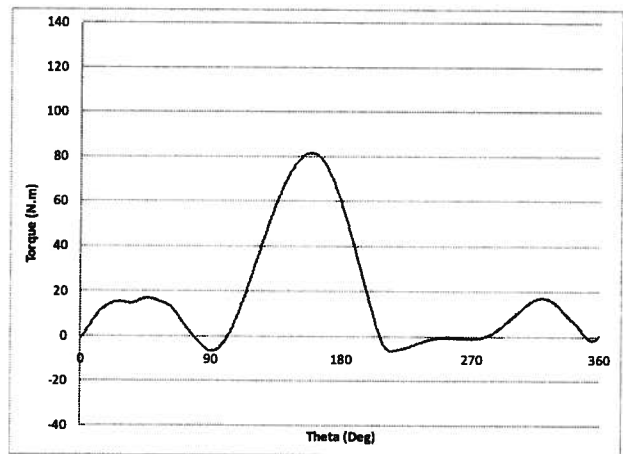


Figure 5-42: Torque curve (single blade) ; V=1.5 m/s , TSR=2.25

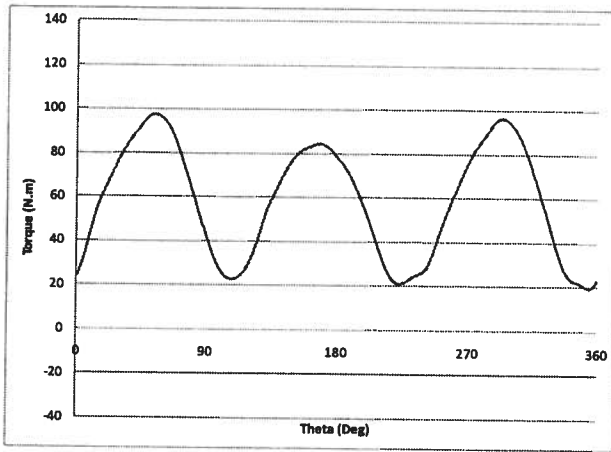


Figure 5-43: Torque curve (3 blades) ; $V=1.5$ m/s , $TSR=2.50$

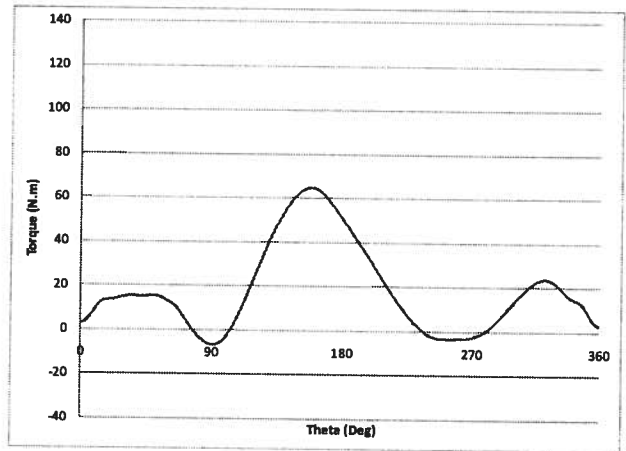


Figure 5-44: Torque curve (single blade) ; $V=1.5$ m/s , $TSR=2.50$

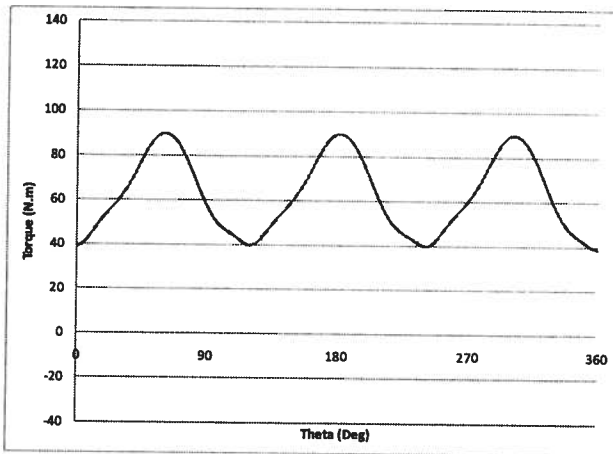


Figure 5-45: Torque curve (3 blades) ; $V=1.5$ m/s , $TSR=2.75$

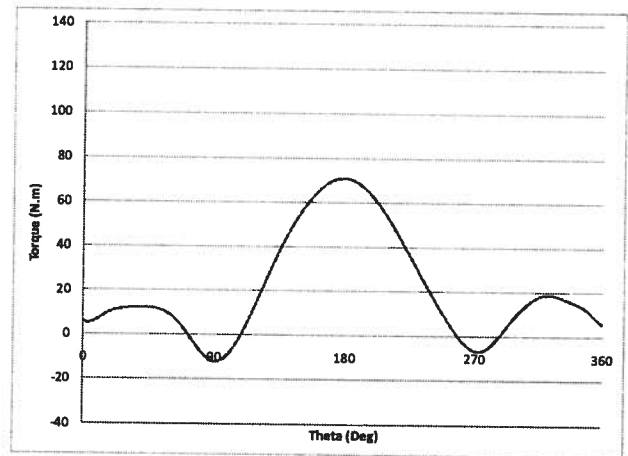


Figure 5-46: Torque curve (single blade) ; $V=1.5$ m/s , $TSR=2.75$

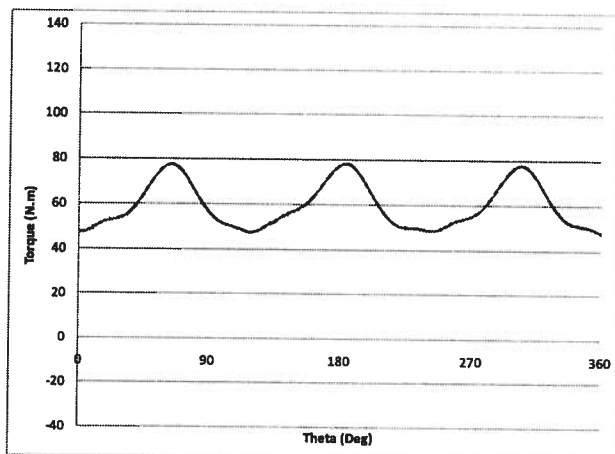


Figure 5-47: Torque curve (3 blades) ; $V=1.5$ m/s , $TSR=3.00$

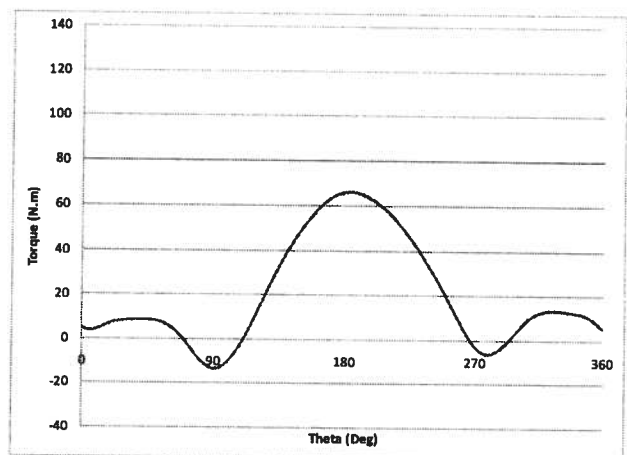


Figure 5-48: Torque curve (single blade) ; $V=1.5$ m/s , $TSR=3.00$

As it is observed at high TSR's, the torque fluctuation is significantly smaller than the torque fluctuation at lower TSR's. A wider single blade torque curve can explain the reason for such a reduction in the torque ripple. A higher velocity downstream of the device increases the angle of attack and hence, the rear blades generate a larger torque than the free-stream case.

Figure 5-49 shows the efficiency curve obtained from the simulations for the ducted turbine at an inlet velocity of 1.5 m/s. The efficiency curve reveals that there is a substantial increase in the efficiency in the presence of the UBC duct around the turbine. The results show that the efficiency can reach 56% at TSR=3.00 with a duct which is approximately 22% larger than the free-stream turbine.

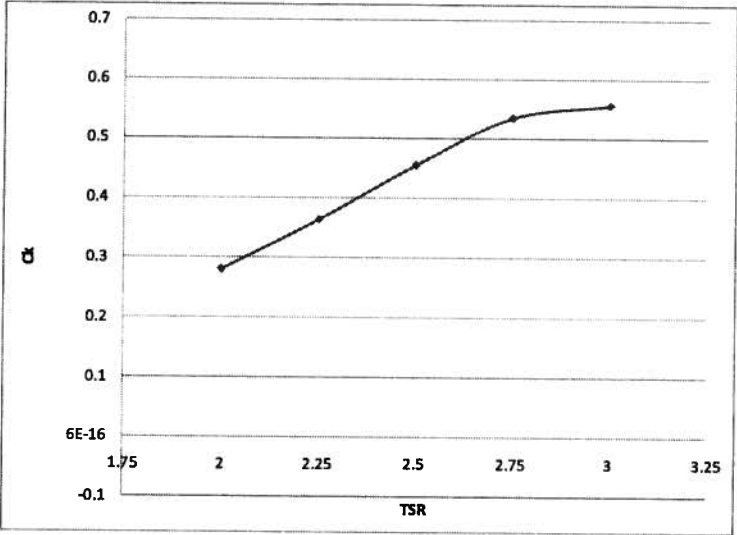


Figure 5-49: Efficiency curve for a ducted turbine at V=1.5 m/s

It should be mentioned that similar to a free-stream turbine simulation, the efficiency is calculated based on the frontal area of the turbine, not based on the frontal area of the device. The same area was used for consistency between free-stream turbine and ducted turbine calculations. This consistency allows for an accurate comparison of the total power generated by each configuration.

The main reasons for the efficiency increase in the case of the ducted turbine can be summarized as below:

- Flow acceleration: The presence of a converging diverging duct results in an increase in the flow velocity guided through the turbine. As the duct sectional area decreases in the flow direction, it can be simply understood from the continuity equation that the velocity should increase and reach its maximum at the mid-section of the duct where the area is minimum. When the velocity is increased, the kinetic energy of the flow will increase significantly as the kinetic energy is proportional to the velocity squared. Hence, the power available to the turbine will increase dramatically with velocity cubed ($P_{av} \propto V^3$). It was also observed that the flow at downstream of the turbine is re-energized compared to the free-stream turbine cases. The flow re-energization also results in higher Reynolds numbers downstream of the device and hence, decreases the separation intensity on the downstream blades. Figure 5-50 and Figure 5-51 show the velocity contours for the TSR's of 2.00 and 3.00 respectively. Comparing Figure 5-50 with Figure 5-13 and Figure 5-51 with Figure 5-14 reveals the fact that the flow velocity is higher downstream of the ducted turbine. Hence the blades at the azimuth angles between -90 and 90 degrees see a larger upstream velocity and can generate a larger torque magnitude. Similar to Figure 5-13 and Figure 5-14, the black regions show the areas where the velocity magnitude is below 70% of the upstream velocity magnitude.

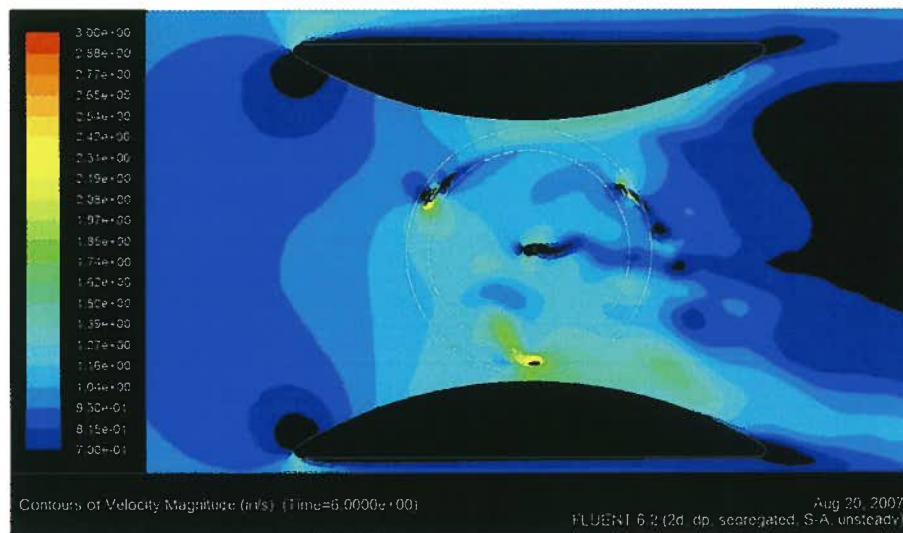


Figure 5-50: Velocity contours at TSR=2.00

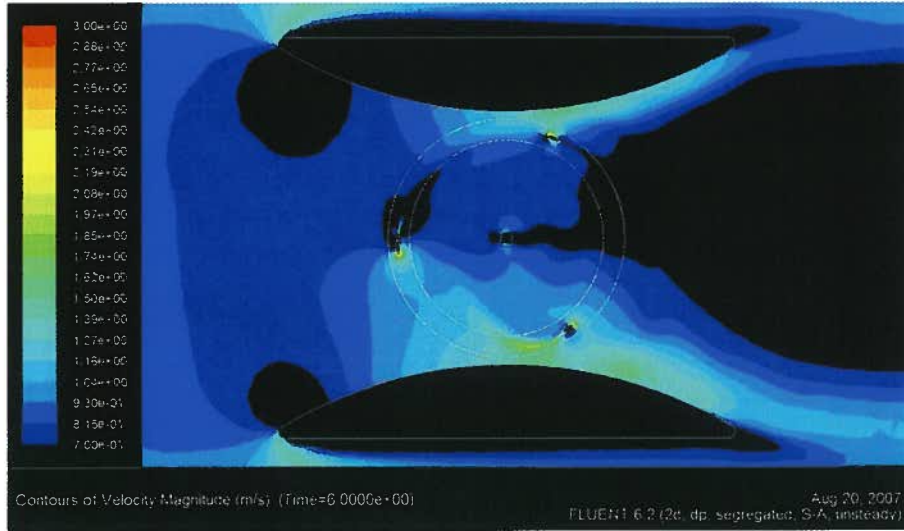


Figure 5-51: Velocity contours at TSR=3.00

- Flow redirection:** Another factor that causes the efficiency to be increased in case of the ducted turbine compared to the free-stream turbine is the change in direction of velocity vectors. The angle of attack seen by the blade is a function of the blade's angular velocity as well as the upstream velocity vector. In the presence of a duct, both the direction and magnitude of the upstream velocity vectors change resulting in different angles of attack compared to the free-stream turbine case. The effect of the change in upstream velocity vector on the angle of attack is compared in Figure 5-52 and Figure 5-53. Figure 5-52 shows the angle of attack a blade sees in the absence of the duct while Figure 5-53 shows the angle of attack in the presence of the duct.

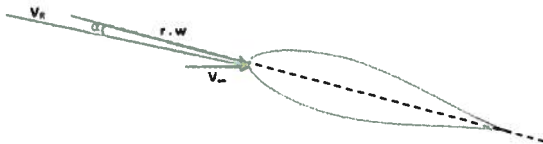


Figure 5-52: Blade's angle of attack calculation for a free-stream turbine

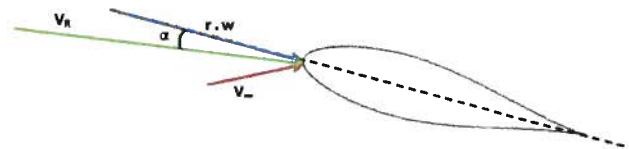


Figure 5-53: Blade's angle of attack calculation for a ducted turbine

In the second set of simulations for the ducted turbine model, the inlet velocity was changed to 2.0 m/s while the tested TSR's were the same as the first series. Similar to the free-stream turbine, the main results of an increase in the current velocity is the effect of Reynolds number on hydrodynamic coefficients. It subsequently affects the shear stress as well as pressure drag, separation and stall angle. Figure 5-54 to Figure 5-63 present the torque curves for this set of simulations. As observed from the torque curves, the torque amplitude is very large at lower TSR's (2.00 and 2.25) as a result of high angles of attack as well as dynamic stall. However, at TSR of 2.50 the torque fluctuations begin to reduce and at TSR=3.00 the torque fluctuations become minimum. The single blade torque curves can explain the reason for the reduction in the torque fluctuations. As shown in the single blade torque curves, the curve is sharp at its peak point at low TSR's, but at higher TSR's this curve begins to become wider and the peak point has a lower value compared to low TSR's. Thus, when single torque curves are super-imposed, the final curve should be smoother if three flatter and wider curves are super-imposed. The Torque Ripple Factor defined by Equation 5-9 can be defined and used to quantify the torque fluctuations magnitude for different cases.

$$TRF = \frac{T_{max} - T_{min}}{T_{avg}} \tag{Equation 5-9}$$

The results suggest that at V=1.5 m/s and TSR=2.75 the TRF is reduced from 1.92 for a free-stream turbine to 0.82 for a ducted turbine. It is also observed that at V=2.0 m/s and TSR=2.75, the TRF is reduced from 1.72 for the free-stream turbine to 0.37 for the ducted turbine.

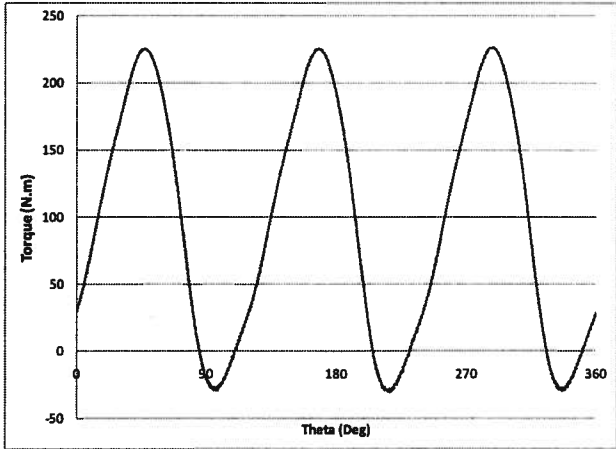


Figure 5-54: Torque curve (3 blades) ; V=2.0 m/s , TSR=2.00

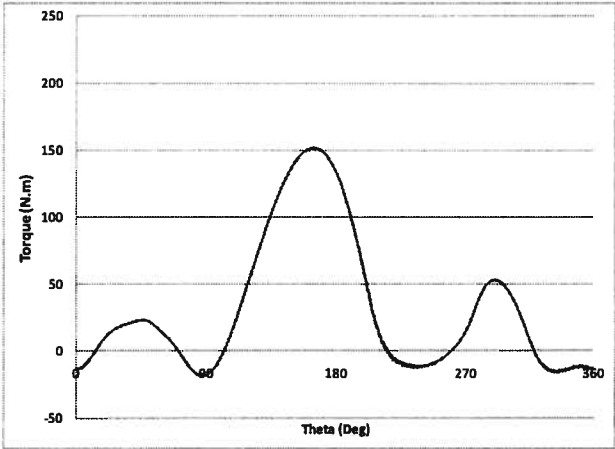


Figure 5-55: Torque curve (single blade) ; V=2.0 m/s , TSR=2.00

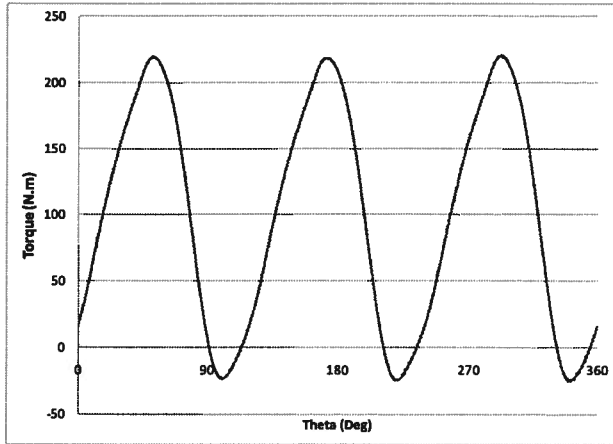


Figure 5-56: Torque curve (3 blades) ; $V=2.0$ m/s , $TSR=2.25$

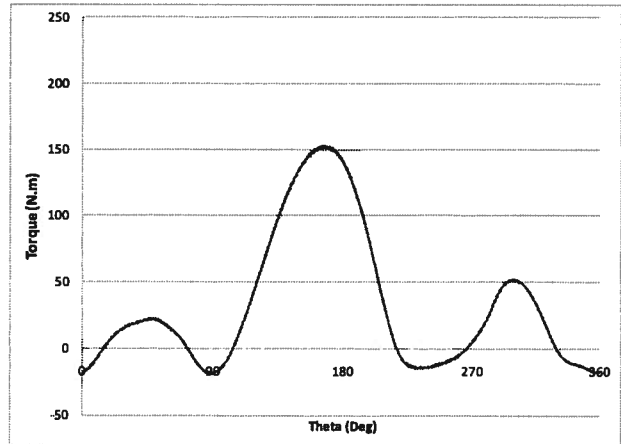


Figure 5-57: Torque curve (single blade) ; $V=2.0$ m/s , $TSR=2.25$

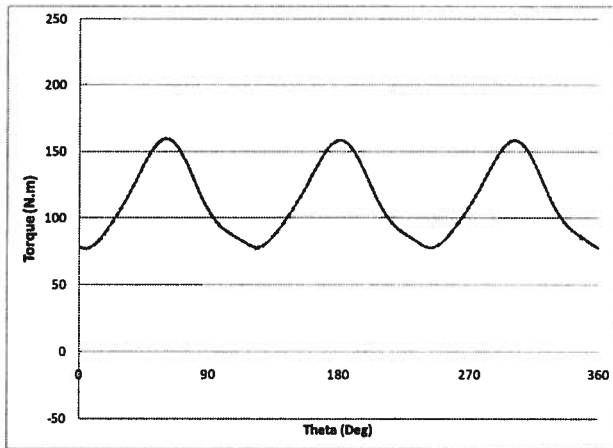


Figure 5-58: Torque curve (3 blades) ; $V=2.0$ m/s , $TSR=2.50$

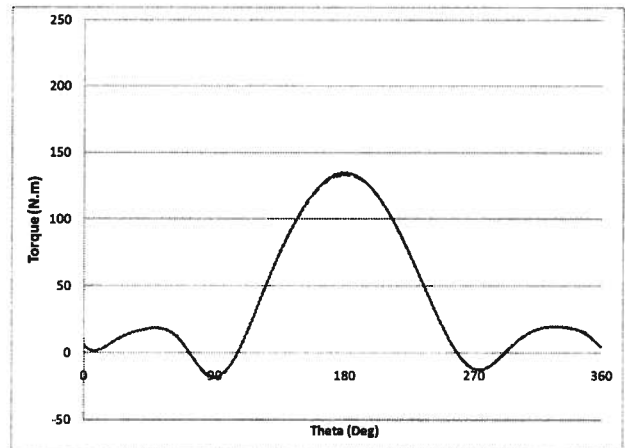


Figure 5-59: Torque curve (single blade) ; $V=2.0$ m/s , $TSR=2.50$

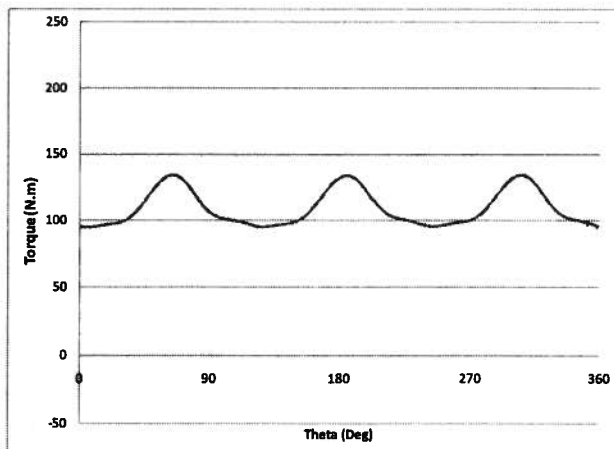


Figure 5-60: Torque curve (3 blades) ; $V=2.0$ m/s , $TSR=2.75$

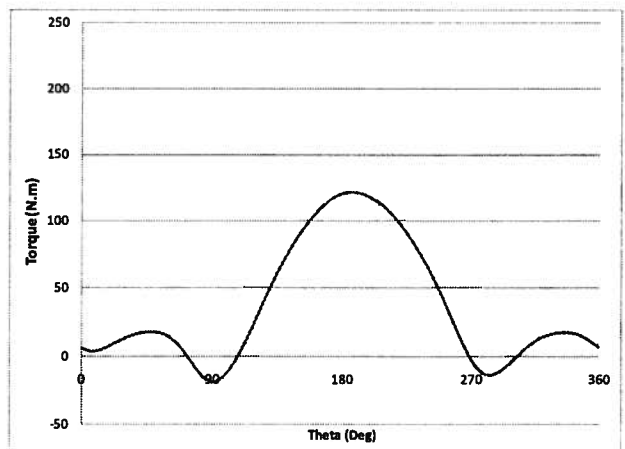


Figure 5-61: Torque curve (single blade) ; $V=2.0$ m/s , $TSR=2.75$

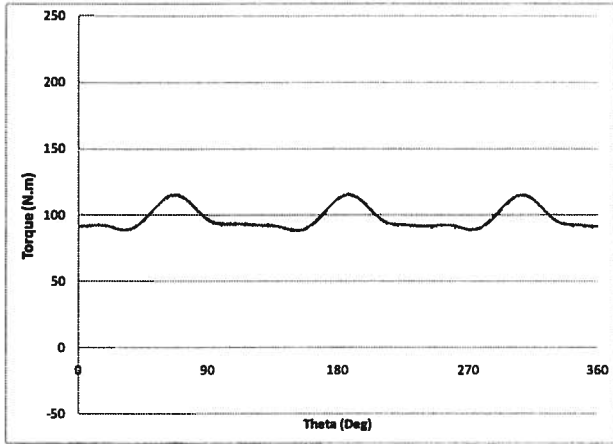


Figure 5-62: Torque curve (3 blades) ; V=2.0 m/s , TSR=3.00

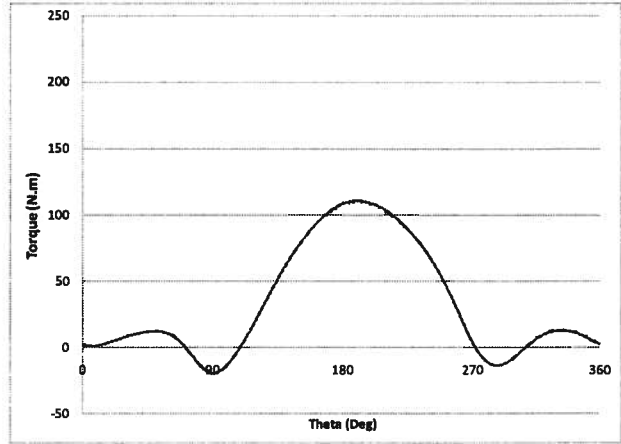


Figure 5-63: Torque curve (single blade) ; V=2.0 m/s , TSR=3.00

The torque curves show that the torque amplitude decreases significantly as TSR increases without reducing the efficiency. The TRF for TSR=2.00 was 2.69 while for TSR=3.00 TRF decreased to 0.29. Figure 5-64 present the efficiency curve for the ducted turbine at V=2.00 m/s.

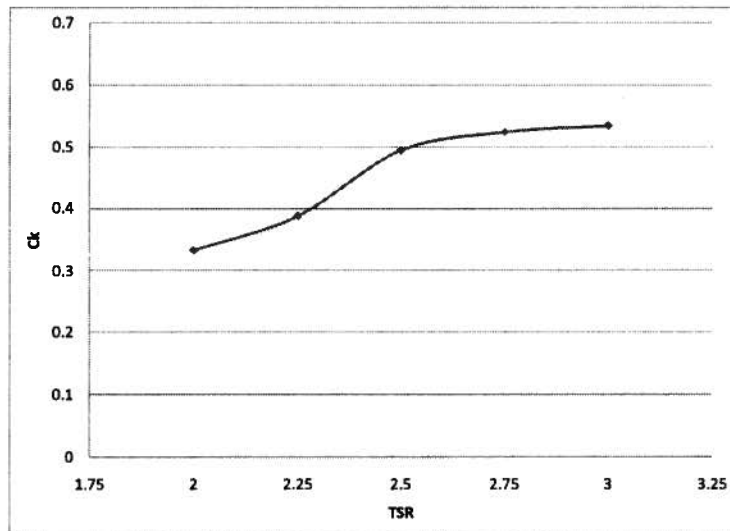


Figure 5-64: Efficiency curve for a ducted turbine at V=2.0 m/s

6. Discussion

In Chapter 5, the simulation results obtained for a free-stream and ducted turbine models were presented. One of the main tasks in every numerical work is to validate the results obtained from a numerical model with usually experimental data as the reference. Thus, the simulation results obtained for the UBC turbine were compared with the experimental data obtained at UBC's tow tank in September 2007. The experimental data includes the free-stream and ducted turbine test results.

As it was described in previous chapters, the CFD model developed for the tidal turbine in the current research is a two-dimensional model. A 2D model was developed because of its acceptable computational cost. Also, as blades' aspect ratio were relatively high (about 10), it was predicted that a 2D simulation can more or less represent the trends of a 3D model. Development of a 3D model was far beyond the financial capabilities and computational facilities available at this stage of the product development.

In order to be able to compare the experimental data with the results of the numerical model, it is necessary to compare results of similar geometries. There are two main geometric differences between the numerical model and the experimental model:

- The arms and the attachment assembly connecting the blades to the central shaft (Figure 6-1 and Figure 6-2)



Figure 6-1: Arms-Shaft connections



Figure 6-2: Arm-Blade connection

- Three-dimensional blades in experiments vs. two-dimensional airfoils in the CFD model

There are also some other physical discrepancies between the two models such as the roughness of the blades and the blades' profile which is cut at trailing edge in experiments.

To be able to compare the performance of a turbine with connecting arms (experimental model) and the one without the connecting arms (numerical model), the effect of arms on the performance should be excluded. The next section is dedicated to the approach taken to exclude the arms effect from the experimental data.

6.1 Arms Effect

The arms and the attachment assembly (which, from now on will be called the connection assembly), have a significant effect on the performance of the turbine. Although the structural difficulties associated with the design of the arms are very important, the main focus in the current research is on the hydrodynamic impact of the arms on the flow field and the turbine's hydrodynamic performance.

The most significant effect of the arms on the performance is due to the counter torque generated by the arms when the blades are rotating. The parasitic drag caused by the rotation of the arms is the source of the counter torque generated by the arms. Consequently, the counter torque generated by the arms lowers the average torque generated by the system over a cycle and hence lowers the turbine efficiencies at all TSR's. As the velocity seen by the blades at different TSR's and inlet velocities change, the parasitic drag generated by the arms, which is proportional to velocity square, will change considerably. Hence, the counter torque created by the arms drag can be described as a function of TSR.

In order to quantify the counter torque generated by the arms, a set of experiments were conducted for different velocities and TSR's for turbine without blades. In other words, the turbine blades were detached but the arms remained on the system (Figure 6-3).

The counter torque generated by the arms can be obtained using Equation 6-1. C_k can be calculated using an empirical formula (Equation 6-2) obtained from the test results of the turbine with no blades.

$$T_{arms} = C_k \left(\frac{1}{2\omega} \rho v^3 A_{front} \right) \quad \text{Equation 6-1}$$

$$C_k = (-0.020244)TSR^2 + (0.041997)TSR - 0.034278 \quad \text{Equation 6-2}$$

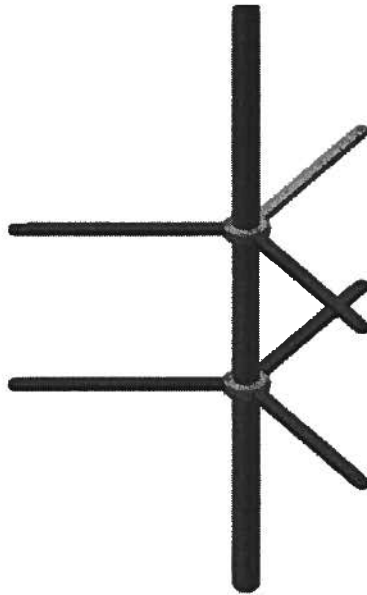


Figure 6-3: Arms' parasitic drag experimental model

After obtaining the counter torque generated by the arms using the above equation, the torque value for a turbine without the arms can be calculated by subtracting the arms' torque from the total torque generated by the blades at the same speed and TSR (Equation 6-3).

$$T_{w/o\ arms}(V, TSR) = T_{w\ arms}(V, TSR) - T_{arms}(V, TSR) \quad \text{Equation 6-3}$$

It is important to note that although the above equation describes the effect of the arms on the torque magnitude, it is only a rough approximation of the arms' effect on the performance of the complete system. An important phenomenon that was neglected in this approach will be discussed later in this chapter when the sources of discrepancies are described. A comparison of FLUENT results with and without the arms effect is presented in Figure 6-4. The flatness in the efficiency curve obtained from the simulations is mainly due to subtracting the arms counter torque from the generated torque by the blades. It is also important to consider the arms effect when optimum operational condition of the device is specified.

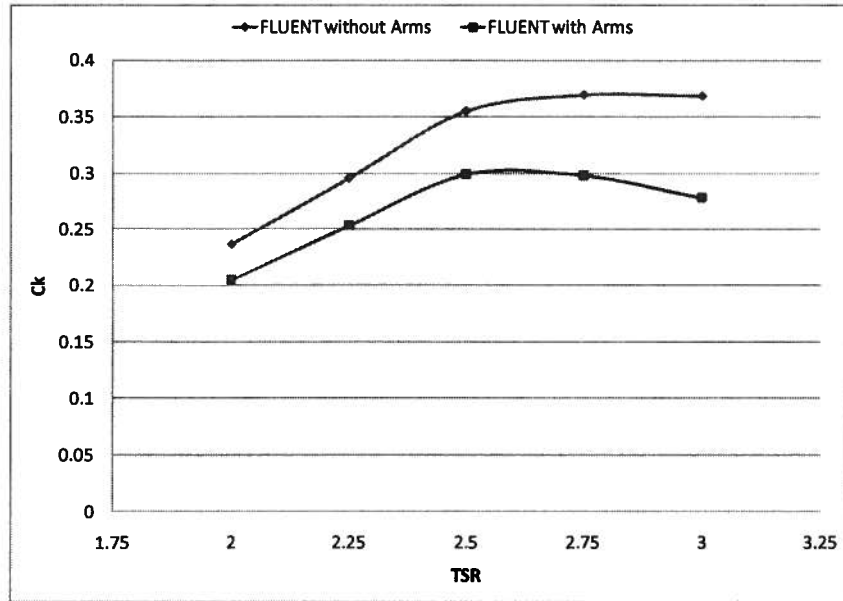


Figure 6-4: Comparison of the efficiency curve with and without the arms effect (V=1.5 m/s)

6.2 Validation of Numerical Results

In this section the numerical and experimental results for the torque and power generated at different velocities and TSR's will be presented. The results presented include the comparison of the power generated by the free-stream turbine at TSR's ranging between 2.00 and 3.00 at velocities of 1.5 and 2.0 m/s. Also, the torque curve will be compared for a few TSR's and the differences will be discussed. Moreover, to obtain more confidence in the validity of the simulations, the results for a ducted turbine are compared with experiments.

Figure 6-5 and Figure 6-6 show the comparison of efficiencies predicted by the numerical model and experiments for a free-stream turbine at current velocities of 1.5 m/s and 2.0 m/s respectively.

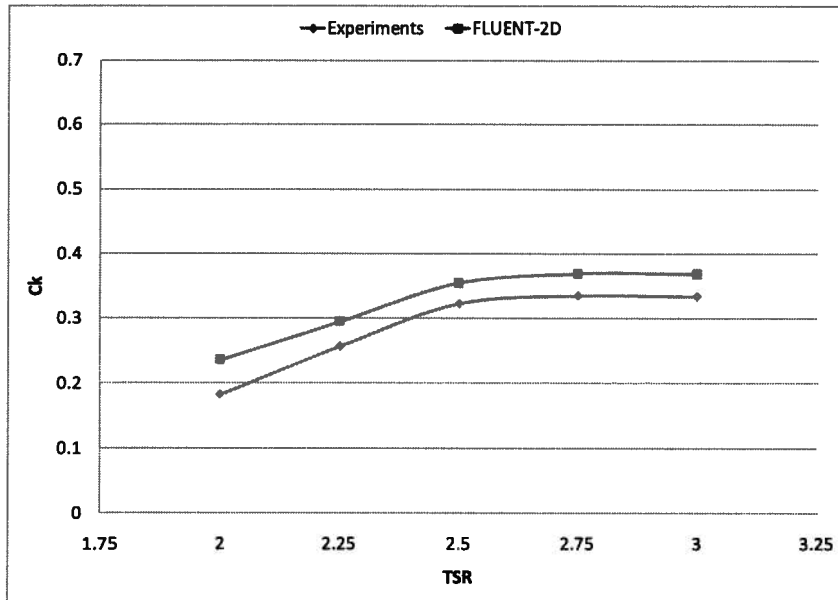


Figure 6-5: Comparison of numerical and experimental efficiencies for a free stream turbine at V=1.5 m/s

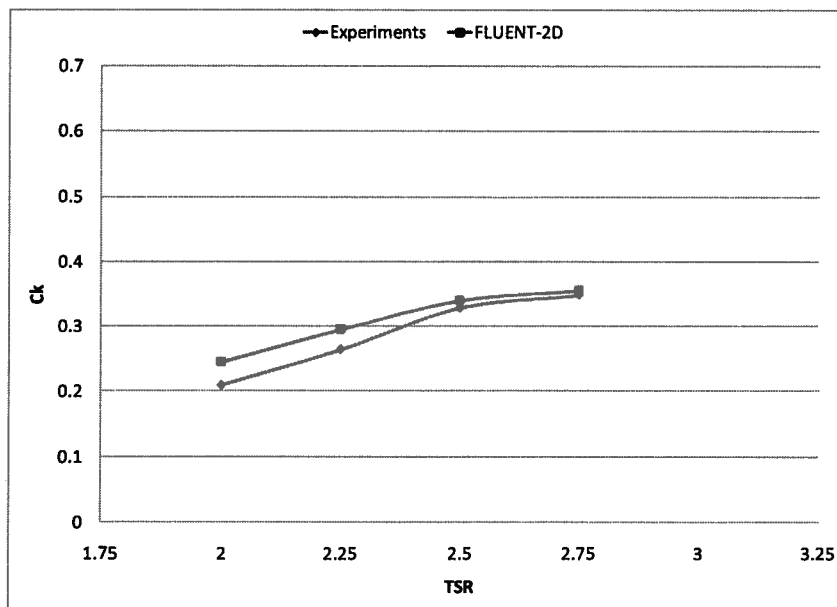


Figure 6-6: Comparison of numerical and experimental efficiencies for a free stream turbine at V=2.0 m/s

The results show that the power coefficient by the numerical model is properly predicted and the results are close to the experimental results. The experimental results presented in these figures are the most recent results obtained at UBC in September 2007. These results are significantly closer to the numerical

model predictions compared to the previous experimental results obtained at UBC in November 2006. The main changes in the recent experiments were the new drive-terrain with a worm-gear which was expected to provide a more rigid system compare to the previous drive-terrain. Another important change in the new experimental model was replacing two arms in the quarter-span of the blade with three arms, one at the mid-span and two at the blades' tips as shown in Figure 6-7 and Figure 6-8.



Figure 6-7: 3-Arm configuration

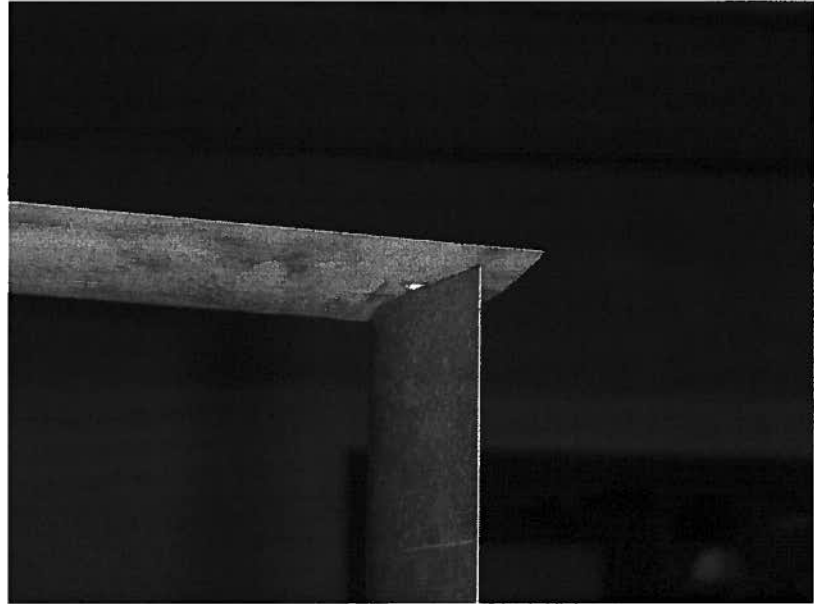


Figure 6-8: Arm-blade connection at the blade's tip

It was observed that placing the arms at the tip of the blades affects the performance of the turbine significantly. The efficiency was increased up to 100% relative to the November 2006 tests due to the change in the arms' profile and their attachment location. This is predicted to be due to the prevention of induced flow circulation from the pressure side to the suction side. In other words, the arm connection at the tips acts as a winglet in the airplane wing design which results in a decreased induced drag. Thus, 2D simulations better represent the recent series of experiments with three arms compare to the previous experiments with two arms in the quarter span.

After validation of a free-stream turbine, the ducted simulations should be validated. The comparison of the experimental and numerical results for the UBC duct configuration is presented in Figure 6-9 ($V=1.5$ m/s) and Figure 6-10 ($V=2.0$ m/s).

The results show that the predicted numerical results are close to the experimental results. It is observed that the numerical efficiencies are predicted slightly higher than the experimental results. The reason for that is because of the 3D effects included in the experiments as well as the effect of the top and bottom walls (Plexiglass plates in Figure 6-18) confining the turbine in the duct. The boundary layer separation from these plates can increase the flow disturbance and reduce the torque in the upstream section of the turbine.

Also, a variable RPM creates a different flow field compared to the numerical model with an absolutely constant value for RPM. Variable RPM also affects the amplitude of the torque curve as well as the phase angle where the torque curve reaches its maximum value.

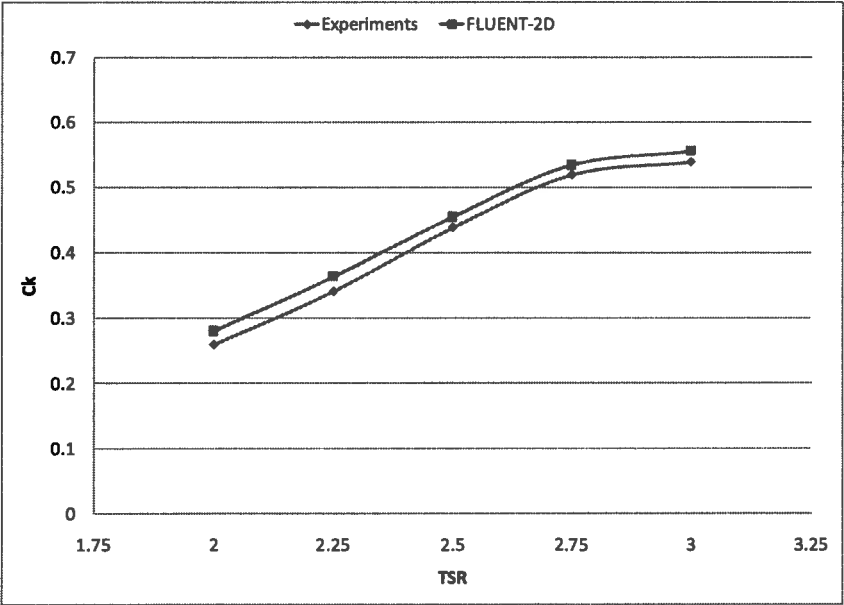


Figure 6-9: Comparison of numerical and experimental efficiencies for a ducted turbine at V=1.5 m/s

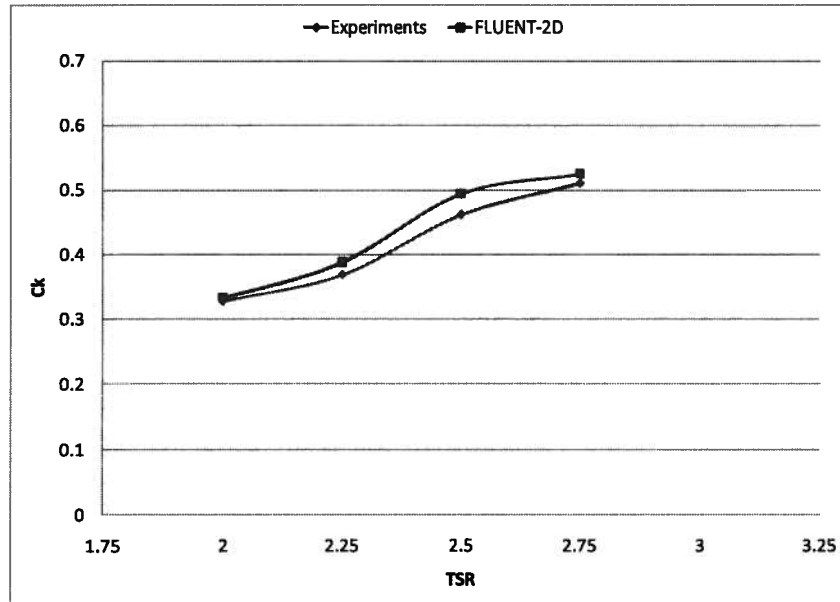


Figure 6-10: Comparison of numerical and experimental efficiencies for a ducted turbine at V=2.0 m/s

The comparison of the torque curves for free-stream and ducted turbines (Figure 6-11 through Figure 6-14) show that the torque amplitude is under-predicted in the numerical models compared to the experiments. This discrepancy may be because of two main reasons; the drive-terrain and dynamic stall simulation. As it was mentioned earlier in this chapter, the drive-terrain was replaced in the last experiments to create a more rigid system, but RPM monitoring showed that the motor response was not fast enough to keep a constant RPM. Thus, the variable RPM problem continued to affect the results. Also, the coupling between the shaft and motor was slightly loose and caused a bucket shape in the torque curve especially at lower TSR's. Another source of discrepancy in experimental and numerical torque is the dynamic stall phenomenon. As the blade angle of attack is high in low TSR's, dynamic stall effect becomes more important in simulations. An extensive research on the numerical simulation of an airfoil in high angles of attack using different turbulence models and comparison with experimental results showed that the stall angle is usually predicted in lower angles and the lift coefficient is slightly less at stall angle in numerical models [41]. This could be due to the low level of accuracy in the turbulence models at high angles of attack.

As seen in the torque comparison figures, variable RPM as well as dynamic stall simulation problems also create a phase difference in the torque curves. At lower TSR's where the torque magnitude is not large, the phase difference between the numerical and experimental torque curve for the free-stream

and ducted turbine is 43 and 42 degrees respectively. However, it is observed that at higher TSR's the phase difference is more pronounced. In fact, the motor cannot quickly respond to the changes in the torque magnitude when the torque generated by the blades is large. The phase difference between the numerical and experimental phase is 55 degrees for free-stream turbine and 50 degree for the ducted turbine. However, the trends are found to be similar in the numerical model and in the experiments. In the case of the free-stream turbine, the phase angle is shifted by 18 degrees in numerical results while it is shifted by 24 degrees in the experiments. For the ducted turbine, the phase shift is 19 degrees in numerical results while it is 15 degrees in the experimental results. A comparison between the torque values obtained from FLUENT and numerical results obtained from a Free Vortex Method developed in UBC Naval Architecture Lab showed agreement for torque amplitude as well as the phasing [40].

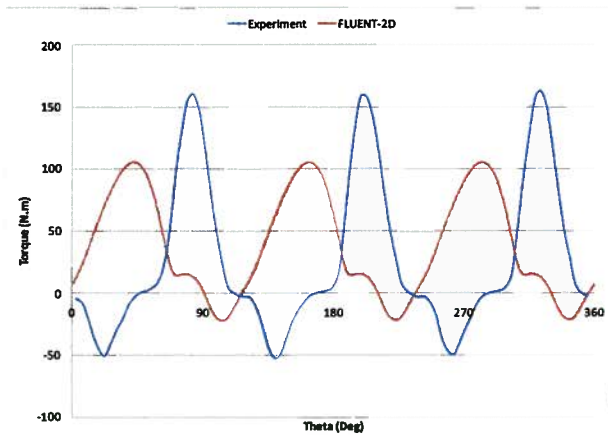


Figure 6-11: Comparison of experimental and numerical free-stream turbine torque at $V=1.5$ $TSR=2.00$

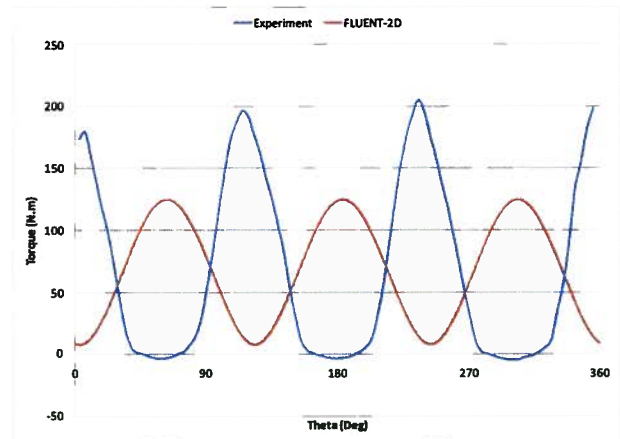


Figure 6-12: Comparison of experimental and numerical free-stream turbine torque at $V=2.0$ $TSR=2.75$

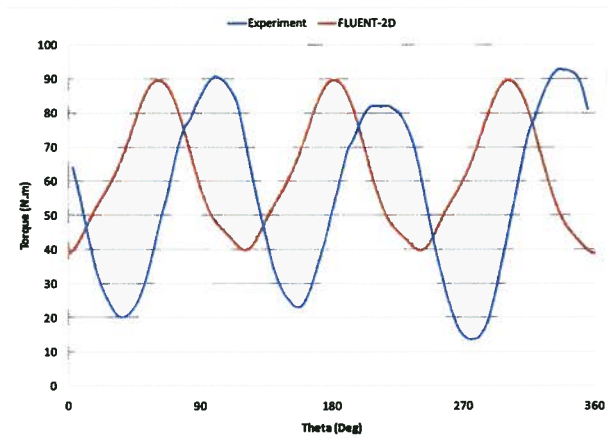


Figure 6-13: Comparison of experimental and numerical ducted turbine torque at $V=1.5$ $TSR=2.75$

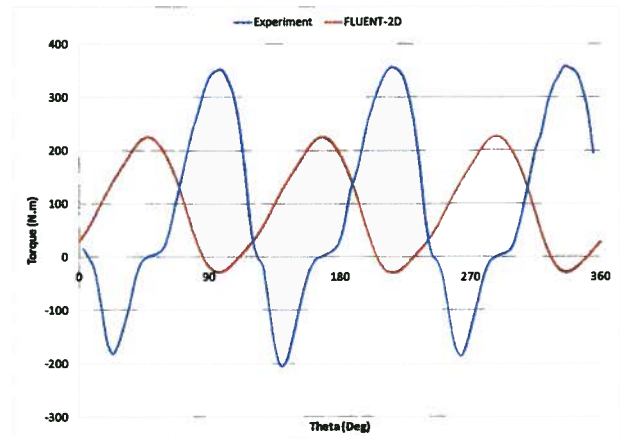


Figure 6-14: Comparison of experimental and numerical ducted turbine torque at $V=2.0$ $TSR=2.00$

Also, a comparison of the FLUENT results with the results obtained from the Discrete Vortex Method code, developed in the Naval Architecture Lab, shows a good agreement between the two numerical models (Figure 6-15 and Figure 6-16).

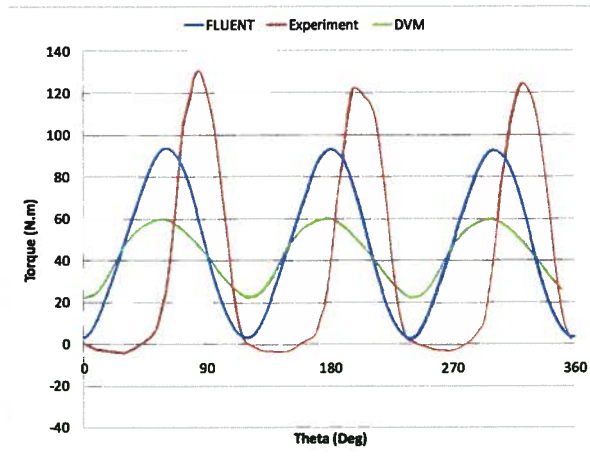


Figure 6-15: Comparison of 3-blade torque obtained from FLUENT, DVM, and Experiments ($V=1.5$, $TSR=2.50$)

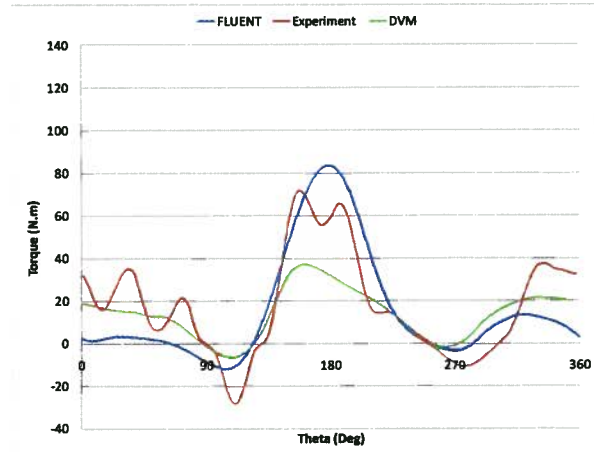


Figure 6-16: Comparison of single-blade torque obtained from FLUENT, DVM, and Experiments ($V=1.5$, $TSR=2.50$)

6.3 Sources of Discrepancy

As it was described in the previous section, there are discrepancies between the results obtained from the numerical model and the experimental model results. In this section, the sources of these discrepancies will be discussed in more details. The sources of discrepancies can be described in two main categories, numerical errors, and experimental errors. Below is a summary of the errors associated with the experiments and numerical models:

- Numerical sources of discrepancy
 - 2D vs. 3D: The first reason of discrepancy between the numerical simulation results and the experimental results is due to the difference in the geometry of the simulated model. As it was briefly mentioned in the previous section, the simulations were conducted for a 2D turbine without any arms. Three-dimensional effects including tip vortices are neglected in the conducted simulation.
 - Arms effects: The arms not only have a significant effect on the generated torque by the system, but also disturb the flow field inside the turbine area and affect the downstream blades performance. Even, subtracting the arms counter torque can not accurately exclude the arms effect from the experimental data because the blade-arm interaction and the blade-arm connection effects are still neglected in this approach.

- **Blade Shape:** One of the geometric differences between the numerical model and experimental model is the difference in the shape of the blade's trailing edge. While the numerical model has the blades with sharp trailing edges, the experimental model blades' trailing edges were cut off due to manufacturing purposes. As a matter of fact, a sharper trailing edge can be manufactured; however, making the trailing edge as sharp as possible could increase the manufacturing time and cost. In addition, a very sharp trailing edge is not predicted to be a viable and durable design. It is predicted that after the installation of the turbine into the ocean, debris, algae, and ocean species will gradually accumulate on the surface of blades; hence, sharpening the trailing edge may not last for a long time. In addition, a sharp trailing edge may also entail environmental issues such as endangering fish and other ocean species that may be cut by the sharp blade edges.
- **Blade Roughness:** Another discrepancy between the numerical and experimental model is that the roughness of the blades was not taken into account in the simulations. Although the blades were built very smooth, they still had a physical roughness that could make a slight difference in the experimental results and numerical results. Although the roughness of the blades can improve the performance by postponing the stall, the negative effect of the increased frictional drag caused by the blade's roughness is dominant and causes the average torque to be decreased.
- **Turbulence modeling:** Turbulence modeling is one of the most important and complicated problems in computational fluid dynamics. Although many turbulence models were developed by scientists and researchers, no turbulence model has been recognized as a superior one. The inaccuracy of turbulence models are more pronounced at higher angles of attack with significant separation of the flow. In the current research, the direct effect of this shortage of accuracy at higher TSR's at which angle of attack is significantly larger than the stall angle. This inaccuracy affects the turbulent viscosity calculations and consequently results in inaccuracies in prediction of the lift and drag forces on the blade.
- **Truncation error:** As it was discussed earlier in this report, a computational solution to the fluid dynamics problem should be conducted by converting Partial Differential Equations (PDE's) to algebraic equations. This conversion should be done by writing the flow parameters in the form of a truncated Taylor expansion series. Dropping of higher

order terms (higher than two in the current simulations), results in a numerical error which is called truncation error. Truncation error is a general part of every CFD solution and can be reduced by using higher order solvers.

- Round-off error: Round –off error is another general error contained in computational solutions to the physical problems. This error is basically the difference between the calculated approximation of a number, stored in the memory of computer and the real mathematical value of that number. There are two types of solvers available in FLUENT, single-precision and double-precision solver. Although single-precision solvers are sufficiently accurate for most of the problems, a double-precision solver was used in the current work to reduce the error imposed to the solution due to the round-off error. Needless to say that double-precision solver needs a larger capacity of the computer’s memory.
- Experimental sources of discrepancy
 - Arm-blade connection: It was mentioned in the previous section that a series of tests were conducted with the blades detached to measure the counter torque generated by the arms. Although this approximation helps to exclude the arms effect on the average torque and efficiency, it still neglects an important part of the physics of the problem. In fact, the flow disturbance generated by the rotation of the arms inside the turbine can affect turbine’s performance significantly. Vorticity shed from the arms results in changes in the magnitude and direction of velocity vector observed by downstream blades. Thus, it can change the torque generated by the downstream blades. This phenomenon was neglected in the numerical simulations and can be an important source of discrepancy between the experimental and numerical results. For the most recent series of experiments at UBC Naval Architecture Lab, the arms profile was changed to a NACA 0012 profile to reduce the counter torque generated by the arms as well as to reduce the flow disturbance and vortex shedding on downstream blades.
 - Drive-terrain response time: As it was observed in the validation section, there is a phase difference between the numerical results and experimental results. Part of this difference is due to the inability of turbulence models to predict the separation accurately. Another important source of this phase shift is caused by the slow response of the motor to the changes in the torque in the experiments resulting in a fluctuating in

RPM. These fluctuations were more pronounced for the cases with higher current velocity and TSR at which the torque magnitude imposed to the motor is relatively large. Figure 6-17 shows the RPM fluctuations for a current velocity of 2 m/s and a TSR of 3.

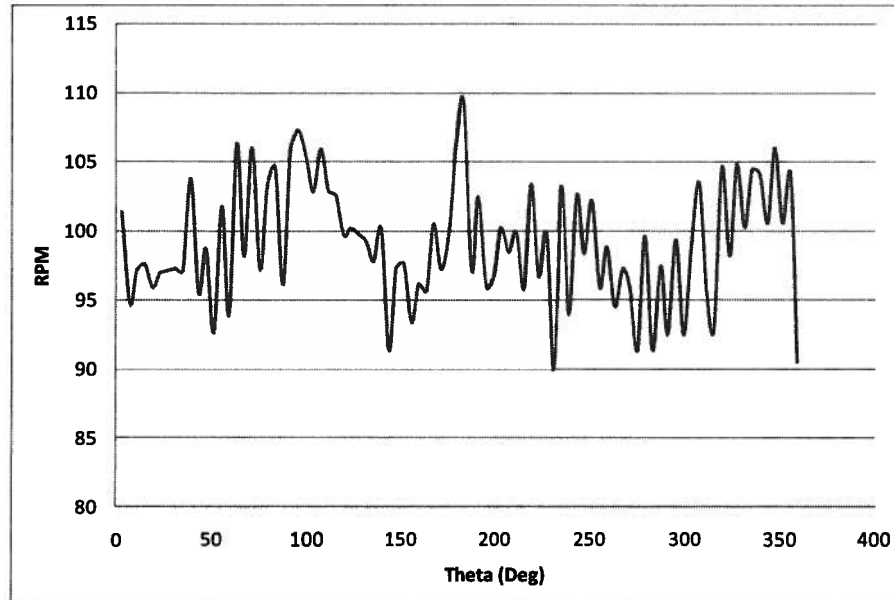


Figure 6-17: RPM fluctuations in experiments

As it can be observed, the RPM ripple is about $\pm 10\%$ of the mean value. This problem affects not only the instantaneous power generated but also can change the physics of the flow field around the blade and consequently the hydrodynamic forces. To address this problem, the drive-terrain was changed in the most recent experiments. The main change was to use a worm-gear instead of the regular gear box to convert the torsion imposed to the motor to an axial force. This change was predicted to minimize the RPM ripple in the experiments.

- Free surface effects: As the turbine is dragged in the tow tank, the free surface of tank is disturbed significantly as shown in Figure 6-18 and Figure 6-19. The free surface boundary can affect the experimental results. The free surface effect can be reduced by mounting the turbine deeper in the tank. However, there is a limit for the turbine depth as it gets close to the towing tank bed. Also a design with a lower system overall drag (such as more stream-lined blades and arms and less 3D effects) can results in reduced free-surface effect on the solution.

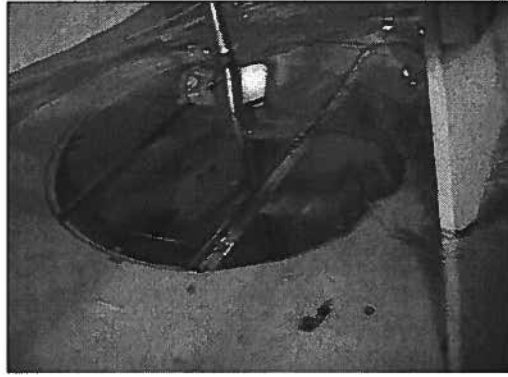


Figure 6-18: Free surface disturbance at lower velocities

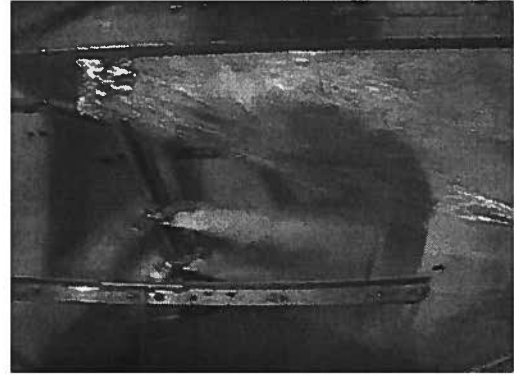


Figure 6-19: Free surface disturbance at higher velocities

- **Averaging Technique:** If the torque generated by the turbine is plotted vs. time or accumulative azimuth angle, it will be observed that the torque curve is not being repeated identically (Figure 6-20). In other words, the peaks and troughs should be theoretically close but is seen that these values are fluctuating about $\pm 10\%$. In the current work, the average power is calculated based on the torque generated over the whole run as opposed to a single cycle.

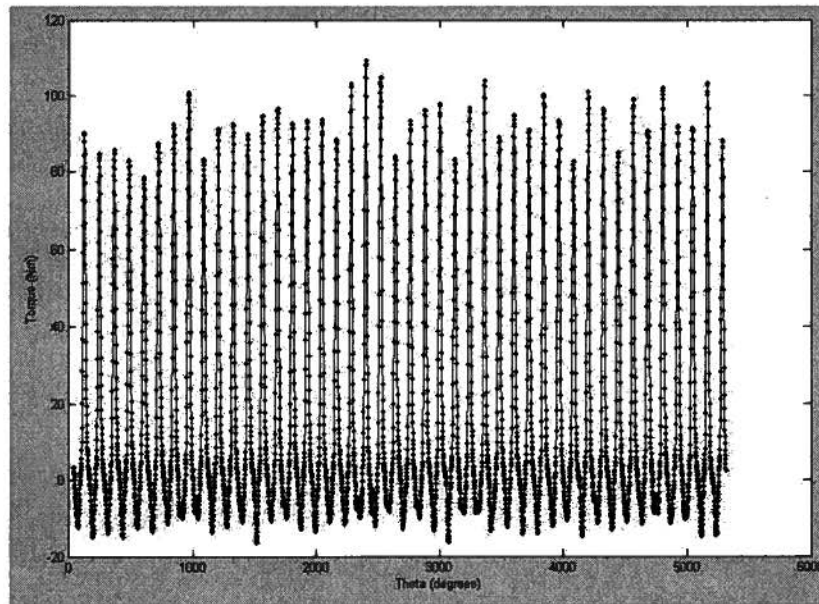


Figure 6-20: Experimental torque variations

- Instrumentation uncertainties and mechanical losses: Similar to every experimental work, there are a few uncertainties and losses in the experimental setup. The more about these issues will be addressed in the Naval Architecture Lab reports on experiments. As a source of discrepancy between the numerical and experimental results, it should be mentioned that some losses such as mechanical losses in the drive-terrain (gear box and motor) and the bearings as well as signal losses exist in the experiments which are not included in the CFD simulation of the turbine. However, it is predicted that these losses are insignificant and do not substantially affect the results accuracy.

All the uncertainties involved with the experiments can be included in the presentation of the results by using error bars for the experimental result. The methodology used for obtaining the range of error for the experiments is beyond the scope of the current work. However, in order to ensure that the experimental and numerical results are in an acceptable level of agreement, a comparison was also made between the numerical results and experimental results with error bars as shown in Figure 6-21.

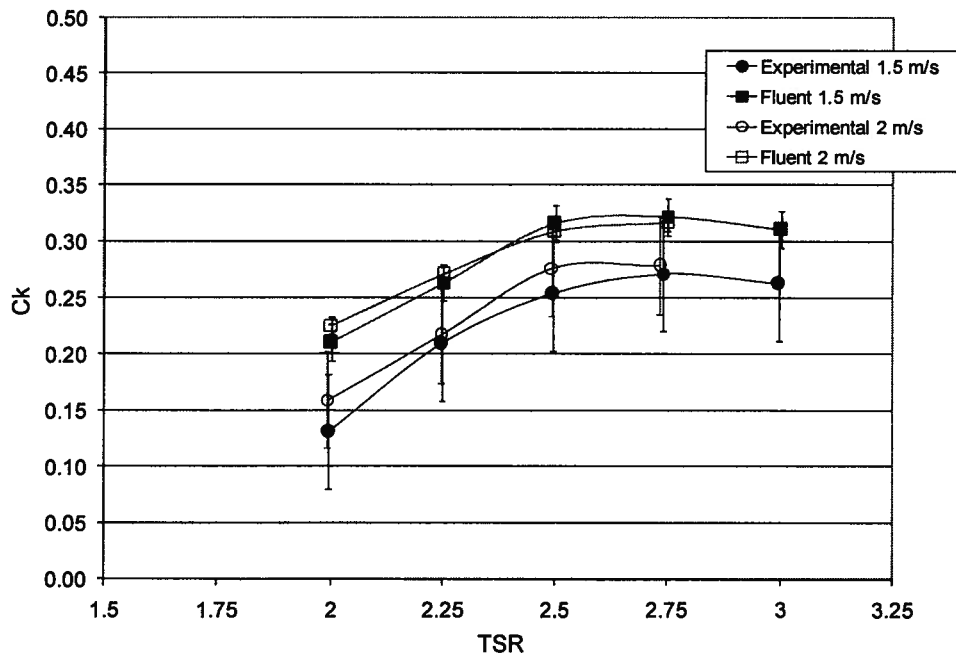


Figure 6-21: Comparison of free-stream results from FLUENT and experiments including the error bars

7. Duct Shape Optimization

The preceding chapters focused on validation of free-stream and ducted turbine simulations using experimentally obtained data in a towing tank. The accuracy of the simulations showed to be adequate to justify proceeding onto the next phase of the project. This phase focuses on modifying the duct geometry to increase the performance of the turbine.

7.1 Preliminary Approach

Numerous duct shapes were examined to understand the physics of the flow inside a duct and to understand whether they can be used to improve the power generated by the turbine. The torque curve over a cycle of rotation was used as a guideline to improve the performance in the regions where the torque generated by the turbine was relatively low.

Figure 7-1 shows a typical torque curve for one blade in a 3-blade configuration.

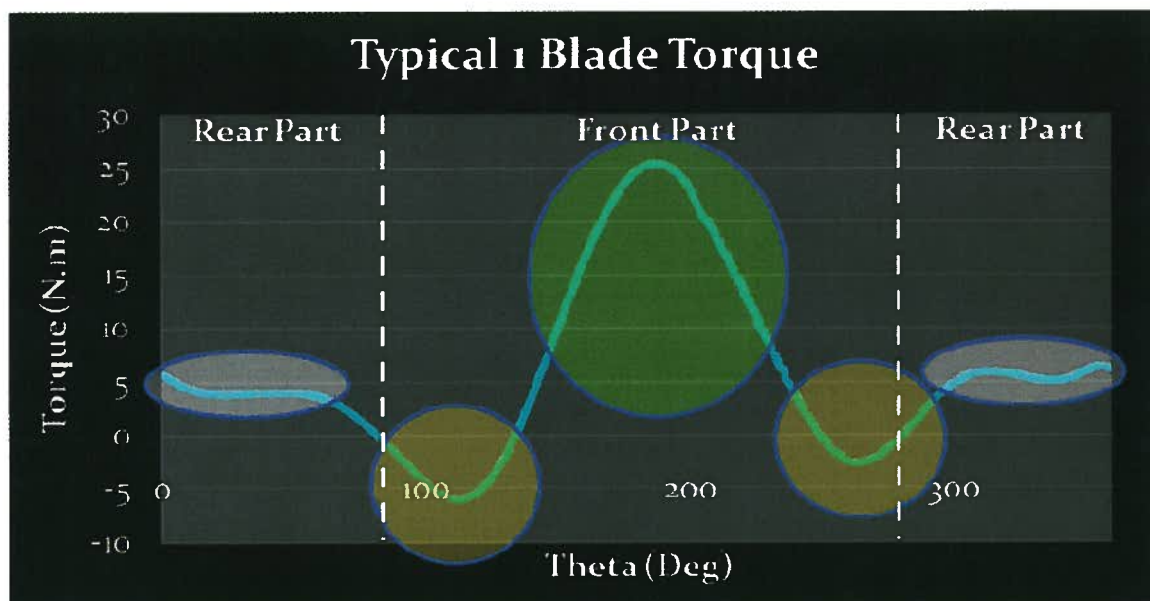


Figure 7-1: Single-blade torque curve over a cycle in the presence of the other two blades

A closer look at this curve reveals that the torque curve can be divided into three main regions: grey regions, orange regions, and green region. The grey regions are expanded through azimuth angles between 0 to 90 degrees and 270 to 360 degrees. This region corresponds to the downstream portion of the blade rotation. The orange regions are the regions at which transition between positive torque and negative torque occurs. In these regions, the angle of attack changes from a positive value to a negative

value and vice versa. Hence, the angle of attack would be zero at some point during this transition. In these transition regions, there exists a point at which the torque is negative. This occurs when the blade passes through an angle of attack of zero and the only torque generated by the turbine would be a counter torque according to Equation 2-3. The green region is where the torque magnitude reaches its maximum. At this point, the angle of attack is large and close to the stall angle. It should be mentioned that at low TSR's (TSR's below 2), the maximum angle of attack exceeds the stall angle.

The strategy chosen to increase the power generated by the turbine was to increase the torque magnitude in the grey and orange regions while keeping the high torque of green region.

As it can be seen in Figure 3-1, the narrowest part of the duct is exactly at the mid-section. Thus, in order to satisfy the continuity equation for an incompressible flow, the maximum velocity would occur at mid-section of the duct. As it was shown in Figure 7-1, the mid-section of the duct is where the maximum negative torque is produced. Hence, by accelerating the flow in the middle part of the duct, the drag force (which is proportional to the velocity square) and the counter torque would increase significantly. Also, the grey regions can be improved by reenergizing the flow in the rear part of turbine.

To be able to compare different ducts performances, a number of geometric limitations should be considered as the design constraints. For example, if the duct size is increased, the flow velocity inside the duct is increased as a result of larger inlet area. Consequently, the available energy to the turbine would be different from that of the UBC duct and the comparison would not be valid. Thus, a contraction ratio is defined by Equation 7-1. For all the ducts tested, the contraction ratio was assumed to be constant (except for double-duct cases) to enable a valid comparison between different cases.

$$CR = \frac{A_{min}}{A_{max}} \quad \text{Equation 7-1}$$

In order to tackle the above problems, a set of simulations were conducted for a duct shape shown in Figure 7-2. This duct shape is similar to the UBC duct with a concave hollow shape in the mid-section. The modified duct is referred to as UBC's 1st modification (mod 1 to be brief).

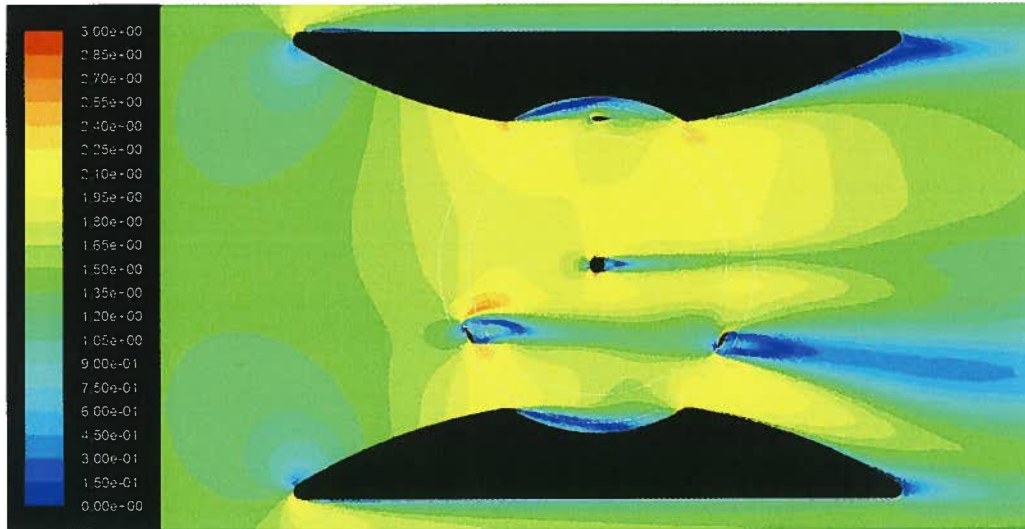


Figure 7-2: UBC duct with a hollow in the middle (mod 1)

As observed from the velocity magnitude contours (Figure 7-2), the throat is transferred to the high torque region at the front to keep or increase the flow velocity hitting the upstream blades. Also, a secondary throat at the rear part of turbine reenergizes the flow to increase the torque generated by downstream blades. Also, an attempt was made to widen the duct sectional area in the mid section to decelerate the flow in the counter torque zones.

In addition to the above duct, two other ducts (2nd and 3rd modifications of the UBC duct, referred to as mod 2 and mod 3) with the same contraction ratio and throat locations but with different inner edges were examined to understand the effect of the flow redirection on the torque curve. Also, it was predicted that these geometric changes slightly affect the mass flow rate inside the duct. This would be due to the change of location of the stagnation point at the mouth of the duct.

Figure 7-3 shows the second duct geometry examined with straight line edges connecting the duct tips to the concave hollow in the middle. This duct shape provides different angles for the upstream blades close to the duct. Figure 7-4 shows the mod 3 duct with a concave connecting edge. The same concept was pursued for this duct as well.

It can be understood from the velocity contour figures that the duct with convex connecting edges (Figure 7-2) has the widest high velocity region while the third duct with concave connecting edges (Figure 7-4) has a limited high velocity region. It is seen that for the latter, the separation zone is widely expanded at the downstream of the duct resulting in deceleration of the central parts of the flow.

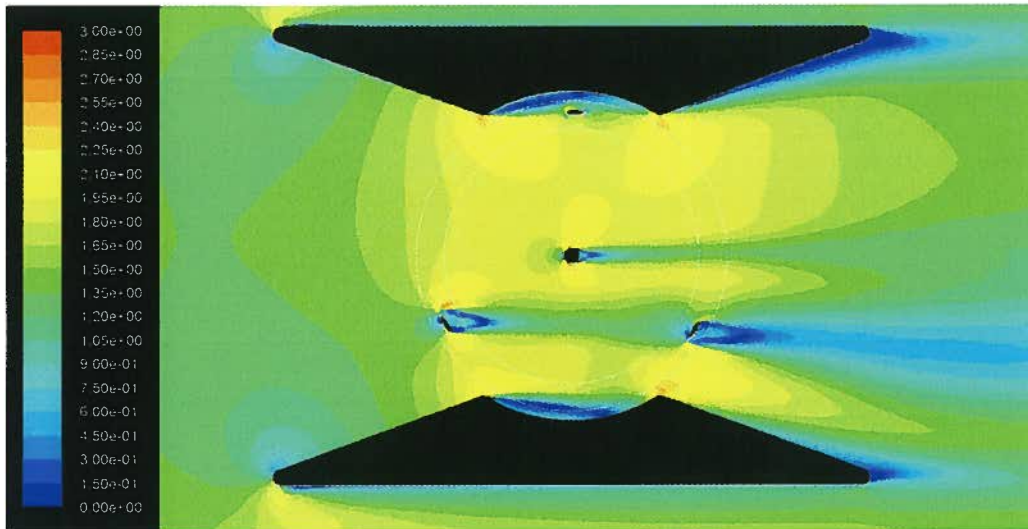


Figure 7-3: A duct with straight line connecting edges (mod 2)

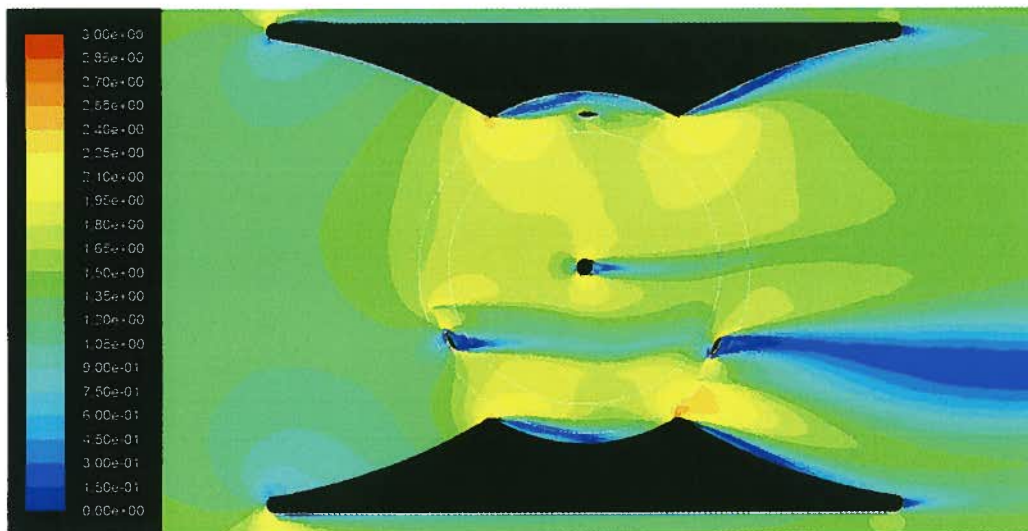


Figure 7-4: A duct with concave connecting edges (mod 3)

In order to understand the effect of the flow redirection on the torque curve it is necessary to run the unsteady simulations and observe the wake development when the blades are rotating. The simulations were conducted for a constant velocity of 1.5 m/s and TSR's ranging between 2.00 and 3.00. The torque curves and the efficiency curves were then compared to understand the effect of the duct geometry on the turbine's performance. All the grid specifications and solver properties used for these simulations are identical to UBC's duct simulations. The comparison of efficiencies obtained from different duct shapes and also the UBC duct is presented in Figure 7-5.

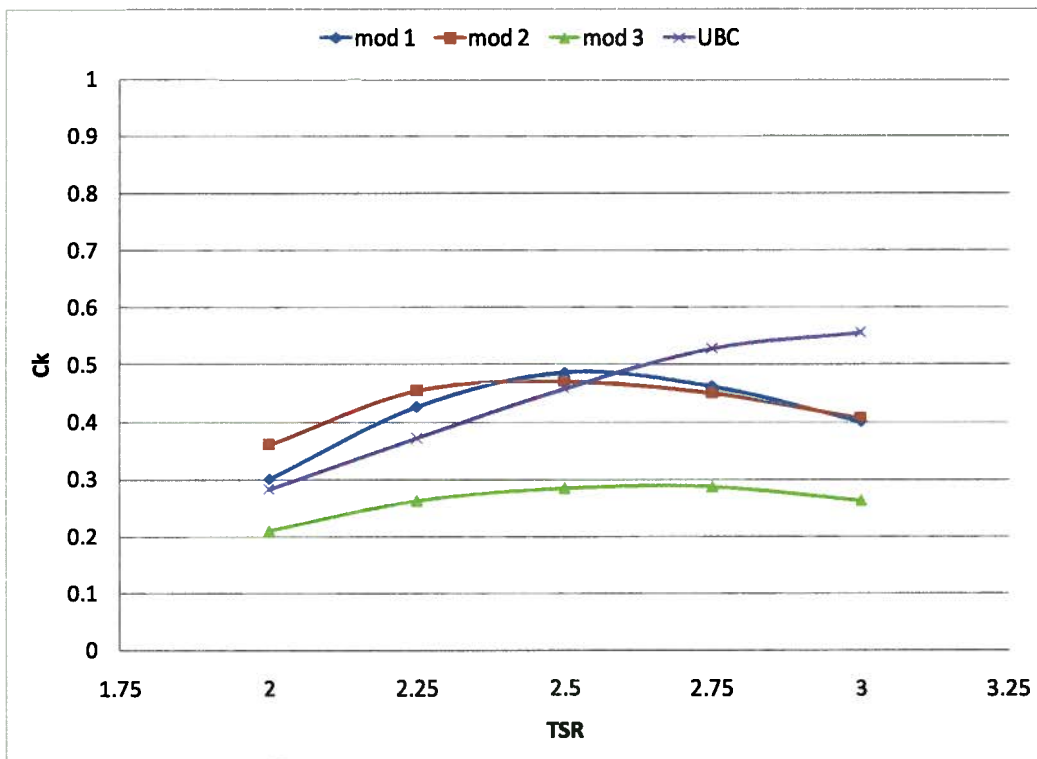


Figure 7-5: Efficiency comparison of different modifications of UBC duct

The following conclusions can be extracted from the above figure:

- 3rd modification of the UBC duct performs even worse than a free-stream turbine. Its efficiency is lower than the UBC duct or any other modifications at all TSR's. However, the power curve is flat which means that the turbine can work in the design conditions over a vast range of RPM's and current velocities.

- 1st and 2nd modifications' efficiencies are higher than the UBC duct at low TSR's while the efficiency reaches its maximum at TSR of 2.5. At higher TSR's they both have a lower efficiency compare to the UBC duct. Also, both 1st and 2nd modifications have a flatter efficiency curve than the UBC duct. That means that their performance is less sensitive to the changes in RPM and current velocities which results in changes in TSR.
- It is observed that 2nd modification has a higher efficiency than the 1st modification at lower TSR's (2.00 and 2.25). On the other hand, 1st modification has a slightly higher efficiency at higher TSR's.

The selection of each duct depends on the design conditions and restrictions. For example, the turbine needs to work at low TSR's as higher TSR's produce relatively high levels of noise having negative environmental effects. The structural and mechanical design restrictions are another constraint to the duct design process. The cost of the duct manufacturing is another important parameter that should be considered in the duct selection process. These restrictions will be discussed further in Chapter 8. The comparison of the three-blade and single-blade torque curves at different TSR's is presented in Figure 7-6 to Figure 7-15.

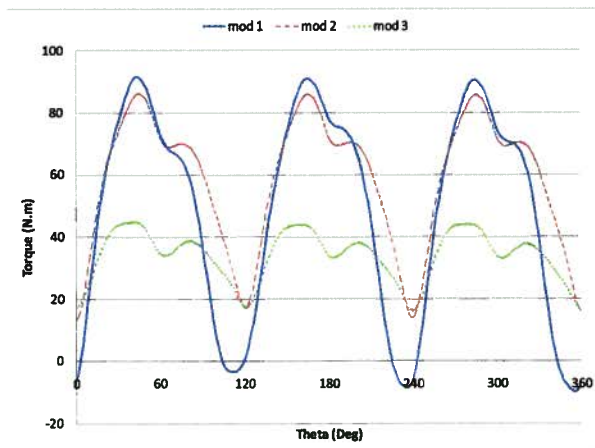


Figure 7-6: 3-Blade torque comparison of three UBC duct modifications (V=1.5 m/s ; TSR=2.00)

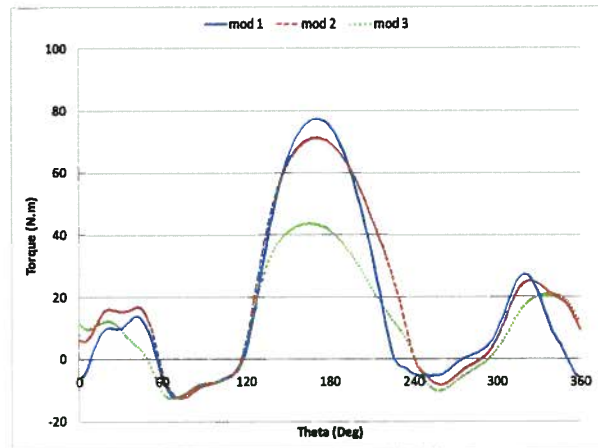


Figure 7-7: Single-Blade torque comparison of three UBC duct modifications (V=1.5 m/s ; TSR=2.00)

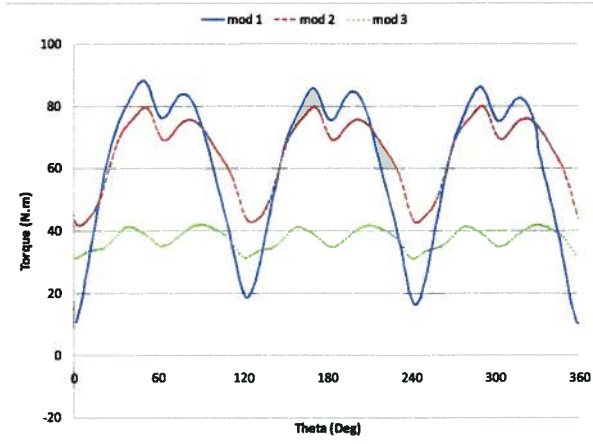


Figure 7-8: 3-Blade torque comparison of three UBC duct modifications ($V=1.5$ m/s ; $TSR=2.25$)

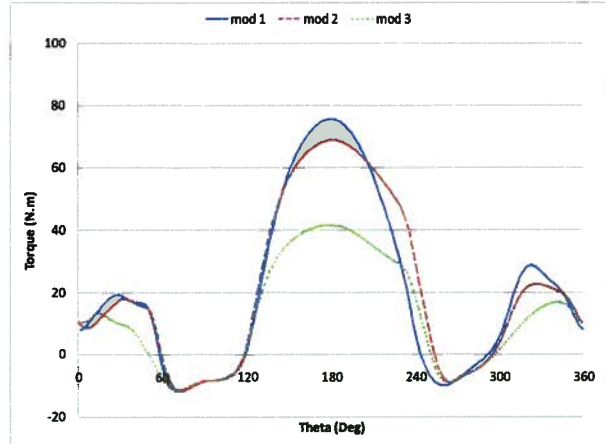


Figure 7-9: Single-Blade torque comparison of three UBC duct modifications ($V=1.5$ m/s ; $TSR=2.25$)

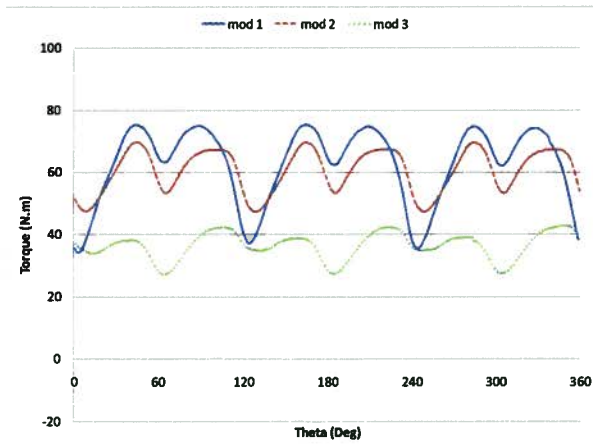


Figure 7-10: 3-Blade torque comparison of three UBC duct modifications ($V=1.5$ m/s ; $TSR=2.50$)

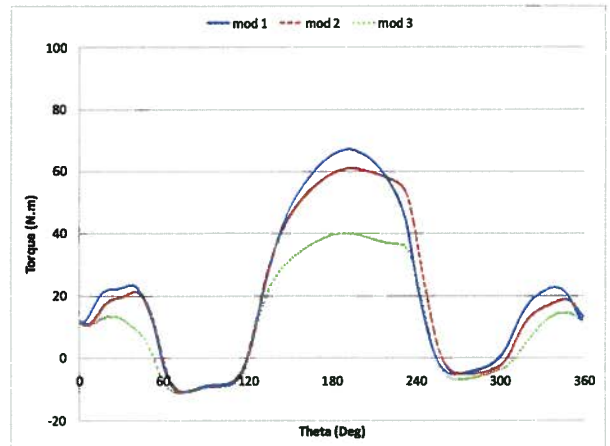


Figure 7-11: Single-Blade torque comparison of three UBC duct modifications ($V=1.5$ m/s ; $TSR=2.50$)

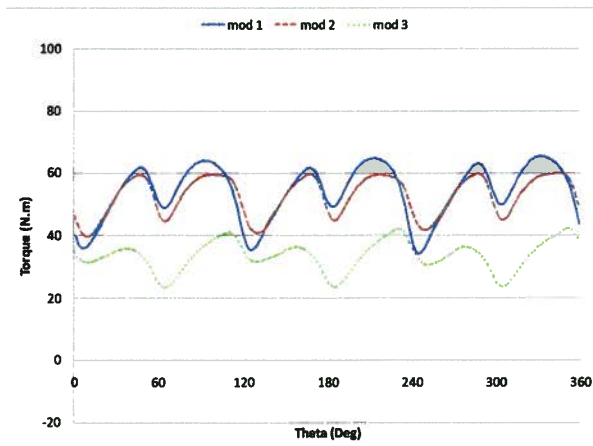


Figure 7-12: 3-Blade torque comparison of three UBC duct modifications ($V=1.5$ m/s ; $TSR=2.75$)

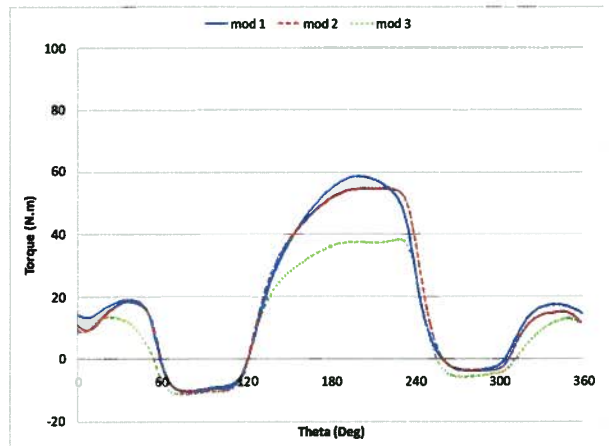


Figure 7-13: Single-Blade torque comparison of three UBC duct modifications ($V=1.5$ m/s ; $TSR=2.75$)

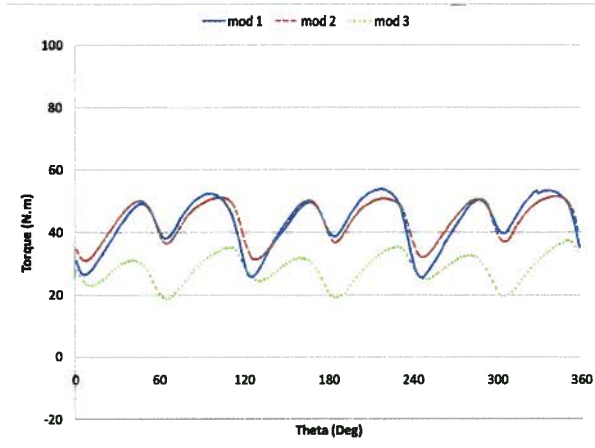


Figure 7-14: 3-Blade torque comparison of three UBC duct modifications ($V=1.5$ m/s ; $TSR=3.00$)

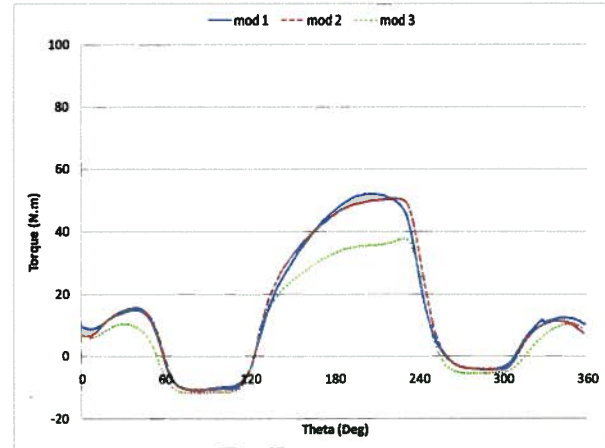


Figure 7-15: Single-Blade torque comparison of three UBC duct modifications ($V=1.5$ m/s ; $TSR=3.00$)

Figure 7-16 shows the typical single-blade torque curve for the UBC duct and its three modifications. It is shown that the UBC duct curve is sharper at its maximum while from mod 1 to mod 3, the maximum torque decreases and the positive torque curve region widens.

According to Figure 7-16, the torque generated downstream is slightly increased which can be the effect of flow-reenergization due to the transfer of the duct throat to the rear part. Yet, it is observed that throat designed near the mouth of the duct, adds to the blockage of the duct and prevents the flow velocity to increase upstream. As a result, the flow velocity and consequently, the maximum torque is lower in the presence of the throat in the front.

Another noticeable phenomenon in the results is the widened torque curve as a result of flow redirection. Changing the place of the throat results in changes in the angle of attack in the regions that the torque generated is low due to low local angle of attack. However, it is observed that the effect of flow redirection is not very significant. Also, it seems that the 2nd modification has the widest torque curve as a result of the flow redirection. The 1st and 3rd modifications however, have a narrower peak and their width is about the same as the UBC duct.

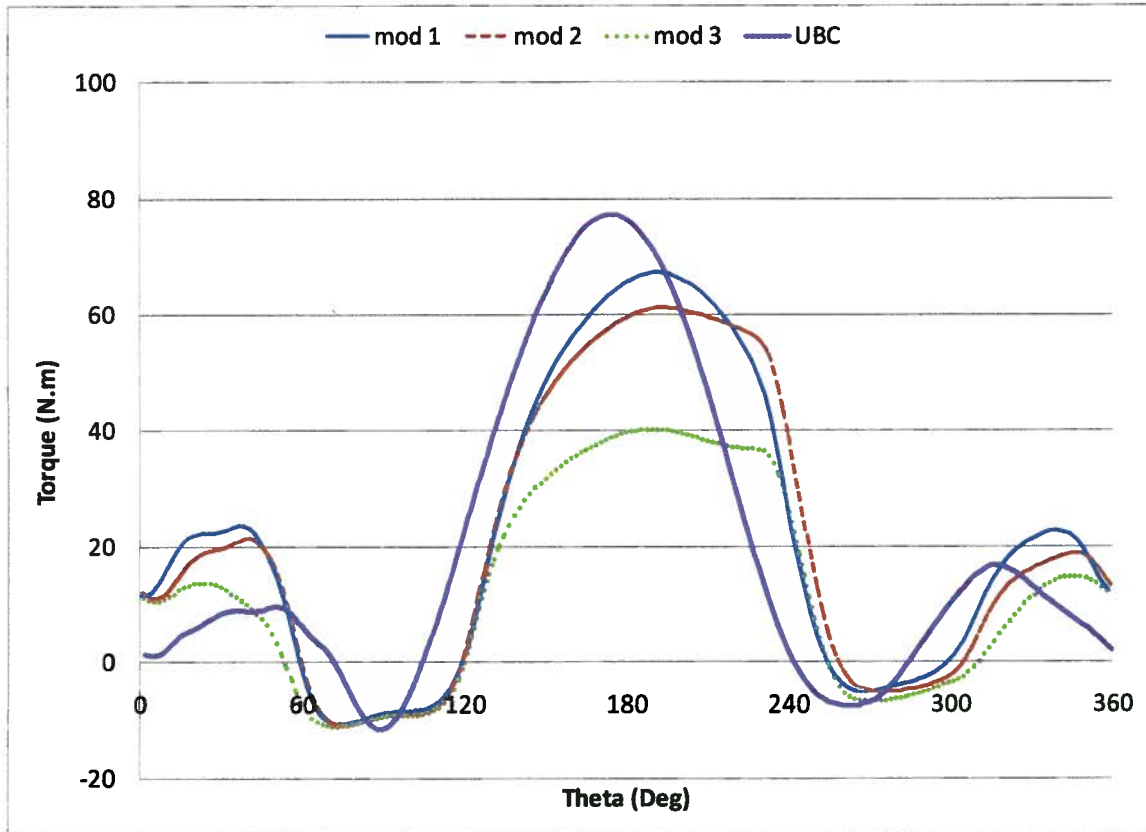


Figure 7-16: Typical single-blade torque comparison for UBC duct and its modifications ($V=1.5$ m/s ; $TSR=2.50$)

7.2 Steady-State Study of Different Ducts

7.2.1 Methodology

In order to better understand the effect of blockage on the torque curve and to maximize the mass flow rate inside the duct, a set of steady-state simulations were conducted for different duct shapes. The methodology used for this phase of study was to examine different duct shapes with the same contraction ratio and inlet area as the UBC duct. This means that a design box with constant boundaries was defined and the duct shape could change inside that box as long as the duct edges touch the box boundaries (to meet the constant contraction ratio requirements). The box concept with constant contraction ratio (A_{min} / A_{max}) is shown in Figure 7-7.

As it will be described later in this chapter, in some cases the constant contraction ratio assumption and the design box approach were not considered as the design constraints. This was the case to study the concept of a double-duct design.

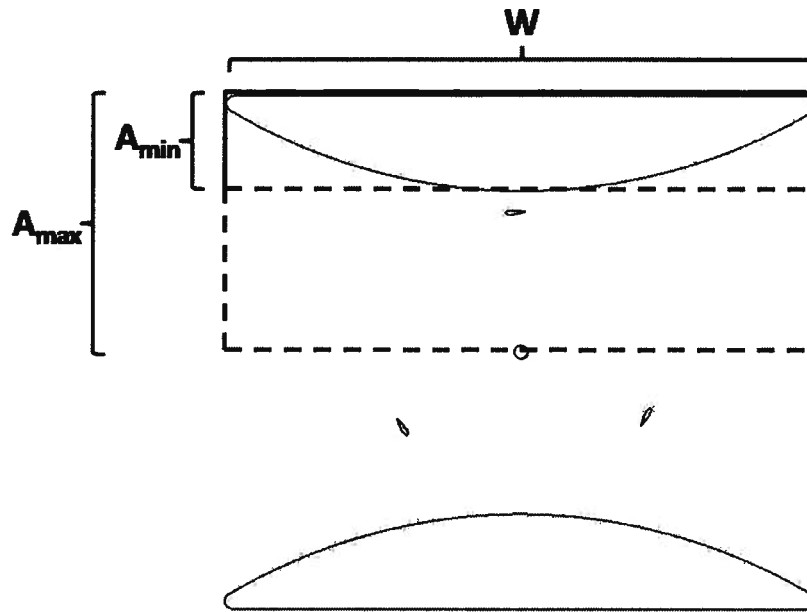


Figure 7-17: Design box concept

The ducts can be categorized into two main types:

- Single-compartment ducts
- Multiple-compartment ducts

For the first category of the ducts, similar to the UBC duct, the duct consists of two large scale parts with no add-ons. In other words, like the first three modifications of the UBC duct, the UBC duct was further modified to achieve the desired flow field inside the duct. For multiple-compartment ducts, however, an attempt was made to obtain the desired conditions by using some additional components inside the duct such as vanes and secondary ducts. The scale of the add-ons is usually significantly smaller than the main duct and in some cases they are used for fine-tuning of the design.

The ducts were named by number and the initials of the researchers who proposed the design (Yasser Nabavi and Voytek Klaptocz). A few parameters were considered for the duct selection process as shown in Figure 7-18. These parameters include the mass flow rate inside the duct, the velocity at the duct entrance (mouth), velocity at maximum torque location (that corresponds to an azimuth angle of

180), and the velocity at the minimum duct area (throat). Also, the average velocity over the blade's circular path was recorded as well as the distribution of the velocity angle over the blade's path.

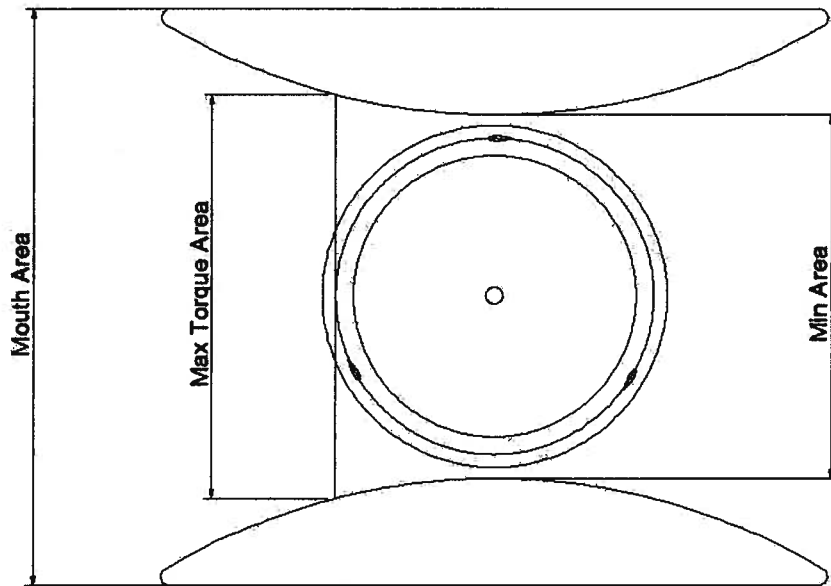


Figure 7-18: Measured flow parameters for comparison of different ducts

Mass flow rate and average velocity at the duct entrance are parameters that represent the effect of blockage on the upstream flow. These two parameters also quantify the level of kinetic energy entrained into the duct. As the available kinetic energy is proportional to the velocity cubed, a small increase in velocity inside the duct can result in significant changes in the power generated by the turbine. Theoretically, in order to increase the mass entrained into the duct area it is necessary to move the frontal stagnation point on the duct towards the outside of the duct. In fact, the distance between the stagnation point on the upper duct and the stagnation point on the lower duct determines the area through which the current fluxes.

Moreover, average velocity at the maximum torque area (the area at which the maximum torque is predicted to occur) shows that kinetic energy available to the upstream blades at highest torque generation condition. The higher velocity at maximum torque area shows a higher maximum torque peak. However, there might be some restrictions for increasing the velocity in this region as increased velocity in this area can result in larger torque ripple and mechanical design problems. The flow at the

throat also shows the highest velocity inside the duct and can be used as a parameter for comparison of different duct configurations.

In order to simplify the comparison, the velocity contours for each duct shape will be displayed and the above-mentioned flow parameters will be compared.

7.2.2 Grid and Solver Specifications

A few changes were made to the modeling procedure compared to what was explained in Chapters 2 and 3. For the simulations in this phase of the project, a two-dimensional, segregated steady-state solver was used with a 2nd order upwind discretization scheme for momentum and turbulence equations. As in the case of transient simulations, a Spalart-Allmaras turbulence model was used in conjunction with the SIMPLE algorithm for pressure-velocity coupling. Under relaxation factors were rearranged to accelerate the convergence. Similar to the previous cases, a combination of structured and untreated grid was used to discretize the domain. A structured grid was used in near-wall regions such as duct walls and vanes, where an accurate solution of the boundary layer is needed. All the simulations in this section were conducted in the absence of the blades in order to better understand the effect of the duct geometry on the behaviour of the flow field inside the duct.

In order to precisely calculate the average velocities at different duct cross sections (such as the mouth and the throat), a rake with 100 nodes was defined across that specific cross sectional area. The velocity was measured on each node and the average was calculated accordingly. It should be mentioned that the same boundary conditions are used for this set of simulations and the inlet velocity was set to 1.5 m/s for all the ducts examined.

7.2.3 Examined Duct Configurations

In this section, the velocity contours for the examined ducts will be presented. The velocity contours show the flow field inside and outside of the duct and facilitate the prediction of the turbine performance in the presence of any duct shape. For the ducts that show an acceptable performance, the velocity vectors were displayed to further study the flow redirection and its effect on the torque generated by the blades.

Figure 7-19 shows the velocity contours for the UBC duct as a reference for comparison to the various duct studies included in this research. The contour levels were identically plotted for all ducts so as to simplify the comparison.

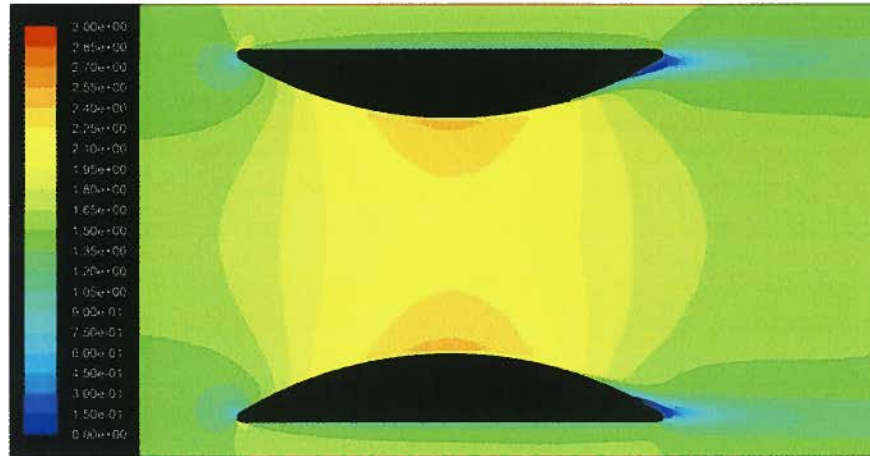


Figure 7-19: Velocity contours for the UBC duct as the reference

Below, different categories of duct shape simulated will be presented and the specification of each duct will be analyzed.

Category 1: Guiding Vane concept

Duct names: YV1, YV2, and YV3

Goal: To redirect the flow without any reduction in the kinetic energy available to the turbine

Type: Multiple-compartment duct

In the first set of simulated ducts, an attempt was made to maintain the flow kinetic energy and redirect the flow in the regions where an increased angle of attack could generate a larger torque. Figure 7-20 to Figure 7-22 show a guide vane configuration that was used for flow redirection. A NACA 4409 airfoil with a chord length of 25 cm was used at different angles of attack and the maximum flow deflection was recorded. Also, the average velocity magnitude on the blades' path was measured to understand the effect of vorticity shed from the vanes on the kinetic energy delivered to the blades.

Table 7-1 summarises the results obtained for this set of ducts and the comparison with the default UBC duct. As it is presented in the table, YV1 has guide vanes with 15 degrees angle of attack, YV2 has the same vane geometry but set at an angle of attack of 5 degrees. YV3 is identical to YV2 but the trailing edge of the vanes was rounded to reduce flow separation for the rear vanes.

As it is observed in Figure 7-20 and Table 7-1, in duct YV1 an effort was made to deflect the upstream flow, but the angle of attack was found to be large as the separation is intense and the blades will be placed in the wake of the vanes. Also, excessive angle of attack increases the blockage and causes a reduction in the mass flow entrained into the turbine area. As the vane angle of attack is decreased in

YV2 and YV3, it is seen that the mass flow rate and velocity average on the blades' path increase, but the deflection mechanism is not effective as YV1. Also, it was understood that rounding the vanes' trailing edges has no significant effect on the average velocity and deflection angle. It will be described later in this chapter that a set of unsteady simulation was conducted for YV3 to investigate the effectiveness of this configuration.

Table 7-1: Duct with guiding vane configuration results

Duct Name	Vane Angle (Deg)	Mass flow rate (kg/s)	Maximum Deflection Angle (Deg)	Average Velocity on blades' path (m/s)
UBC	No vane	2392	5.30	2.189
YV1	15	2177	8.51	1.973
YV2	5	2258	5.75	2.085
YV3	5	2261	5.75	2.090

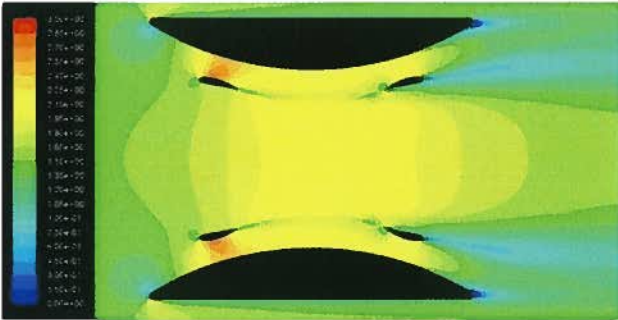


Figure 7-20: YV1 (Guiding vanes at 15 degrees AOA)

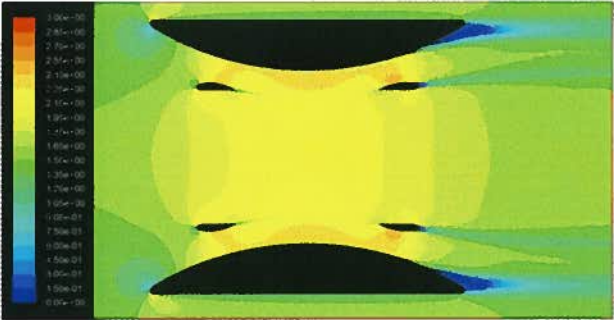


Figure 7-21: YV2 (Guiding vanes at 5 degrees AOA)

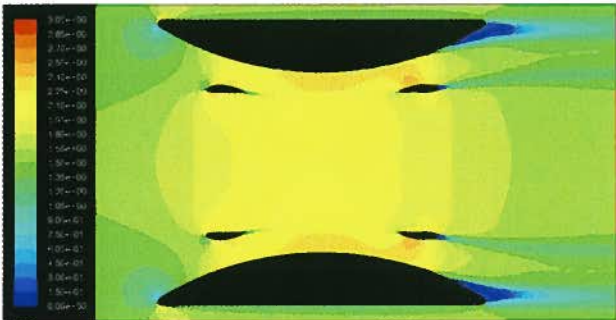


Figure 7-22: YV3 (Guiding vanes at 5 degrees angle of attack and with a rounded trailing edge)

Figure 7-23 also shows the comparison of velocity angle distribution over the blades' path for YV1, YV2 and YV3 and the UBC duct. This figure shows that although YV1 is more effective than any other

configuration upstream, its performance downstream is unacceptable. Also, it appears that YV2 and YV3 do not significantly change the angle of attack upstream but perform slightly better than the UBC duct in the downstream region.

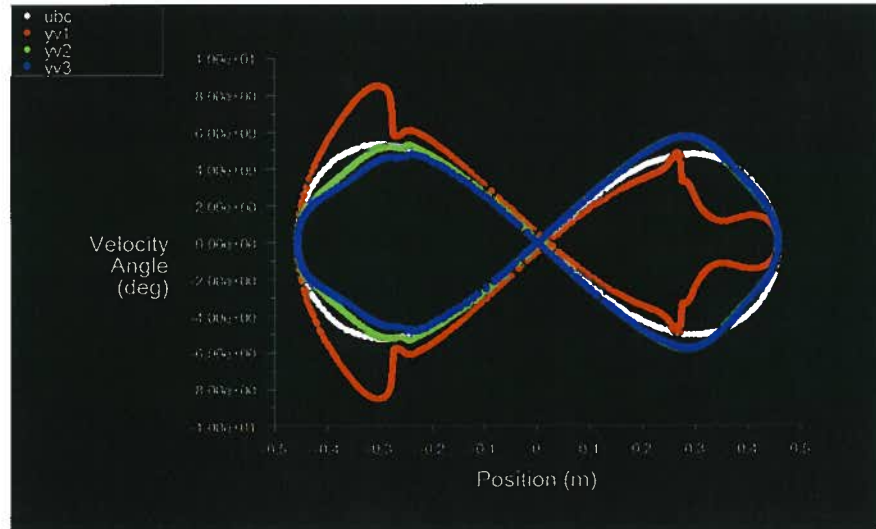


Figure 7-23: Velocity angle distribution for guiding vane configurations

Category 2: Modified UBC Duct

Duct names: YV4, YV5, YV6, YV7, and YV8

Goal: To increase the mass flow rate and the kinetic energy available to the turbine

Type: Single-compartment duct

In this set of simulations, the UBC duct configuration was modified while keeping a constant contraction ratio (limited to box concept). The results obtained for this set of ducts are presented in Table 7-2 and compared to the UBC duct.

Table 7-2: UBC duct modifications results

Duct Name	Mass flow rate (kg/s)	Maximum Deflection Angle (Deg)	Average Velocity on blades' path (m/s)
UBC	2392	5.30	2.189
YV4	2173	3.05	2.062
YV5	2366	10.35	2.165
YV6	2236	5.26	2.082
YV7	1873	5.21	1.732
YV8	1773	3.60	1.690

As shown in Table 7-2, the only duct with acceptable performance is YV5. It appears that the incoming flow is properly redirected in this case and the kinetic energy delivered to the turbine's blades is approximately the same as the UBC duct.

YV4 was supposed to keep the same kinetic energy as UBC delivered to the upstream blades while decreasing the mid-section velocity where counter torque is generated. It is observed that due to a slightly larger area compared to the UBC duct, as well as sudden changes in the duct curvature in the flat regions, the velocity magnitude is significantly decreased.

Duct YV5 was successful in keeping the same velocity as UBC and flow redirection. However, the separation at the rear part of the duct prevents the flow acceleration and an increase in the mass flow rate entrained inside of the turbine area.

Duct YV6 was designed to investigate the outer side of the duct on the mass flow rate and velocity field inside the turbine area. This configuration does not work properly as the duct acts as a deformed, low quality airfoil.

A new concept was attempted for duct YV7. The purpose of placing an injection port inside the duct was to deliver more mass flow to the blades and hence increase the available kinetic energy. As shown in Figure 7-27, the current configuration did not work properly. This concept was investigated further and is described later in this chapter.

As duct YV6 did not function properly, a new geometry was designed in order to understand the effect of having a pair of large airfoils in place of the ducts. Two NACA 4409 airfoils were selected with a chord length equal to the length of the UBC duct. However, the contraction ratio could not be kept constant and was lowered by more than 5%. The velocity contours shown in Figure 7-28 show that the concept has a number of major problems. One of the main problems with this concept is that it is not a symmetric design. Thus, when the tidal currents change direction, the duct does not perform properly anymore. Also, these geometries are very difficult to build, can result in increased cost and cannot lead to a viable design. In addition, the hydrodynamic performance is lower than the UBC duct due to a lower contraction ratio and expansion of shear layer in the wake of the duct. However, using proper optimization tools and a more detailed study on the airfoil that should be selected for this purpose, more research is still needed to be conducted on this concept.

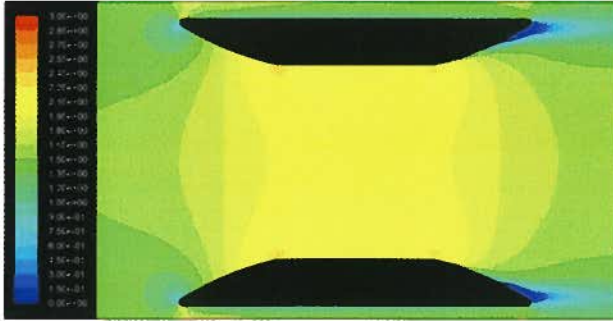


Figure 7-24: YV4 velocity contours

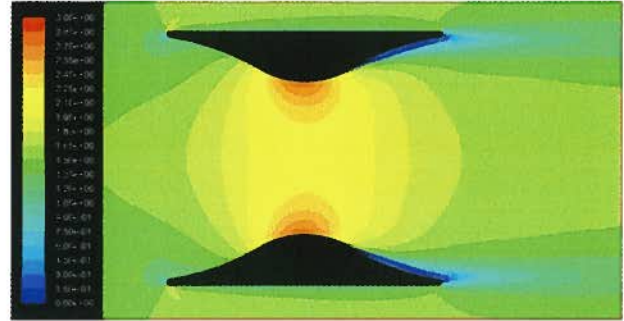


Figure 7-25: YV5 velocity contours

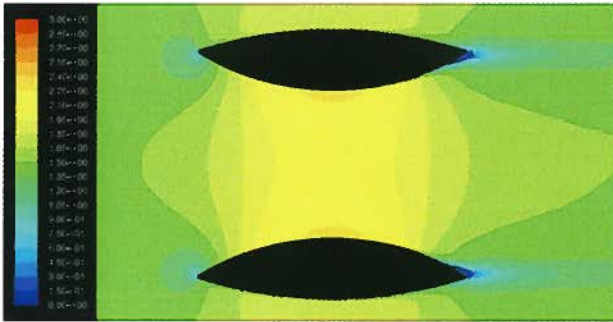


Figure 7-26: YV6 velocity contours

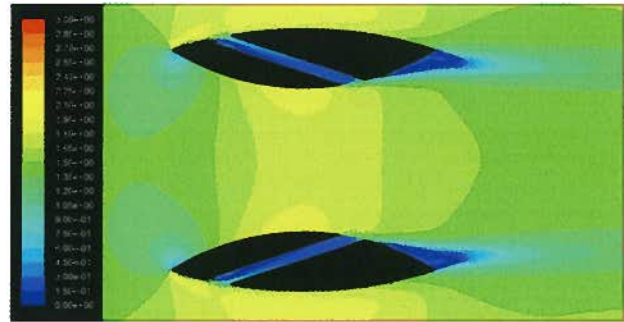


Figure 7-27: YV7 velocity contours

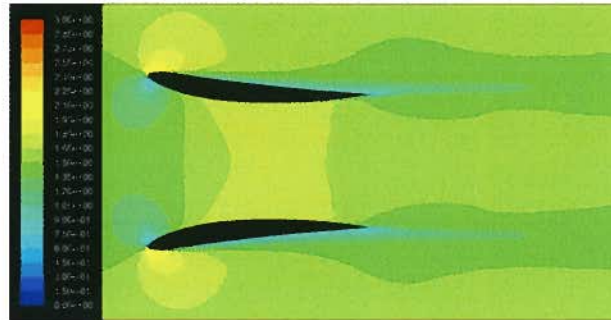


Figure 7-28: YV8 velocity contours

As shown in Figure 7-29, YV5 is the only duct with a potential to change the angle of attack seen by the blades. The deflection angle of the flow in other designs is not appropriate and is lower than the UBC duct. According to Figure 7-29, YV7 and YV8 have a decreased angle of attack in the downstream region and the torque generated in this region is predicted to be smaller than the UBC duct.

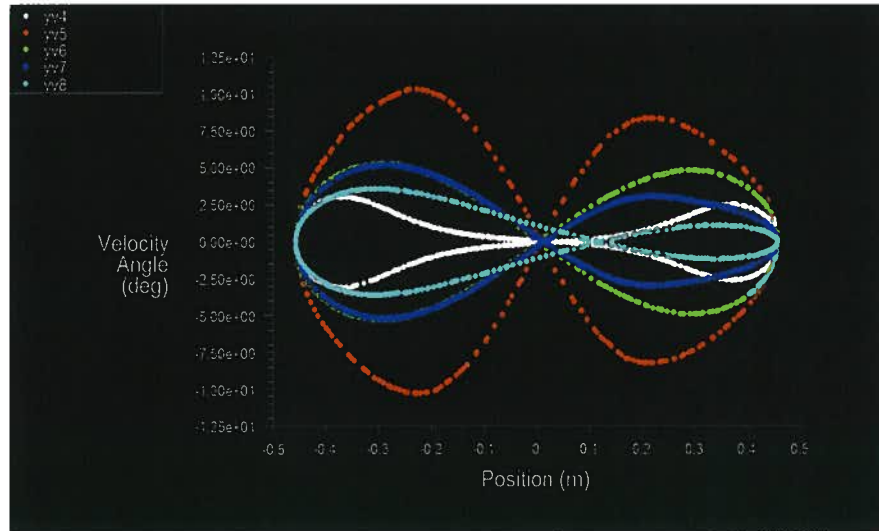


Figure 7-29: Velocity angle distribution for UBC duct modifications

Category 3: Bump Concept

Duct names: YV9, YV10, YV11, YV12, YV13, YV14, YV15, YV16, YV17, YV18, YV19, and YV20

Goal: To shift the location of maximum velocity and reenergize the flow at downstream

Type: Single-compartment and Multiple-compartment ducts

As previously shown in Figure 7-1, a counter torque is generated for a blade at azimuth angles of 90 and 270 degrees where the angle of attack is theoretically zero. Also, at these angles, the velocity magnitude is at a maximum when the UBC duct is used since the throat is placed in the mid section of the duct. An attempt was made to maximize the torque generated by the blades through transferring the throat to a section where a positive torque is generated. That was the main intention for implementing 1st, 2nd, and 3rd modifications on the UBC duct. It was observed, however, that the flow separation at the throat and the vorticity shed from the duct throat decelerates the flow and reduces the kinetic energy available to the turbine. The bump concept was originally developed to address the separation problem of the UBC duct modifications while keeping the throat transferred to a torque-generating region at angles of about 0 and 180 degrees. Figure 7-45 to Figure 7-56 show the concepts designed to achieve these goals. All examined configurations are multiple-compartment ducts except for YV9. Table 7-3 presents the results obtained for this category of ducts.

Table 7-3: Bump configurations results

Duct Name	Mass flow rate (kg/s)	Maximum Deflection Angle (Deg)	Average Velocity on blades' path (m/s)
UBC	2392	5.30	2.189
YV9	2227	4.53	2.123
YV10	2503	9.70	2.217
YV11	2332	9.40	2.207
YV12	2369	8.09	2.273
YV13	2184	7.97	2.148
YV14	2268	10.64	2.176
YV15	2170	15.35	2.153
YV16	2118	13.44	2.096
YV17	2241	9.36	2.177
YV18	2311	11.09	2.291
YV19	2318	6.51	2.185
YV20	2387	17.19	2.300

Comparing the velocity contours of duct YV9 with the UBC duct shows that the local maximum velocity is shifted desirably but the average velocity magnitude, the entrained mass flow rate, and hence the power available are decreased due to the separation at the throat and the increased blockage due to the existence of the bump. It was observed, however, that separation is considerably less severe than the UBC duct modifications because the flow is expanded with a smaller positive pressure gradient downstream of the bumps. Also, it was seen that this duct was not effective in deflecting the upstream flow and the maximum deflection angle was lower than the UBC duct.

Duct YV10 is basically the UBC duct with added bumps at the mid-section. The bumps were designed to be positioned 1 inch away from the main duct for all the simulations except duct YV21. The simulations were conducted to observe the effect of the bumps on the entrained mass flow rate and the velocity angle distribution. The results show that the mass flow rate is increased approximately 5% due to the existence of the bumps. Figure 7-30 and Figure 7-31 show a comparison of the velocity magnitude and velocity angle distribution over the blades' path. As shown in these figures, the velocity distribution curve is sharper for YV10 compared to the UBC duct and the peak point is located at the mid-section

where counter-torque is produced. On the other hand, it is seen that the flow is properly redirected and extra power can be extracted due to an increased angle of attack, especially between azimuth angles of 10 and 50 degrees where the difference in the velocity angle between the two ducts is noticeable. It should be noted that an excessive flow redirection can cause the blades to stall and decrease the generated power. Further fine-tuning might be necessary to obtain the ideal conditions.

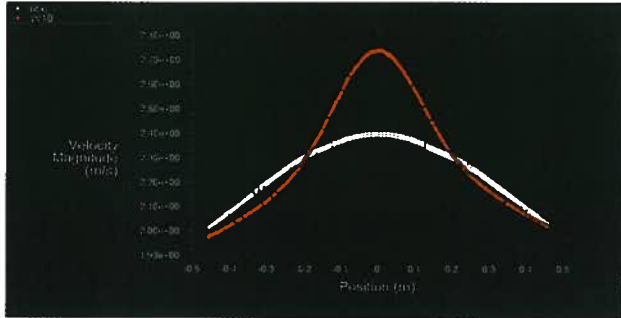


Figure 7-30: Comparison of velocity magnitude distribution over the blades' path for UBC and YV10 ducts

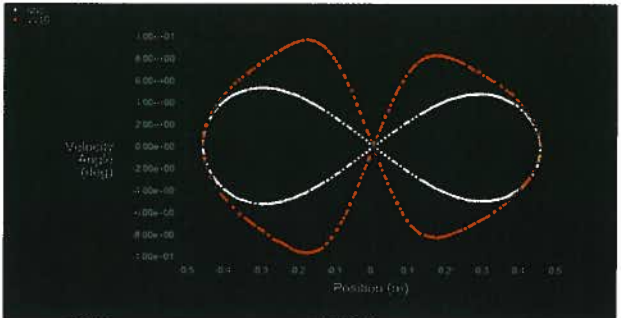


Figure 7-31: Comparison of velocity angle distribution over the blades' path for UBC and YV10 ducts

Duct YV11 has the same dimensions for the bumps as YV10. The YV10 was modified in order to shift the maximum velocity location towards the areas upstream and downstream of the turbine where the generated torque is positive. Shifting the maximum velocity location also reduces the counter-torque generated at the mid-section of the turbine. Figure 7-32 and Figure 7-33 show the comparison of the velocity magnitude and velocity angle distribution over the blades' path respectively.

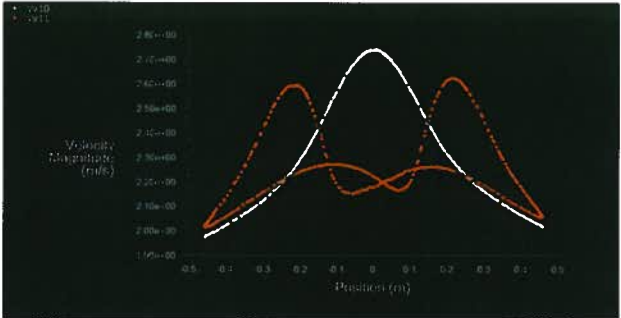


Figure 7-32: Comparison of velocity magnitude distribution over the blades' path for YV10 and YV11 ducts

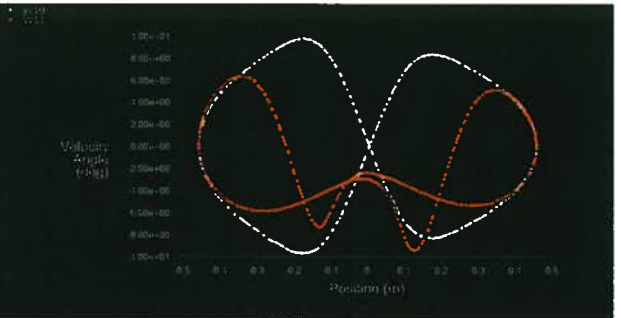


Figure 7-33: Comparison of velocity angle distribution over the blades' path for YV10 and YV11 ducts

As shown in Figure 7-32, the maximum velocity location was properly shifted, but due to the blockage effects at the duct entrance, the maximum velocity is lower compared to the configuration with bumps in the center. It is also observed that the velocity vector is deflected a few degrees at the center, hence,

allowing for a positive torque generation by a potential blade. However, since the velocity angle is lower than velocity angle in YV10, the angle of attack will not be changed properly for this duct. Therefore, it was decided to study the effect of bump shape on the velocity magnitude and angle over the blades' circular path. Duct YV12 was modeled to understand the effect of the bump length on the flow field while duct YV13 studied the effect of having four bumps instead of a diagonal pair. Ducts YV14, YV15, and YV16 were designed to investigate the effect of bump thickness and camber on the flow field inside the duct.

Figure 7-34 and Figure 7-35 show the effect of the bump length on the velocity field over the blades' path. It is seen that having a longer bump slightly increases the average velocity but dampens the velocity peaks in the upstream and downstream and increases the velocity magnitude at the center. Also, the velocity angle does not change significantly except at azimuth angles of about 60 and 120 degrees where the velocity angle and thus the angle of attack seen by the blades are reduced.

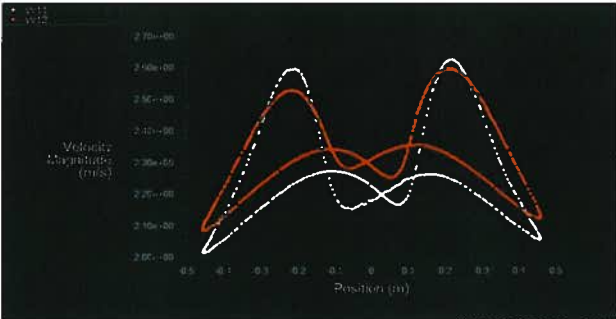


Figure 7-34: Comparison of velocity magnitude distribution over the blades' path for YV11 and YV12 ducts

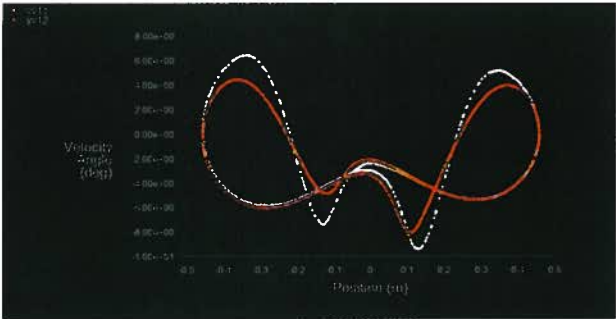


Figure 7-35: Comparison of velocity angle distribution over the blades' path for YV11 and YV12 ducts

Figure 7-36 and Figure 7-37 show the effect of using four bumps instead of two diagonally-configured bumps. The average velocity is lower and the velocity angle is not redirected properly. As shown in Figure 7-38, the velocity angle suddenly changes from negative to positive and vice versa in the vicinity of the bumps. That phenomenon is due to the Coanda effect - the tendency of the fluid to adhere to a convex surface rather than following a straight path in its original direction. Hence, it can be concluded that using four bumps with the current size and shape as in YV13, results in increased blockage and inappropriate redirection of the upstream flow. However, changing the location of the bumps and the distance from the ducts may improve the duct performance.

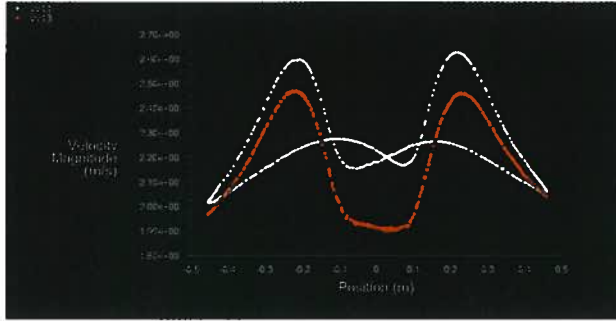


Figure 7-36: Comparison of velocity magnitude distribution over the blades' path for YV11 and YV13 ducts

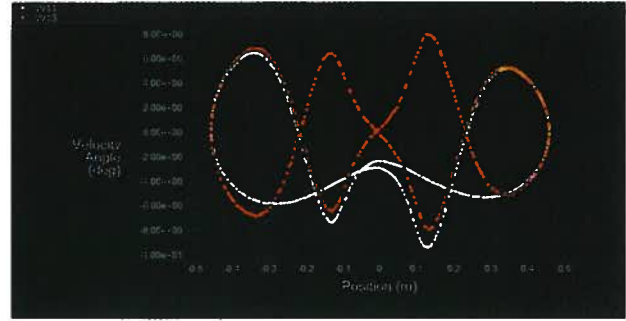


Figure 7-37: Comparison of velocity angle distribution over the blades' path for YV11 and YV13 ducts

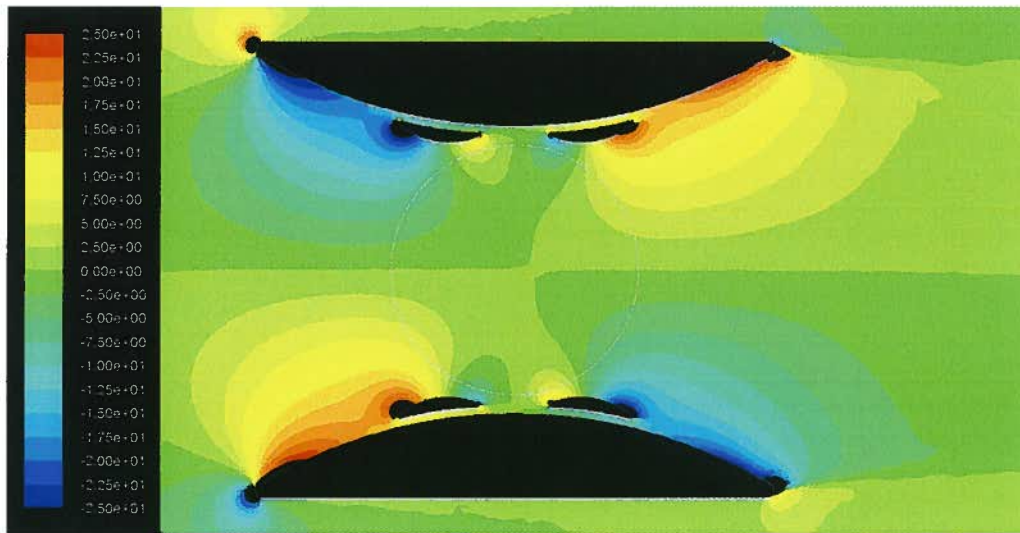


Figure 7-38: Velocity angles contours for the four-bump configuration (Duct YV13)

Ducts YV14, YV15, and YV16 were built to investigate the effect of the thickness and camber of the bumps on the velocity field over the blades' path. A comparison of velocity magnitude and angle for these ducts is presented in Figure 7-39 and Figure 7-40. The thickness of YV14 was set to be 0.10 inch while YV15 and YV16 have thicknesses of 0.13 and 0.14 inch. Also, in YV16, the camber location of the bump was moved towards the bump leading edge. The results show that the average velocity is decreased with an increased bump thickness as a result of increased blockage at the duct inlet. It is also seen that the flow reenergization property of the bump becomes less effective as the thickness is increased. Comparing the velocity magnitude and angle of ducts YV15 and YV16 also reveals that cambering the bump has a negative effect on duct performance. The fine-tuning process of the bump shape can be conducted using appropriate optimization tools.

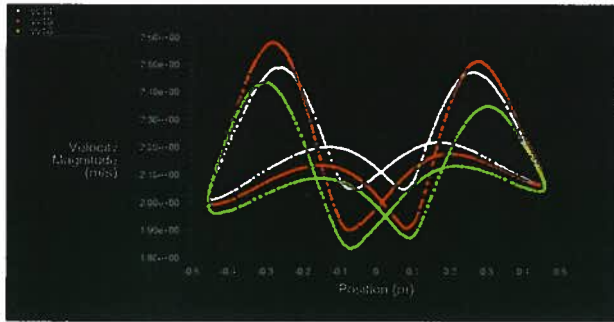


Figure 7-39: Comparison of velocity magnitude distribution over the blades' path for YV14, YV15, and YV16 ducts

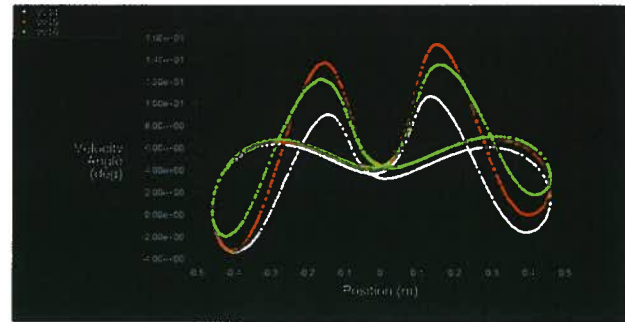


Figure 7-40: Comparison of velocity angle distribution over the blades' path for YV14, YV15, and YV16 ducts

In order to study the effect of the duct's length on the performance ducts YV17 and YV18 were simulated. Duct YV17 has a longer bump compared to YV15 but the bump thickness was kept constant. YV18 has the same proportions but is stretched in the X-axis direction. YV18 was set to be 50 percent longer than YV17. Although this study is beyond the box concept, it is still beneficial to understand the duct length effect on the turbine's performance.

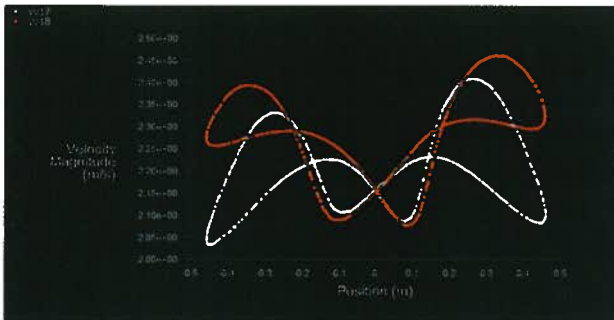


Figure 7-41: Comparison of velocity magnitude distribution over the blades' path for YV17 and YV18 ducts

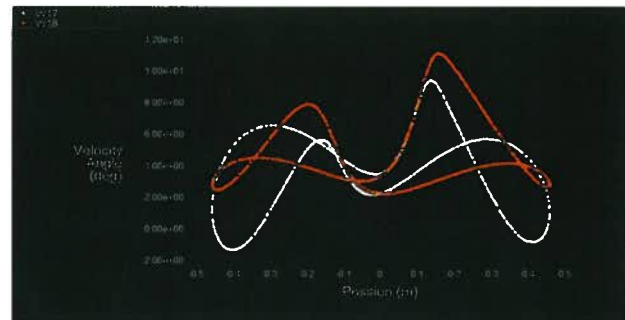


Figure 7-42: Comparison of velocity angle distribution over the blades' path for YV17 and YV18 ducts

It can be observed from the results and Figure 7-41 and Figure 7-42 that a longer duct yields an average velocity which is approximately 5% more than the basic duct length. Also, the flow deflection seems to be more effective when using a longer duct. In order to make a decision regarding the viability of the design, the increased generated power should be monitored against manufacturing, installation, mooring, and maintenance costs. However, this topic is beyond the scope of the current research.

A set of simulations were also conducted to study the effect of the bump placement relative to the main duct. Hence, YV19 which has an identical bump shape as YV14 was manufactured and simulated. The horizontal distance of the bump from the mouth in this configuration was 27 cm compared to 39 cm of

YV14. The simulation results showed that a slight increase in the average velocity can be achieved using this configuration. However, the effectiveness of the bumps seems to be reduced by placing the bumps further from the blades' path. The velocity magnitude and velocity angle distribution of YV19 is presented in Figure 7-43 and Figure 7-44 along with the results for duct YV20.

The last study in this category of ducts was to investigate the effect of the bump distance from the main duct. In other words, the width of the small channel between the bump and the duct was changed from 2.54 cm (1 inch) to 5.08 cm (2 inches) and the results were compared. The bump configuration for this study is identical to YV19 but with a larger gap of about 2 inches between bump and duct. The results show that increasing the gap width has a significant effect on the velocity magnitude and velocity angle over the blades' path. The velocity increases by more than 5 percent which can result in more than 17 percent increase in the available kinetic energy to the turbine. Also, the deflection angle reaches 17 degrees, a value larger than any other bump configuration studied. A comparison of velocity distribution for this duct and YV19 is presented in Figure 7-43 and Figure 7-44.

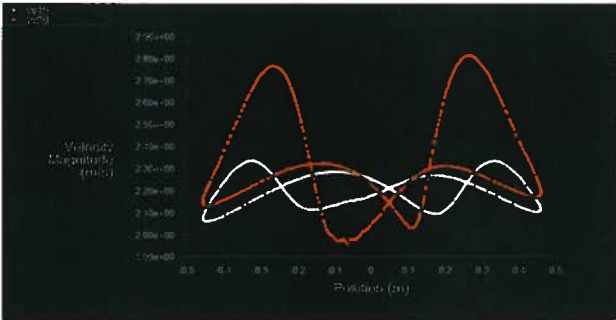


Figure 7-43: Comparison of velocity magnitude distribution over the blades' path for YV19 and YV20 ducts

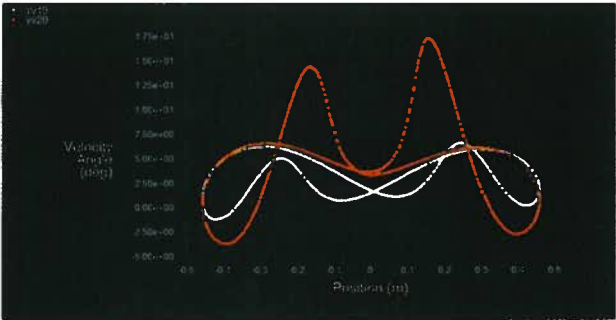


Figure 7-44: Comparison of velocity angle distribution over the blades' path for YV19 and YV20 ducts

Unsteady simulations were also conducted for YV11 and YV13 to investigate the effectiveness of bump mechanism in the presence of the turbine's blade. The results will be discussed later in this chapter along with other duct configuration simulated in unsteady conditions.

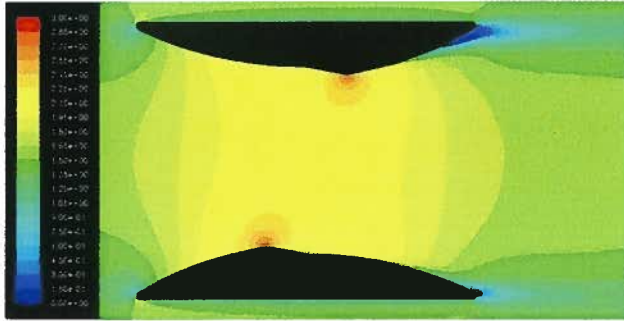


Figure 7-45: YV9 velocity contours

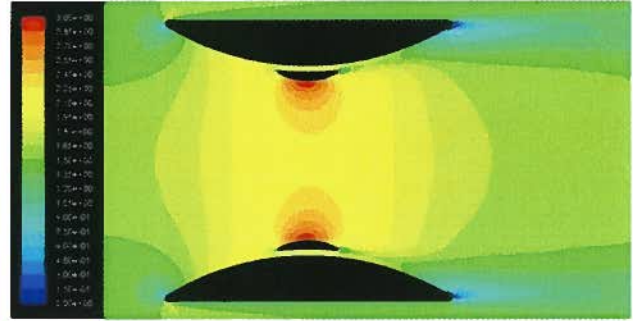


Figure 7-46: YV10 velocity contours

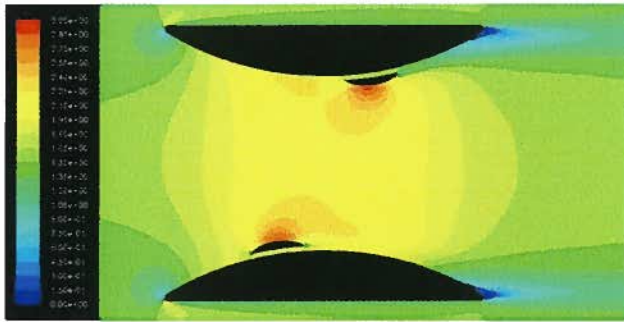


Figure 7-47: YV11 velocity contours

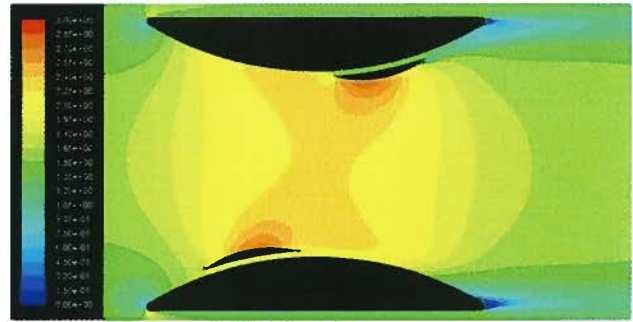


Figure 7-48: YV12 velocity contours

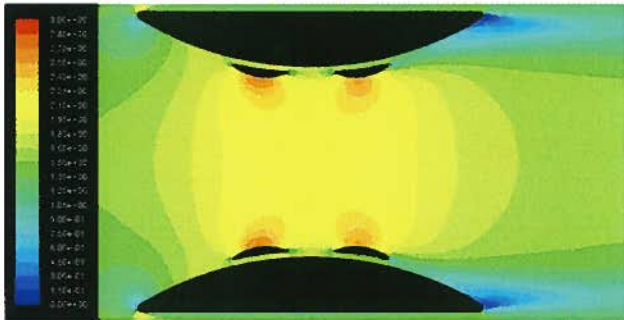


Figure 7-49: YV13 velocity contours

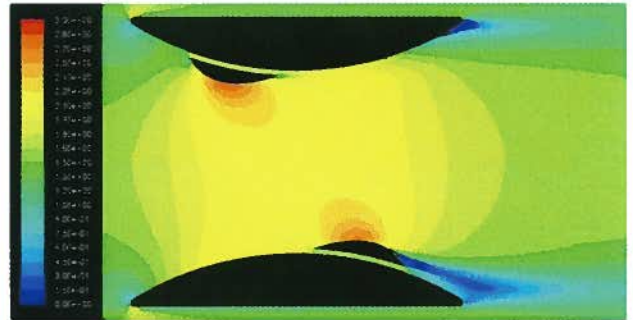


Figure 7-50: YV14 velocity contours

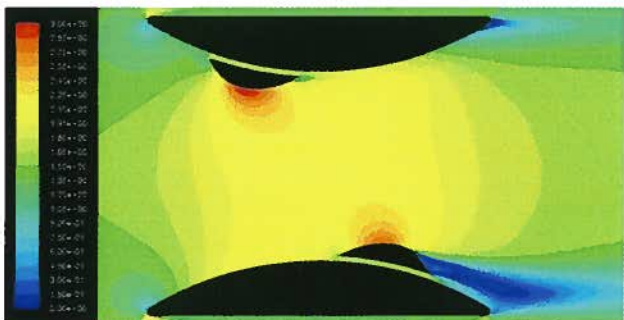


Figure 7-51: YV15 velocity contours

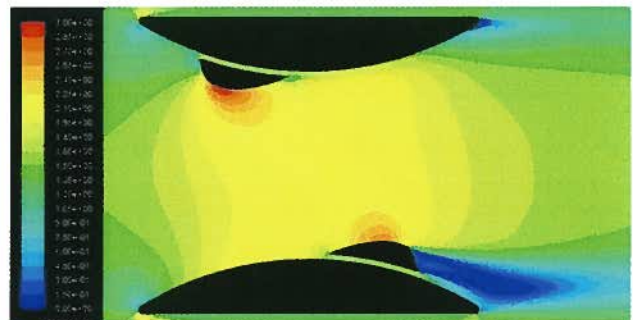


Figure 7-52: YV16 velocity contours

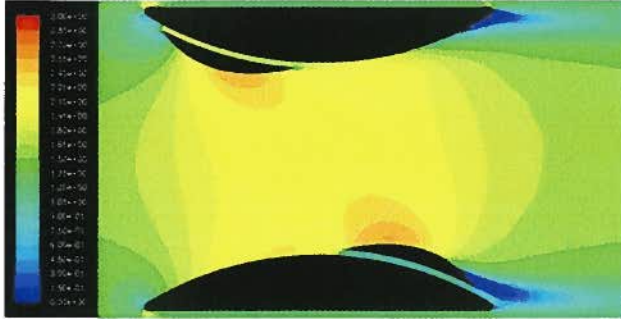


Figure 7-53: YV17 velocity contours

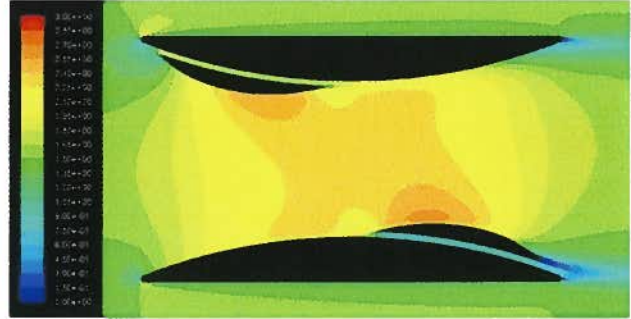


Figure 7-54: YV18 velocity contours



Figure 7-55: YV19 velocity contours

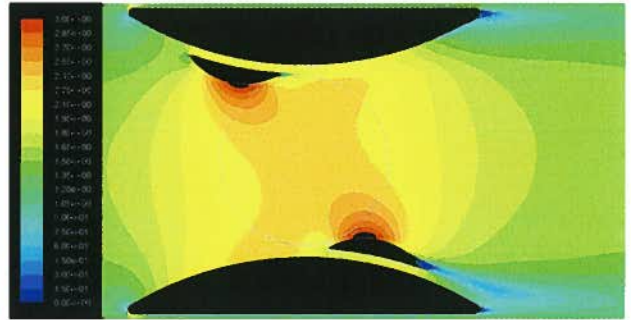


Figure 7-56: YV20 velocity contours

Category 4: Double-Duct Concept

Duct names: YV21, YV22, YV23, YV24, YV25, YV26, YV27, and YV28

Goal: To maximize the velocity magnitude inside the duct

Type: Multiple-compartment ducts

The double-duct concept is similar to the bump concept, but the objective of this approach is to increase the velocity magnitude inside the duct as much as possible. Needless to say that an increased velocity inside the duct has a direct effect on the resultant velocity vector and hence the angle of attack the blades see. A larger velocity magnitude results in an increased angle of attack. Figure 7-61 to Figure 7-68 show the velocity contours obtained from the simulations for this category of ducts. The results are presented in Table 7-4 and compared to the UBC duct.

Table 7-4: Double-Duct configuration results

Duct Name	Mass flow rate (kg/s)	Maximum Deflection Angle (Deg)	Average Velocity on blades' path (m/s)
UBC	2392	5.30	2.189
YV21	3061	4.25	2.873
YV22	3260	5.40	3.011
YV23	3168	5.34	2.938
YV24	3362	3.131	5.42
YV25	2907	5.36	2.709
YV26	2679	5.36	2.477
YV27	2785	6.83	2.547
YV28	2771	9.21	2.643

Ducts YV21, YV22, YV23, and YV24 were designed to study the double-duct concept. This concept aims to reduce the blockage of the duct by splitting it into two sections. In this design, the fluid can flow through a gap between two ducts, thus preventing the severe separation downstream of the duct. Hence, the shear layer effect would be minimal and the flow expansion can occur smoothly. There are some additional benefits from mechanical design point of view by using these type of ducts as well. These benefits include smaller duct sizes, reduced costs, and less mooring problems (due to the smaller drag force that these ducts produce). YV21 and YV22 basically compare the performance of a single and double duct concept. The inner duct in YV22 was the UBC duct and the outer duct was a scaled model of the same duct with a scaling factor of 2. YV22 is a single duct with the same contraction ratio as YV21 (approximately 30%). YV23 and YV24 were also modeled to capture the effect of the inner duct shape on the flow field inside the turbine area. The results show that using a double-duct concept can considerably improve the duct performance.

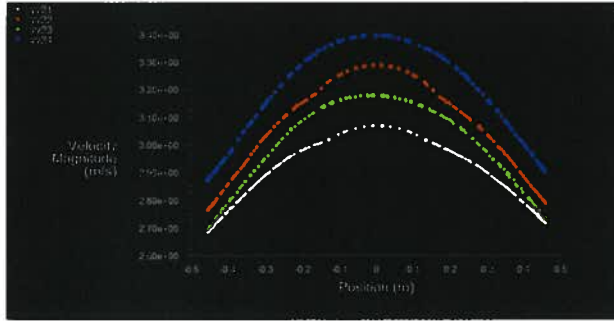


Figure 7-57: Comparison of velocity magnitude distribution over the blades' path for YV21, YV22, YV23, and YV24 ducts

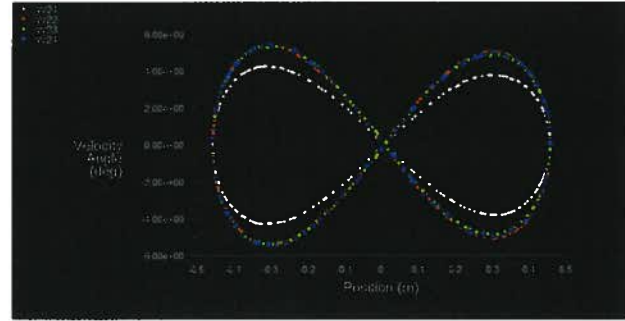


Figure 7-58: Comparison of velocity angle distribution over the blades' path for YV21, YV22, YV23, and YV24 ducts

As it is seen in Figure 7-57 and Figure 7-58, using the double duct concept with the same contraction ratio can increase the average velocity magnitude by approximately 10 percent. Also, the velocity angle distribution improves compared to the single duct case. However, the velocity deflection is in the same order as the UBC duct and other methods such as guide vanes or bumps can be used to manipulate the velocity angle and consequently the angle of attack the blades see.

As the duct size is very crucial from a mechanical design point of view and has a direct effect on manufacturing, installation, mooring, and cost, a study was conducted to investigate the effect of the outer duct size on the flow field. YV25 is a double-ducted configuration with a contraction ratio of 0.45 and the outer-duct length of 3.812 m. The length of the outer-duct for YV26 and YV27 was set to 2.303 m in order to capture the effect of the outer-duct length on the average velocity and velocity angle. YV26 and YV27 have identical outer-duct geometries. The inner-ducts of these two ducts have the same aspect ratio but with different curvatures. In addition to these ducts, YV28 was designed to understand how effective a bump configuration would be in a double-duct design. The comparison of the results of duct YV25 and YV26 reveal that using a shorter duct (approximately 40% shorter) can result in an average velocity drop of about 8 percent. Thus, using a longer duct with the same contraction ratio can improve the performance at the cost of increased manufacturing, installation, and maintenance cost. Duct YV27 results show that by cambering the inner duct, it is possible to increase the average velocity and the mass flow rate inside the duct. Also, duct YV28, which is identical to YV27 with an added bump has a larger velocity deflection and a higher average velocity but a lower mass flow rate due to the increased blockage caused by placing a bump close to the duct's mouth. Figure 7-59 and Figure 7-60 show the velocity magnitude and angle over the blades' path. The results show that the bumps are still effective in shifting the location of maximum velocity and reenergization of the flow downstream of the

turbine. The angle, however, seems to be similar to the regular UBC duct and bumps configuration, and no significant change is observed.

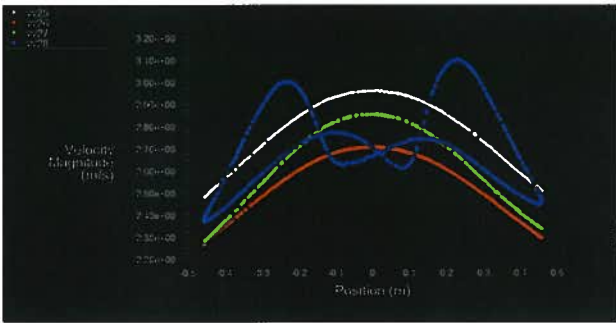


Figure 7-59: Comparison of velocity magnitude distribution over the blades' path for YV25, YV26, YV27, and YV28 ducts

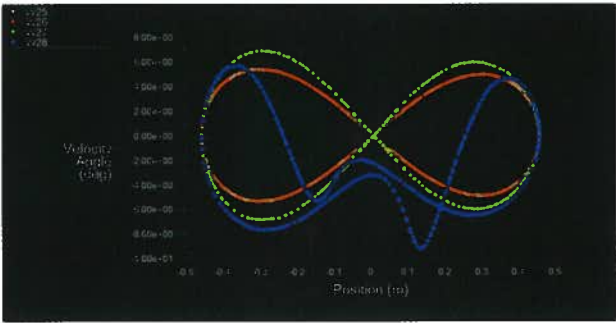


Figure 7-60: Comparison of velocity angle distribution over the blades' path for YV25, YV26, YV27, and YV28 ducts

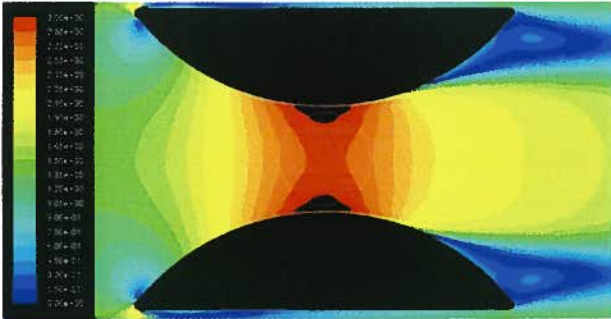


Figure 7-61: YV21 velocity contours

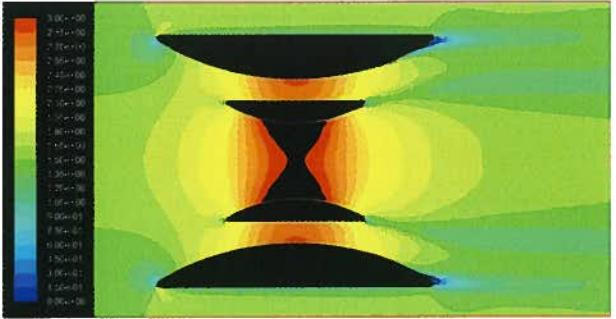


Figure 7-62: YV22 velocity contours

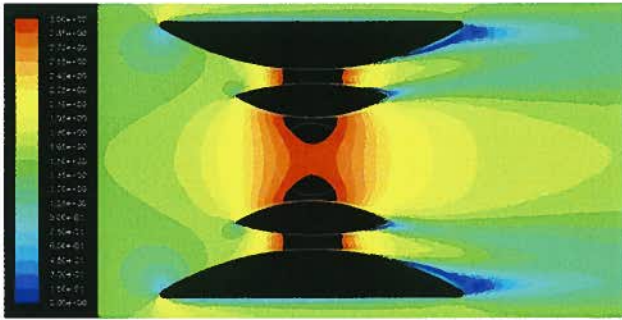


Figure 7-63: YV23 velocity contours

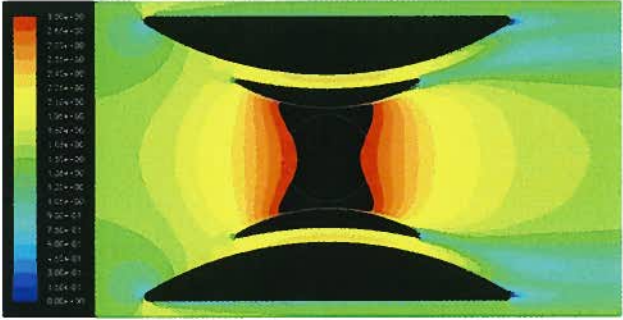


Figure 7-64: YV24 velocity contours

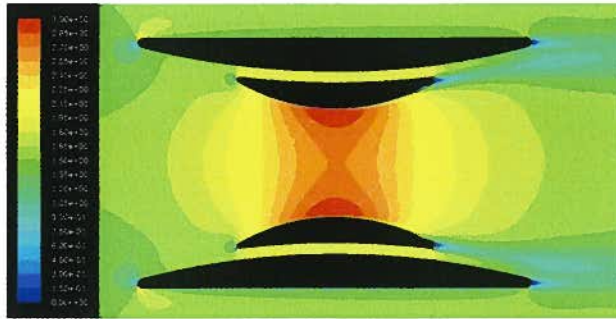


Figure 7-65: YV25 velocity contours

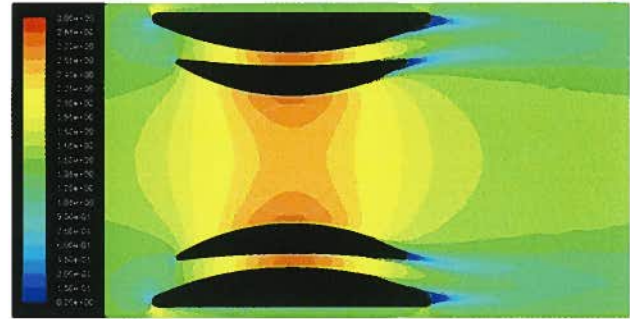


Figure 7-66: YV26 velocity contours

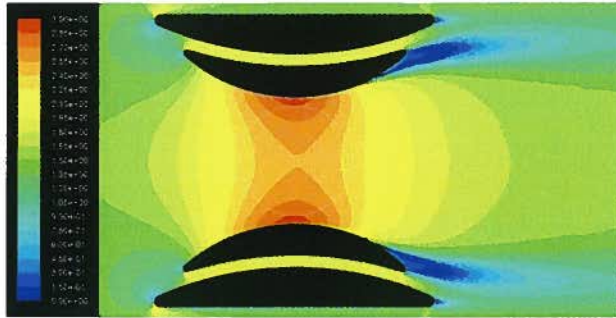


Figure 7-67: YV27 velocity contours

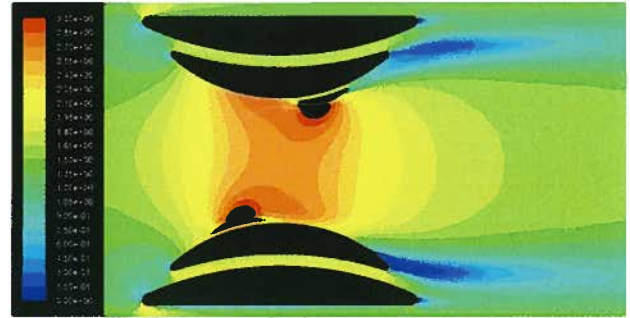


Figure 7-68: YV28 velocity contours

Category 5: Guiding-Vane Concept

Duct names: YV28, YV29, YV30, YV31, YV32, YV33, and YV34

Goal: To maximize the entrained mass flow rate inside the turbine especially at downstream

Type: Multiple-compartment ducts

The last set of simulations was dedicated to study a concept to entrain more fluid into the downstream region of the turbine in order to provide the downstream blades with a larger and more energized mass flow rate. Seven different configurations were simulated as shown in Figure 7-73 to Figure 7-84. Also, the summary of the results is presented in Table 7-5.

Table 7-5: Guiding vane concept results

Duct Name	Mass flow rate (kg/s)	Maximum Deflection Angle (Deg)	Average Velocity on blades' path (m/s)
YV29	1373	38.56	1.502
YV30	1489	5.23	1.414
YV31	2131	6.06	1.945
YV32	1795	6.02	1.516
YV33	1902	6.82	1.527
YV34	2121	9.67	1.722
YV35	2206	10.27	1.782

The first configuration simulated for this concept was YV29. The configuration consists of 16 guiding vanes, 8 in front and 8 in the back. The front side and the backside have four vanes at the top and four vanes at the bottom. NACA 4409 airfoil was used for the vanes' profile. The chord length of the vanes was 20 cm, 22.5 cm, 25 cm and 30 cm from front to the back. Also, the angle of attack of the vanes was set to 10, 15, 20, and 30 degrees. The trailing edges of the vanes are placed on a straight horizontal line. The vane angle of attack was increased in order to capture the flow separated from the upstream vanes and to guide it into the turbine area. The upstream and downstream vanes have different directions in order to conform to the symmetry assumption about the Y axis. This assumption explains that because the tidal flow changes direction by approximately 180 degrees, the duct should perform independent of the flow direction. The velocity contours of YV29 show that there is not a great amount of flow entrained into the downstream of the turbine because of the opposite direction of the downstream vanes. However, it is observed that the velocity downstream is increased as the entrained flow upstream cannot pass through the space between the downstream vanes. The mass flow rate and average velocity obtained using this configuration does not show any improvement compared to the UBC duct. The angle of attack, however, changes significantly, especially at the azimuth angles of about 90 degrees.

Duct YV30 uses a similar concept as YV29, but it is designed to examine whether any improvement can be achieved using flow injection to the downstream blades. The symmetry assumption was not considered in this design. The first, second, third and fourth vanes are identical to YV29, but the fifth and sixth vanes are identical to the fourth vane. The results showed that this configuration was not successful in achieving its goals. The velocity was reduced and the deflection was not as effective as YV29. The reason for poor performance of this duct can be the massive separation of the flow from the upstream vanes and the inability of downstream vanes to guide the separated flow inside the turbine area. Figure 7-69 and Figure 7-70 show the velocity magnitude and velocity angle distribution for YV29 and YV30. These figures show that YV30 has a minimal effect on the flow field and it does not affect either the velocity magnitude or velocity angle. On the other hand, although upstream velocity is low when YV29 is used, the downstream flow is properly re-energized as described before.

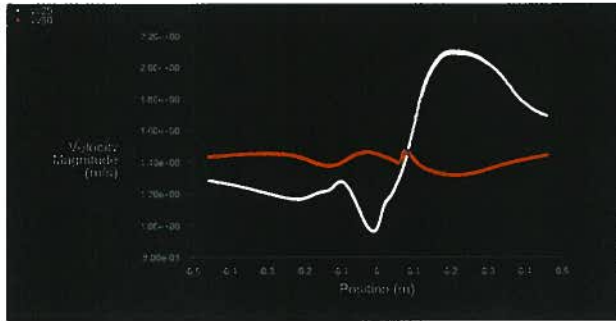


Figure 7-69: Comparison of velocity magnitude distribution over the blades' path for YV29 and YV30 ducts

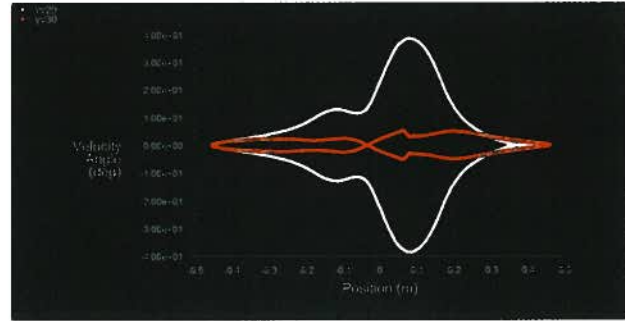


Figure 7-70: Comparison of velocity angle distribution over the blades' path for YV29 and YV30 ducts

YV31 is similar to the UBC duct with a channel going through the top surface of the duct all the way down to the inside area of the duct. This channel is basically used to increase the entrained mass flow inside the duct. However, the velocity vectors of this duct show that this mechanism does not perform properly as the flow is separated from the leading edge of the front part of the duct. YV32 is a modified, asymmetric version of YV31. The rear duct was designed to be more streamlined. However, this duct did not perform appropriately, especially due to the severe separation from the sharp leading edge of the front part of the duct. In order to address this problem, the front part was replaced with an airfoil shape (NACA 4409) in YV33 to reduce the separation from the leading edge. Also, the rear part of the duct was slightly moved in the positive y direction. This was done to transfer the stagnation point of the rear duct to a higher point in space, thus allowing a larger mass flow to be streamed into the channel between the front and rear parts of the duct. The results show that the performance is improved in this design compared to YV32. YV34 has an identical front part as YV33 but a longer, more streamlined rear part. The results showed that the mass flow rate was increased more than 13 percent in this case compared to YV33. This duct does not consider the symmetry assumption yet. YV35 is a symmetric model of YV34. Although it is observed that the velocity and mass flow rate could be kept high, the boundary layer separation from downstream vanes is severe and affects the shear layer and flow expansion downstream of the turbine. However, it seems that this separation cannot be avoided if the symmetry assumption is to be considered. The velocity magnitude and velocity angle distributions of YV31 to YV35 are compared in Figure 7-71 and Figure 7-72.

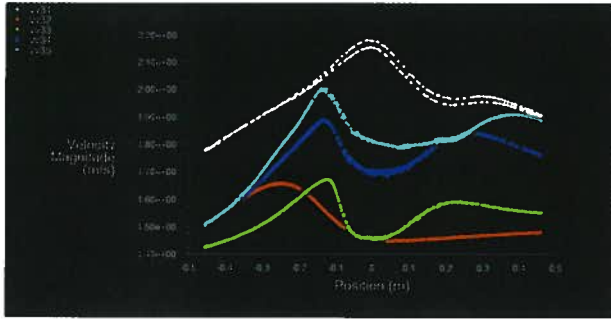


Figure 7-71: Comparison of velocity magnitude distribution over the blades' path for YV31, YV32, YV33, YV34, and YV35 ducts

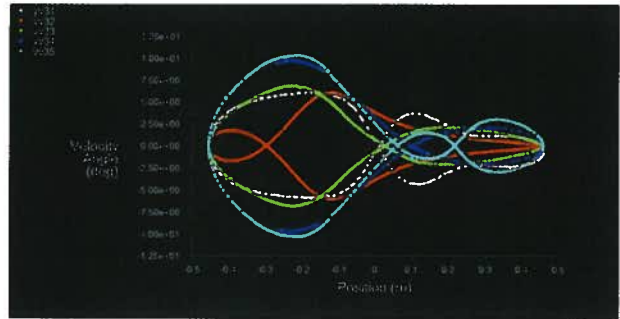


Figure 7-72: Comparison of velocity angle distribution over the blades' path for YV31, YV32, YV33, YV34, and YV35 ducts

The above figures show that YV32 and YV33 do not have an acceptable average velocity and velocity angle. YV31 has a high average velocity but the flow deflection is not significant. YV34 and YV35 have relatively larger velocities and velocity deflection angles. None of these ducts is effective in the redirection of the flow downstream. Therefore, it can be concluded that no superior performance is predicted to be produced by any of the ducts modeled in this category. However, in order to understand the duct-blade interactions, duct YV34 was simulated in unsteady conditions. This duct was chosen because of its relatively better performance (high average velocity and large velocity angles upstream) compared to the other ducts in this category. The results will be presented and discussed later in this chapter.

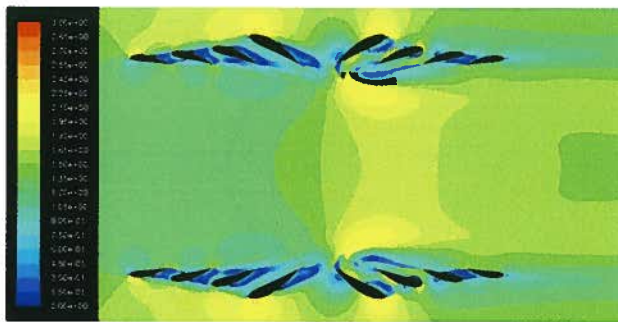


Figure 7-73: YV29 velocity contours

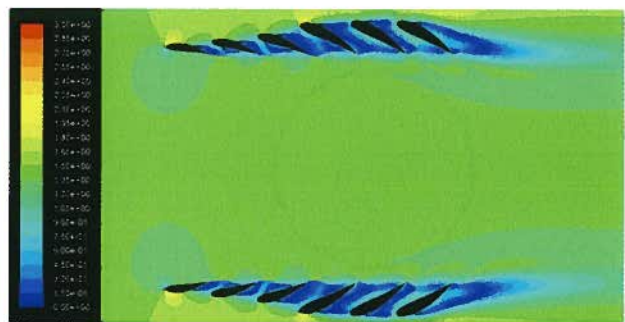


Figure 7-74: YV30 velocity contours

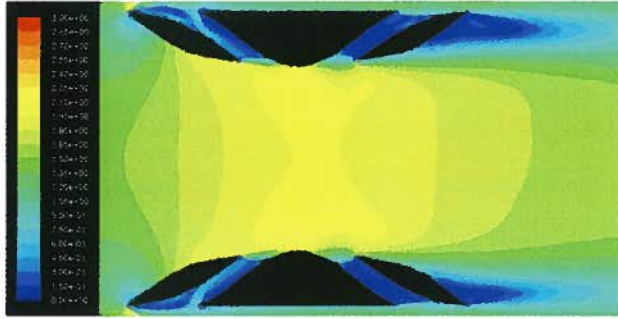


Figure 7-75: YV31 velocity contours

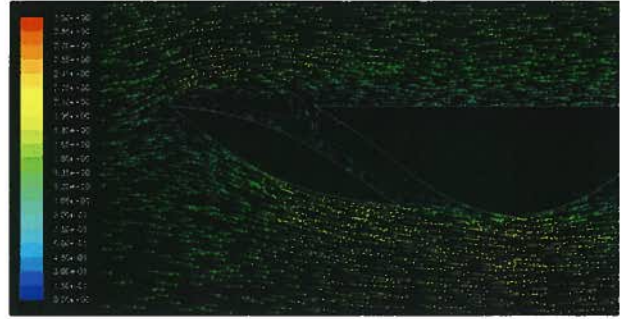


Figure 7-76: YV31 velocity vectors

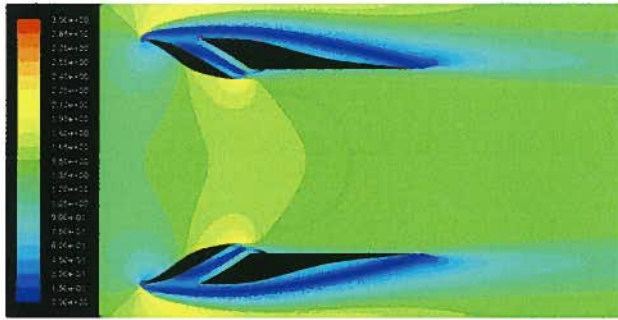


Figure 7-77: YV32 velocity contours

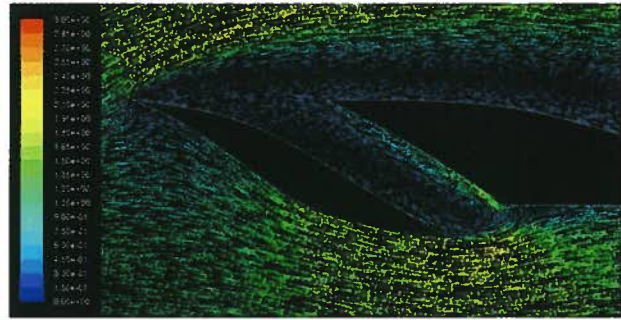


Figure 7-78: YV32 velocity vectors

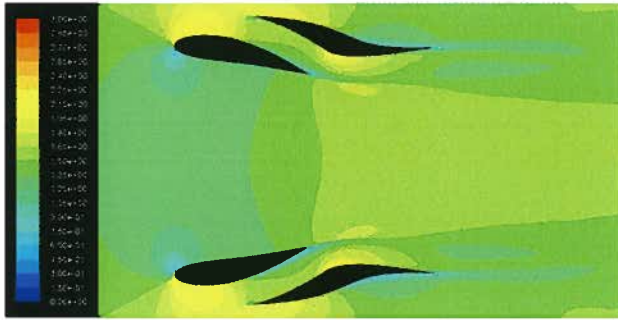


Figure 7-79: YV33 velocity contours

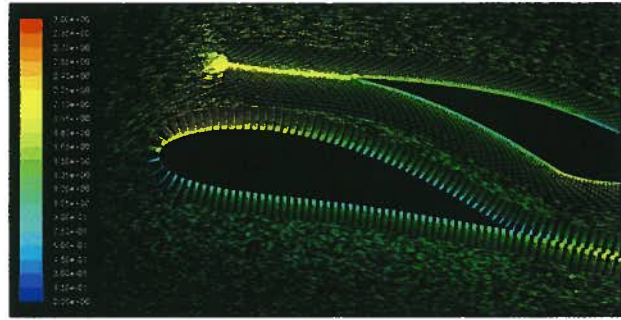


Figure 7-80: YV33 velocity vectors

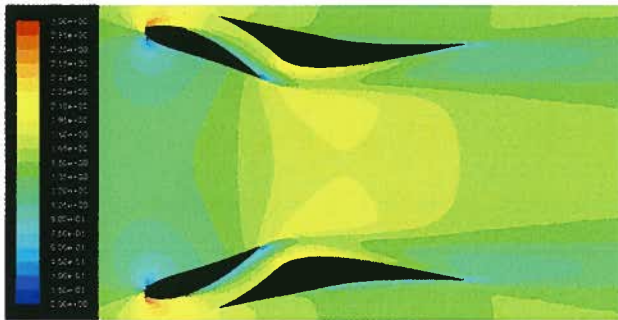


Figure 7-81: YV34 velocity contours

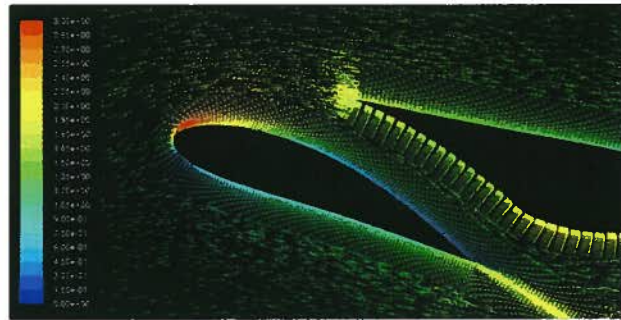


Figure 7-82: YV34 velocity vectors

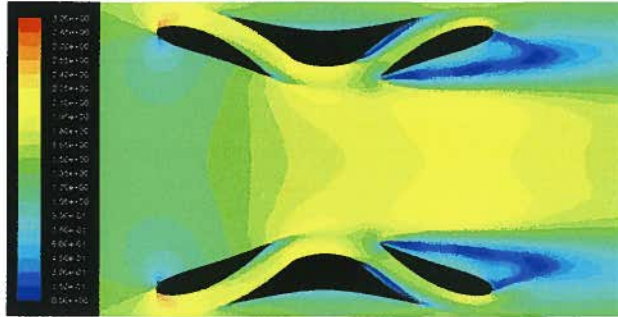


Figure 7-83: YV35 velocity contours



Figure 7-84: YV35 velocity vectors

7.3 Unsteady Simulations of Various Duct Configurations

Steady state simulations in the previous sections provided an idea of how each duct performs in reenergizing or redirecting the flow. The benefit of steady-state simulations was in saving computational time and cost. However, as steady-state models do not completely represent the flow field in the presence of the blades, it is necessary to run unsteady simulations to study the behaviour of the ducts and turbine's blades simultaneously. Ducts YV3, YV11, YV13, YV28, and YV34 were chosen to be simulated in unsteady conditions for this phase of the project. YV3 was chosen to capture the effect of the guide vanes while YV11 and YV13 were selected to show the effect of bumps. YV28 was simulated to show the effect of having bumps and double-duct concept together. Finally, YV34 was simulated to show the effectiveness of mass flow entrainment concept. The simulations were conducted for an inlet velocity of 1.5 m/s and TSR's of 2.00 to 4.00 with 0.25 increments. The comparison of the efficiency curve for the simulated ducts is presented in Figure 7-85. Finally, the torque curve for each duct is compared at each TSR to give a clearer understanding of the duct behaviour at different working conditions. The results show that there is no superior duct between the simulated cases. It seems that the flow entrainment concept (YV34) improves the performance slightly at lower TSR's while the efficiency is lower than the UBC duct for higher TSR's. The bump concept (YV11 and YV13) was observed to be ineffective as the increased blockage at the duct inlet reduces the mass flow rate inside the turbine in addition to reducing the average velocity magnitude and hence the kinetic energy inside the turbine area. It is also seen that the double-duct concept (YV28) increases the efficiency at TSR's over 2.75 and the maximum efficiency reaches approximately 68% at TSR of 3.00. The low efficiency of this design in lower TSR's can be explained as the increased local velocity causes a larger angle of attack and the blade stall at lower TSR's. At high TSR's where the blade does not stall, the increased kinetic energy entrained into the turbine area causes an increased generated power and efficiency. The results also show that the guiding vane concept (YV3) does not improve the efficiency. It is observed that the

rotation of blades downstream of the guiding vanes affect the flow over the vanes and causes flow separation which lowers the upstream blades' torque. However, the size and the distance of the vanes from the blades' path can be investigated in more details in future.

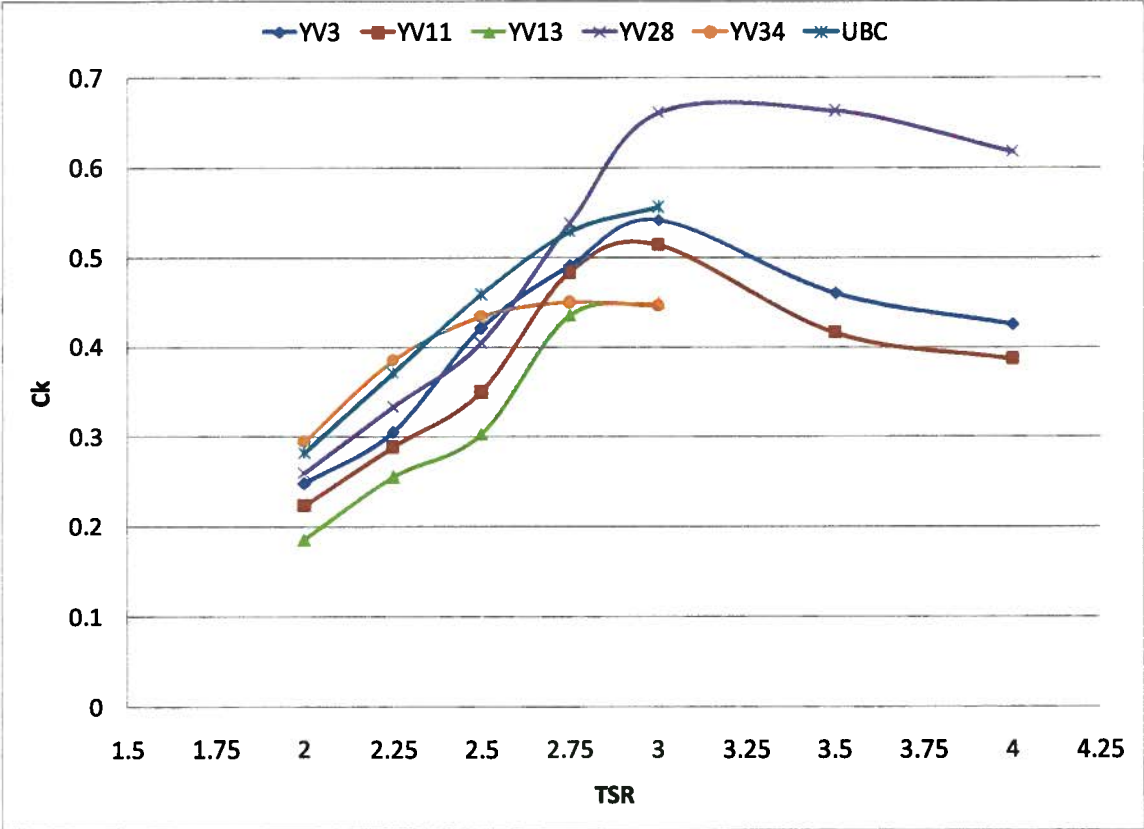


Figure 7-85: Efficiency comparison for different duct shapes

Figure 7-86 to Figure 7-95 show the torque curves over a cycle for the unsteady duct simulations. The single blade torque curves are also presented to assist in evaluating the effectiveness of each concept and to give guidelines for future improvements.

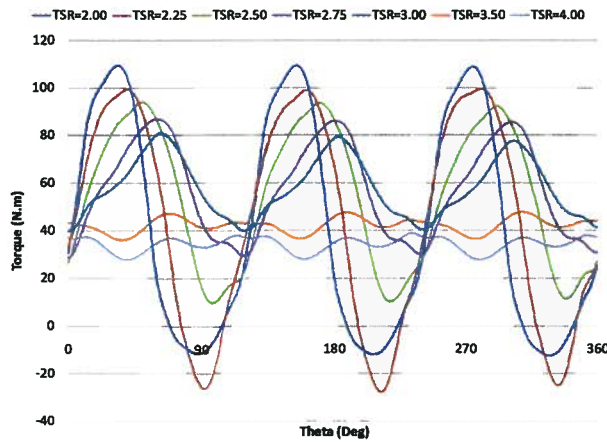


Figure 7-86: 3-Blade torque curve for YV3 at different TSR's

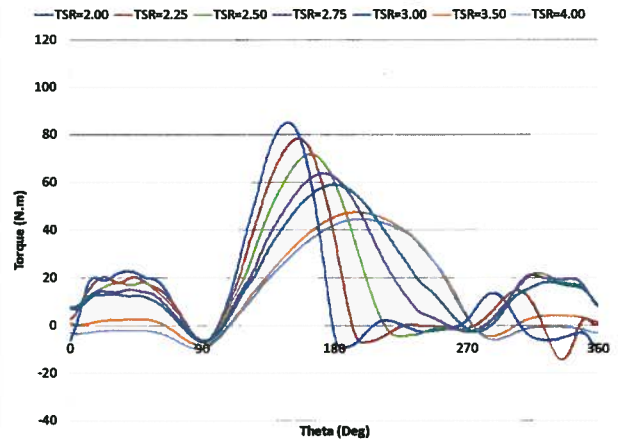


Figure 7-87: Single-blade torque curve for YV3 at different TSR's

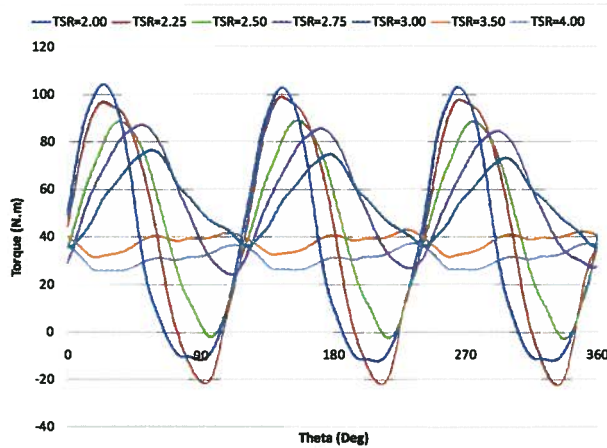


Figure 7-88: 3-Blade torque curve for YV11 at different TSR's

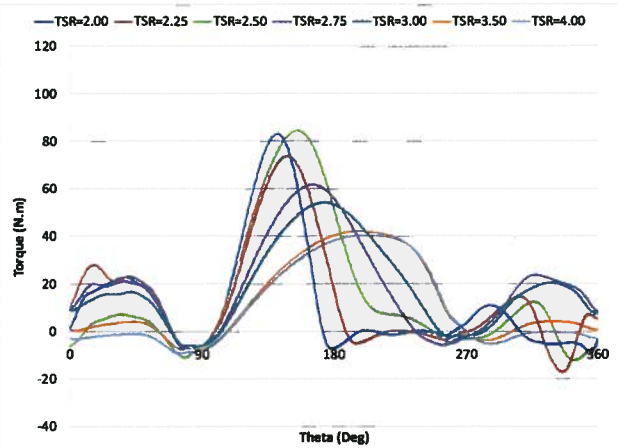


Figure 7-89: Single-blade torque curve for YV11 at different TSR's

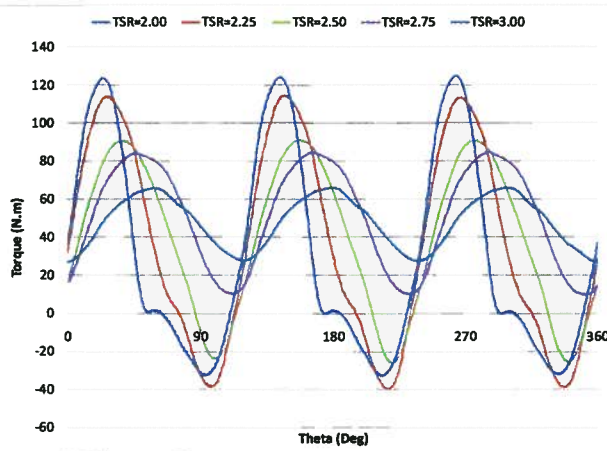


Figure 7-90: 3-Blade torque curve for YV13 at different TSR's

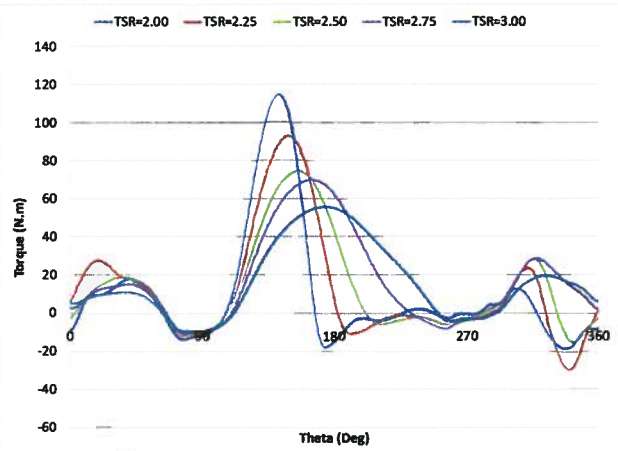


Figure 7-91: Single-blade torque curve for YV13 at different TSR's

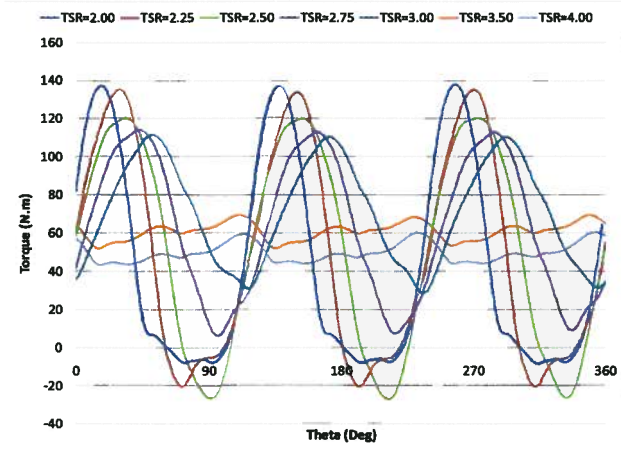


Figure 7-92: 3-Blade torque curve for YV28 at different TSR's

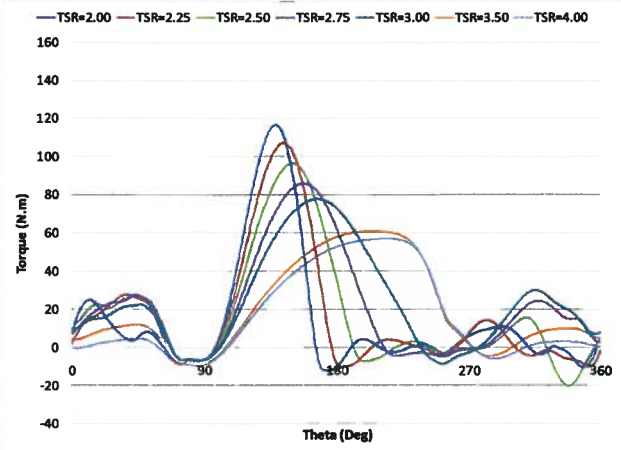


Figure 7-93: Single-blade torque curve for YV28 at different TSR's

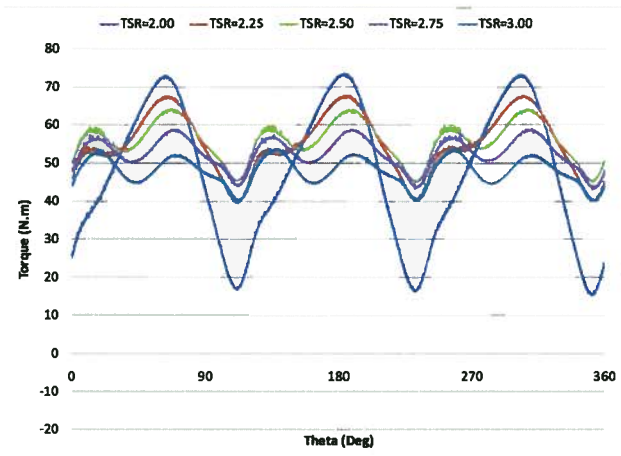


Figure 7-94: 3-Blade torque curve for YV34 at different TSR's

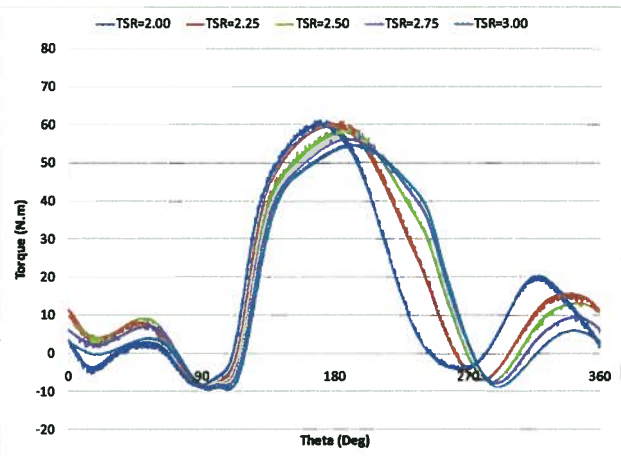


Figure 7-95: Single-blade torque curve for YV34 at different TSR's

The guide vane torque curves (YV3) show a trend similar to the UBC duct, and thus, the role of the guide vanes in flow redirection is not significant. It is observed that the torque amplitude decreases with an increased TSR as a result of a smaller range of angle of attack seen by the blade. The efficiency was also found to be very close to the UBC duct due to the insignificant effect of the vanes. The torque curve at very high TSR's (3.50 and 4.00) shows that the torque ripple is minimized due to the same reason. It is also seen that for all cases, the single-blade torque curve expands as TSR's increase.

Comparison of the torque curves obtained for YV11 and YV13 with the UBC duct shows that the torque amplitude is smaller. Also, the maximum torque value is lower in these cases as the result of the increased blockage due to the presence of the bumps at the inlet.

YV28 results show that the torque amplitude is increased as a result of increased velocity inside the turbine area. However, due to the high angle of attack at low TSR's and high velocity, the blades stall and the dynamic stall phenomenon causes the torque curve to be sharp with a large amplitude and negative torque. It is seen that the effect of dynamic stall decreases as the TSR increases. Hence, at high TSR's (such as 3.00 or more) where the average torque value drops for other cases, the average torque for this case is still high and the efficiency is the highest among the examined cases. However, there can be two major problems with this duct. The first problem is the difficult mooring of the duct as the size of this duct is larger than the UBC duct and other ducts with the same contraction ratio. The other problem with this duct is that its performance is satisfactory at high TSR's only.

The last simulated duct (YV34) proved that the flow injection can be effective at low TSR's (2.00 and 2.25). The other advantage of using this duct is the reduced torque ripple as a result of a uniform distribution of angle of attack over the cycle. A widened single-blade torque curve for this duct (Figure 7-95) supports the fact that the flow redirection concept works properly for this configuration. However, the low torque amplitude over the downstream blade rotation shows that the flow entrainment effect is not significant. This is due to a significantly smaller momentum of the injected secondary flow compared to the main stream flow. As shown in Figure 7-96 and Figure 7-97, the flow separates from the suction sides of the vanes at high TSR's. This is the direct effect of the changes occurring downstream of the vanes. The blades rotate with a higher angular velocity thus increasing the blockage in the downstream regions.

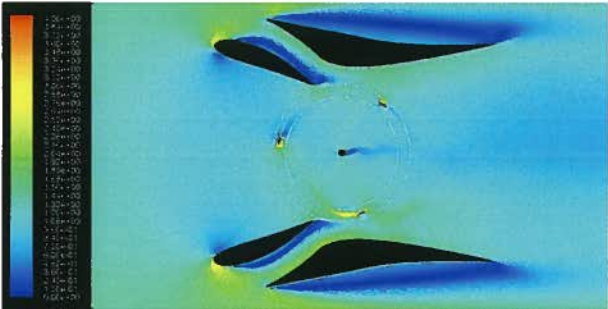


Figure 7-96: Velocity contours of YV34 show the flow separation from the upper side the guide vanes at V=1.5 m/s and TSR=3.00

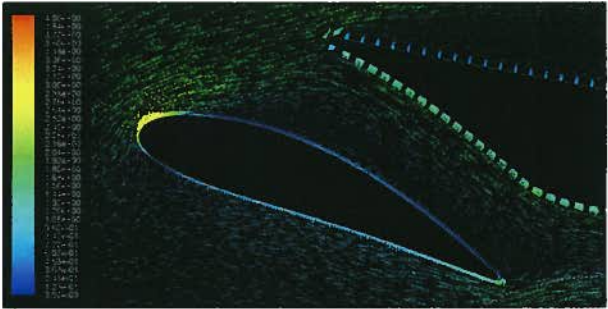


Figure 7-97: Velocity vectors of YV34 show the flow separation from the upper side of the guide vanes at V=1.5 m/s and TSR=3.00

YV34 can be useful in case the turbine needs to work at very low TSR's. Also, it can be structurally beneficial as the torque ripple is decreased. The type, size, angle, and position of the blades should be optimized in order to maximize the performance of the duct. The disadvantages of these ducts can be

summarized as difficult manufacturing and mooring and the high chance of blockage of the channel between the vanes and the main duct due to bio-fouling.

Figure 7-98 presents a summary of the duct study results conducted in this chapter. This bar chart consists of two series of bars for efficiency and the Torque Ripple Factor (TRF). This chart can facilitate the duct selection process as a desirable duct is the one with a high C_k and low TRF.

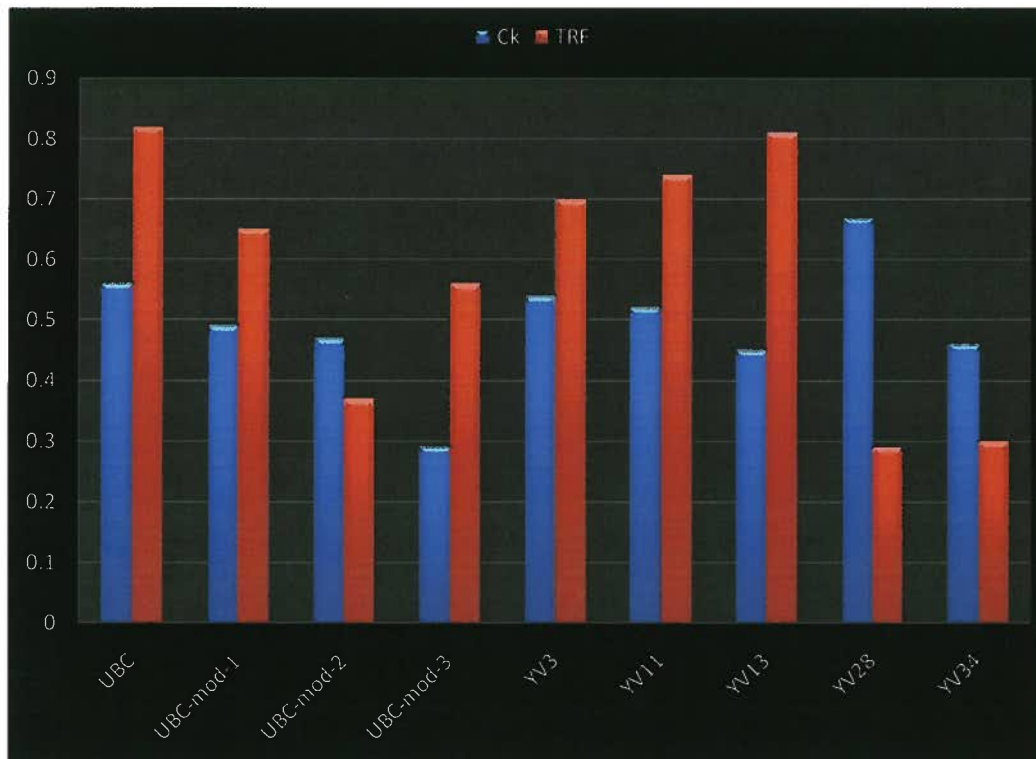


Figure 7-98: Summary of the performance of studied ducts

8. Conclusion, Recommendations, and Future Work

8.1 Conclusion

The current research focused on the numerical simulation of a ducted vertical axis tidal turbine using the commercial CFD package, FLUENT. The geometric parameters of the rotor such as the radius of the turbine, the blades' profile, and solidity ratio were assumed to be constant. Previous studies at the NRC suggested that if the turbine were confined within a duct, the generated power could increase significantly. The concentration of this research was to find a duct shape that could improve the performance of the turbine.

The first stage of the research was dedicated to the validation of the numerical model. A free-stream turbine as well as a parabolic duct shape with an identical duct tested experimentally at University of British Columbia, were simulated at different tip speed ratios, and the results were compared with experimental results. There were several discrepancies between the two-dimensional numerical models and the three-dimensional experimental model. A comparison of the results, however, shows that the numerical models have an acceptable level of accuracy and are capable of capturing important trends affecting turbine performance, and can thus be used as a reliable tool for optimization purposes.

After gaining sufficient confidence in the accuracy and validity of the numerical models, the second stage of the project was dedicated to the investigation of the duct shape effect on the performance of the turbine. Different concepts such as flow redirection, flow entrainment, and the double-duct concept were examined to improve the performance of the turbine relative to the case of the UBC duct. As the unsteady simulations are computationally expensive, each duct shape was simulated in the steady-state conditions, and only when performance was promising, the unsteady simulations were conducted for the duct shape. All the examined duct shapes were assumed to have the same contraction ratio as the UBC duct in order to standardize the performance comparison, except for the case of the double-duct concept.

The unsteady simulation results show that no superior solution was found for the ducting problem. A few duct shapes had a higher efficiency at low TSR's while a number of other ducts performed better at high TSR's. It was also observed that although certain ducts reduce the efficiency relative to the UBC duct, they can be useful in addressing the torque ripple problem. The summary of the results will be presented in the Recommendations section.

8.2 Recommendations

The approach taken in studying the turbine in the current research can be used as a guideline for future researches. This research showed that although RANS simulations are more accurate than potential flow codes, they are efficient tools for certain applications only. It was found that RANS simulations are not very efficient for optimization of the rotor. The RANS simulation of a free-stream turbine can take up to four days and up to a week for a ducted turbine. Although the simulations' run-time is very long, the set-up time is significantly shorter than that of potential flow codes. Thus, RANS simulations using the commercial packages are recommended when a quick solution is required and when there are time constraints in developing potential flow codes.

It is also recommended that RANS simulations be used for applications with significant flow separation. Although RANS simulations suffer from lack of accurate turbulence models, they allow for the inclusion of separation which is not possible in potential flow codes. The potential flow codes can therefore be used for the free-stream turbine as well as in the UBC duct case; however, they cannot be used in the guide vane applications, bumps applications, and probably in double-duct applications. In addition, potential flow codes could not be used for the majority of the ducts studied in Chapter 7 because many of these ducts showed significant flow separation inside the turbine operational area. Also, the shaft effect cannot be captured in the potential flow codes while it can be properly modeled in the RANS simulations.

Also, most of the potential flow codes are incapable of properly modelling the dynamic stall phenomenon. They also require experimental data of the blade profile. In such cases, CFD simulations would be an alternative to the experiments.

RANS simulations using a commercial package such as Fluent give a detailed insight to the physics of the problem by allowing the user to examine various parameters such as vorticity levels or velocity vector magnitude and direction. This significantly facilitates the analysis process and can help with the development of new concepts.

In addition to the general recommendations mentioned above, the engineering recommendations obtained from the current research for the duct shape are summarized in Table 8-1. The advantages and disadvantages of each duct are also presented to give engineering guidelines for future designs.

Table 8-1: Summary of the simulation results for different duct shapes

Duct Name	Advantages	Disadvantages
UBC	Simple and easy to manufacture, efficiency up to 56%, low torque ripple at high TSR's (TRF=0.82)	Medium-high efficiency, large torque ripple at low TSR's, high-level noise
UBC mod 1	High efficiency at low TSR's*, lower torque ripple at all TSR's (TRF=0.65), efficiency up to 49% at TSR=2.50, low-level noise, flat efficiency curve	7% lower efficiency, torque ripple significant for low TSR's, harder to manufacture
UBC mod 2	High efficiency at low TSR's, lower torque ripple (TRF=0.37), efficiency up to 47% at TSR=2.50, low-level noise, flatter efficiency curve, not very sensitive to TSR changes	9% lower efficiency, torque ripple relatively large at the lowest TSR, harder to manufacture
UBC mod 3	Significantly lower torque ripple (TRF=0.56), efficiency up to 29% at TSR=2.50, low-level noise, very flat efficiency curve, not very sensitive to TSR changes	27% lower efficiency (significant loss), harder to manufacture
YV3	Lower efficiency at all TSR's, efficiency up to 54%, low torque ripple at high TSR's (TRF=0.7)	2% lower efficiency, guide vane concept not effective, harder to manufacture, high-level noise
YV11	Lower efficiency at all TSR's, efficiency up to 52%, bump concept causes a slightly smaller torque ripple (TRF=0.74)	4% lower efficiency, bump concept not effective in increasing the efficiency, harder to manufacture, chance of blockage of the channel between bump and duct, high-level noise
YV13	Lower efficiency at all TSR's, efficiency up to 45%, torque in the same order of magnitude as the UBC duct (TRF=0.81)	11% lower efficiency, four-bump concept not effective in increasing efficiency, larger torque ripple, harder to manufacture, high-level noise
YV28	Higher efficiency at high TSR's, efficiency up to 67% at TSR=3.50, small torque ripple at very high TSR's (TRF=0.29)	Large size duct, hard to manufacture and moor, lower efficiency and larger torque ripple at low TSR's, high level noise
YV34	Higher efficiency at low TSR's, efficiency up to 46%, significantly lower torque ripple (TRF=0.30)	10% lower efficiency, very difficult to manufacture, chance of blockage of the channel between vane and duct, non-symmetric

* All comparisons are made to the UBC duct

8.3 Future Work

The current research should be pursued in two different paths. The first path is to improve and fine-tune the promising concepts that emerged from the analysis of various geometries. For example, the guiding vane concept was introduced and examined for one particular vane geometry and the results obtained from the simulations showed no significant improvement. However, the size, the incident angle, the profile, and the location of the vanes are parameters that if modified, may result in significant improvements in the performance of the turbine. In order to optimize any duct geometry, it is necessary to use optimization packages for CFD applications such as Sculptor, developed by Optimal Solutions, which uses an ASD (Arbitrary Shape Deformation) algorithm to achieve this purpose.

The second path that is vital for future development of the device is to address other engineering aspects of the project. Cavitation is among the factors that must be investigated. The factors affecting cavitation are the current velocity as well as the angle of attack, separation, and TSR. Although it was partially addressed in the current work, the torque ripple problem requires further study. A helical blade shape should be considered as an option and weighed against potential drawbacks such as ease of manufacturing when compared to the straight blade. The mechanical design side of the project is also very important and Finite Element Analysis is necessary, especially for large scale models. Fatigue problem is one of the issues that need to be addressed to ensure the reliability of the design. Also, the sensitivity of the design to different ocean conditions and the chance of blockage of the small channels in the ducts, such as the gap between the bumps and the main duct, are among the considerations for ocean applications. Mooring is another engineering aspect of the project which was beyond the scope of the current research but is among the most important challenges of this type of project.

References

- [1] Wikipedia, Online Encyclopaedia; "Carbon Emission";
http://en.wikipedia.org/wiki/Carbon_emission
- [2] BP; "Historical Data from 1965 to 2007";
<http://www.bp.com/sectiongenericarticle.do?categoryId=9017904&contentId=7033466>; 2007
- [3] Hubbert, MK; "The Energy Resources of the Earth, Energy and Power, A Scientific American Book"; pp.39; W.H. Freeman and Company; San Francisco, CA 1971 (ASIN: B00071D6RG)
- [4] Roosevelt IV, Theodore; Llewellyn, John; "Investors Hunger for Clean Energy,"
Harvard Business Review, Vol. 85, No. 10, pp. 38-40, Oct. 2007
- [5] Energy Information Administration;
http://www.eia.doe.gov/cneaf/solar.renewables/page/rea_data/rea_sum.html
- [6] Gunther, Marc; "For Solar Power, The Future Looks Bright", Fortune, Vol. 156, No. 8, pp. 45-50,
Oct. 2007
- [7] Google Finance, NASDAQ stock price of SunPower Corporation (SPWR) as November 2nd 2007
- [8] Draper, Mark; "More Than Just a Ripple: Ocean Power Technologies Sets Its Sights High",
Refocus, Vol. 7, No. 1, pp. 54-56, Jan.-Feb. 2006
- [9] Wikipedia, Online Encyclopaedia; "Rance Tidal Power Plant";
http://en.wikipedia.org/wiki/Rance_tidal_power_plant
- [10] Jeremy Thake, "Development, Installation and Testing of a Large-Scale Tidal Current Turbine",
UK Department of Trade and Industry, Contract No. T/06/00210/00/REP, Oct. 2005
- [11] Charlier, Robert H., "Tidal Energy", Van Nostrand Reinhold, 1982
- [12] Inventory of Canada's Marine Renewable Energy Resources, CHC (abstract)

- [13] Paraschivoiu, Ion, "Wind Turbine Design: with Emphasis on Darrieus Concept", Polytechnic International Press, Jun 2002
- [14] Mazharul Islam; Ting, David S.-K.; Fartaj, Amir; "Aerodynamic models for Darrieus-type straight-bladed vertical axis wind turbines", Renewable and Sustainable Energy Reviews, Available online 28 December 2006
- [15] Templin RJ.; "Aerodynamic Performance Theory for the NRC Vertical-Axis Wind Turbine", NRC Lab. Report LTR-LA-190, June, 1974. p. 29.
- [16] Wilson, RE; Lissaman, PBS; "Applied aerodynamics of wind power machines", Oregon State University, May, 1974
- [17] Strickland, JH.; "A Performance Prediction Model for the Darrieus Turbine" International Symposium on Wind Energy Systems", Cambridge, UK, September 1976, pp. C3-39–54
- [18] Muraca, RJ; Stephens, MV; Dagenhart, JR; "Theoretical Performance of Cross-Wind Axis Turbines With Results for a Catenary Vertical Axis Configuration", NASA TMX-72662, USA, 1975
- [19] Sharpe, DJ; "A Theoretical And Experimental Study of the Darrieus Vertical Axis Wind Turbine", School of Mechanical, Aeronautical and Production Engineering, Kingston Polytechnic, Research report, October, 1977
- [20] Read, S; Sharpe, DJ; "An Extended Multiple Streamtube Theory for Vertical Axis Wind Turbines", 2nd BWEA workshop, Cranfield, UK, April, 1980. p. 65–72
- [21] Lapin, EE; "Theoretical Performance of Vertical Axis Wind Turbines", ASME paper, 75-WA/Ener-1, The Winter Annual Meeting, Houston, TX, USA, 1975
- [22] Paraschivoiu, I; Delclaux, F; Fraunie, P; Beguier, C; "Aerodynamic Analysis of the Darrieus Rotor Including Secondary Effects" Journal of Energy 1983, Vol. 7 No. 5, pp. 416–421

- [23] Paraschivoiu, I; Delclaux, F; "Double Multiple Streamtube Model With Recent Improvements", *Journal of Energy* 1983; Vol. 7, pp. 250–255.
- [24] Larsen, HC; "Summary of a Vortex Theory for the Cyclogiro", *Proceedings of the second US National Conferences on Wind Engineering Research, Colorado state university, 1975*, pp. V8-1–3
- [25] Fanucci, JB; Walter, RE; "Innovative Wind Machines: The Theoretical Performance of A Vertical-Axis Wind Turbine", *Proceedings of the vertical-axis wind turbine technology workshop, Sandia Laboratories, SAND 76-5586, iii-61-95, USA, 1976*
- [26] Li, Ye; Nabavi, Yasser; Alidadi, Mahmoud; Klaptocz, Voytek R.; Rawlings, William G.; Calisal, Sander M.; "UBC Numerical Investigation of Vertical Axis Tidal Turbine: RANS CFD and Potential Flow", *Proceedings of the Seventeenth (2007) International Offshore and Polar Engineering Conference, 2007*, pp. 314-321, 2007
- [27] Strickland, JH; Webster, BT; Nguyen, T; "A Vortex Model of the Darrieus Turbine: An Analytical and Experimental Study" *Journal of Fluids Engineering* 1979
- [28] Hirsch, H; Mandal, AC; "A Cascade Theory for the Aerodynamic Performance of Darrieus Wind Turbines", *Wind Engineering*, 1987; Vol. 11 No. 3, pp. 164–75
- [29] Mandal, AC; Burton, JD; "The effects of dynamic stall and flow curvature on the aerodynamics of Darrieus turbines applying the Cascade model" *Wind Engineering*, 1994; Vol. 18, No. 6, pp. 267–82
- [30] Edinburgh Design Ltd., "Variable Pitch Foil Vertical Axis Tidal Turbine", UK Department of Trade and Industry, Contract No. T/06/00234/00/00, Mar. 2006
- [31] NEL-002: "Water Turbine Model Trials", March 1980, Barry v. Davis, Nova Energy Limited for NRC Hydraulics laboratory Ottawa

- [32] NEL-021: "Ultra Low Head Hydroelectric Power Generation Using Ducted Vertical Axis Water Turbines", March 1981, Barry V. Davis, David H. Swan, Kenneth A. Jeffers, Nova Energy Limited for NRC Hydraulics laboratory Ottawa
- [33] NEL-022: "Ultra Low Head Hydroelectric Power Generation Using Ducted Vertical Axis Water Turbines", October 1983, B. V. Davis, D. H. Swan, K. A. Jeffers, Nova Energy Limited for NRC Hydraulics laboratory Ottawa
- [34] NEL-038: "Research and Development of a 50kW to 100kW Vertical Axis Hydro Turbine for a Restricted Flow Installation", March 1984, B. V. Davis, J. R. Farrell, D. H. Swan, K. A. Jeffers, Nova Energy Limited for NRC Hydraulics laboratory Ottawa
- [35] NEL-070: "The Ducted Vertical Axis Hydro Turbine for Large Scale Tidal Energy Applications", March 1984, B.V. Davis, D.H. Swan, K.A. Jeffers, Nova Energy Limited for H. A. Simmons
- [36] NEL-081: "Commissioning and Testing of a 100kW Vertical Axis Hydraulic Turbine", December 1985, B.V. Davis, D.H. Swan, Nova Energy Limited for NRC Hydraulics laboratory Ottawa
Coefficients of a NACA0012 Airfoil at High Angles of Attack"; MECH579 term project, April 2006
- [37] Fluent Inc. "User's Guide," Fluent 6.2.2, Ch 12, 2006
- [38] Versteeg, H; Malalasekera, W; "An Introduction to Computational Fluid Dynamics: The Finite Volume Method", Prentice Hall, Feb 2007
- [39] Garret, Chris; Cummins, Patrick; "Generating Power from Tidal Current", Journal of Waterway, Port, Coastal, and Ocean Engineering, Vol. 130, No. 3, pp. 114-118, May/Jun 2004
- [[40]] Alidadi, Mahmoud; Nabavi, Yasser; "Experimental and numerical Study of a Vertical Axis Turbine", 8th Canadian Marine Hydrodynamics and Structures Conference, Oct 2007
- [41] Nabavi, Yasser; "Turbulence Modeling for a Vertical Axis Tidal Turbine", MECH579, Term Project